VNIVERSITAT DE VALÈNCIA

Departamento de Física Atómica, Molecular y Nuclear

Instituto de Física Corpuscular

Doctorado en Física

Development of high resolution and efficiency detectors based on Silicon Photomultipliers (SiPMs) and continuous crystals for medical physics applications

TESIS DOCTORAL PRESENTADA POR

John Barrio Toala

DIRIGIDA POR

Dra. Gabriela Llosá Llácer

Dr. Carlos Lacasta Llácer

Abril 2017

Declaration

Dra. Gabriela Llosá Llácer, *Investigadora Ramón y Cajal, CSIC*,
Dr. Carlos Lacasta Llácer, *Investigador Científico, CSIC.*

CERTIFICAN:

Que la presente memoria: **"Development of high resolution and efficiency detectors based on Silicon Photomultipliers (SiPMs) and continuous crystals for medical physics applications"** ha sido realizada bajo nuestra dirección en el Departamento de Física Atómica, Molecular y Nuclear de la Universidad de Valencia por Don John Barrio Toala y constituye su tesis para optar al grado de Doctor en Física.

Y para que así conste, firmamos el presente Certificado.

Firmado
Dra. Gabriela Llosá Llácer

Firmado
Dr. Carlos Lacasta Llácer

A mis padres,
por ser un ejemplo constante
y por apoyarme siempre.

Contents

Introduction

The work presented in this thesis is carried out within the instrumentation research line of the IRIS (*Image Reconstruction, Instrumentation and Simulations for medical imaging applications*) group of IFIC, which aims at the development of high performance detectors for PET and hadron therapy applications.

In these applications, spatial resolution is a critical parameter. Usually, the detection of gamma rays is performed employing detectors based on pixelated scintillator crystals coupled to segmented photodetectors. In such detectors, the spatial resolution strongly depends on the crystal size. In order to improve spatial resolution, small crystals are needed, which reduces the sensitivity of the detector. In addition, the reduction of the crystal size greatly increases the detector cost.

The work carried out in this thesis is motivated by the need to develop alternative detector designs capable of enhancing spatial resolution without reducing detector efficiency. Traditionally, photomultiplier tubes (PMTs) coupled to scintillator crystals have played a dominant role in the detection of gamma rays. In the last years, a new kind of solid state photodetector, the Silicon Photomultiplier (SiPM), has emerged as an option to substitute PMTs in certain applications. SiPMs have high gain and quantum efficiency, low bias voltage and excellent timing properties. Besides, they are very compact devices and insensitive to magnetic fields.

The use of continuous scintillator crystals coupled to SiPMs can lead to an improvement of spatial resolution and sensitivity at the same time, at the expense of imposing additional technological challenges. Besides, avoiding segmentation strongly reduces the detector cost, which can benefit the transfer of technology from research to commercial systems.

This thesis aims at overcoming such challenges and at evaluating the possibilities, limitations and further developments needed for the use of this innovative technology.

The main goal of this thesis is to demonstrate the feasibility of this approach in the development of novel detector concepts, focused on PET and hadron therapy applications, which have different requirements. To do so, scintillator crystals of different types coupled to SiPMs from several manufacturers have been tested and fully characterized. The work takes place at an early stage of development, and thus it is focused on evaluating the performance, rather than on achieving an optimal operation for each application.

The main part of the thesis comprises the development of a small animal PET prototype based on SiPMs and continuous LYSO crystals. In addition, the first tests of a Compton telescope based on SiPMs and continuous $LaBr_3$ crystals for treatment delivery monitoring in hadron therapy are presented.

The thesis is divided in six chapters. Chapters 1 and 2 describe the theoretical background for medical imaging and detectors for medical imaging, respectively, focused on the detectors and applications relevant for this work. Chapter 3 presents the results obtained with the first tests of a detector based on SiPMs and continuous $LaBr_3$ crystals for a Compton telescope. Chapter 4 describes the characterization, coincidence tests and simulations performed with a detector head based on SiPMs and continuous LYSO crystals for the development of a first prototype of a small animal PET.

In both Compton telescope and small animal PET applications, a new readout system was needed due to the foreseen increase in the number of readout channels. The ASIC selected was the VATA64HDR16 and chapter 5 shows the performance evaluation of this ASIC for medical physics applications based on continuous crystals and SiPMs. This ASIC is employed in chapter 6 to develop the second version of the small animal PET based on continuous LYSO crystals and SiPMs. Characterization tests and images with point-like sources and FDG are presented.

The thesis finishes with final conclusions and a summary of the work performed, written in Spanish.

Chapter 1

Medical imaging

Medical imaging is the technique and process that noninvasively produce visual representations of the interior of a body for clinical analysis and medical intervention, as well as visual representation of the function of some organs or tissues. In this sense, medical imaging can be seen as the solution of the mathematical inverse problem: the cause (the properties of the living tissues) is inferred from the effect (the observed signal). The main medical imaging modalities include X-ray imaging, computed tomography (CT), magnetic resonance imaging (MRI), ultrasound imaging and nuclear medicine.

Nuclear medicine is the branch of medicine that makes use of radioactive tracers (radiotracers) in the diagnosis and treatment of disease. Radiotracers consist of carrier molecules in which one or more atoms have been replaced by a radioisotope. A radioisotope is an atom whose nucleus has an excess of either protons or neutrons, making it unstable and prone to change to a more stable configuration by means of radioactive decay. The carrier molecules in a radiotracer vary greatly depending on the purpose of the scan and the biological phenomenon being investigated. Once administered to the patient, the radiotracer concentrates at specific organs or cellular receptors with a certain biological function. For this reason, nuclear medicine provides information about physiological processes, in contrast to other imaging techniques such as CT or MRI, which provide anatomical information.

In nuclear medicine imaging, two major types of radiotracers are employed: single photon emitters and positron emitters. The former emit one principal gamma ray or a sequence of gamma rays that are directionally uncorrelated. Positron emitters emit a positron that travels a short distance and annihilates with an electron. This annihilation

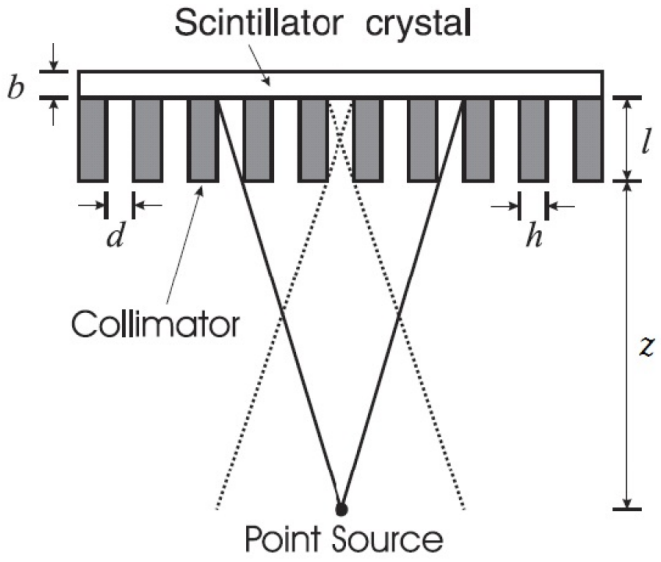

Figure 1.1: Gamma camera cross section. The incidence angle of the incoming photons is restricted by a mechanical collimator.

generates two 511 keV gamma rays, which travel in nearly opposite directions.

This thesis is focused on two nuclear medicine imaging techniques: Compton imaging, a variety of single photon emission computed tomography (SPECT), and positron emission tomography (PET). In the following sections, a brief overview of these imaging techniques is presented.

1.1 SPECT

SPECT is a nuclear medicine imaging technique that employs singles photon radioisotope emitters. The most common used radionuclide for SPECT is technetium-99m (^{99m}Tc), which emits gamma rays of 140.5 keV. The most widespread applications for SPECT have been myocardial pefusion imaging and functional brain imaging.

The single photons emitted by the radiotracer are detected by a gamma camera head consisting of a photodetector, a scintillator crystal and a collimator. The collimator rejects gamma rays that are not within a small angular range (see figure 1.1). The gamma camera head rotates around the patient acquiring planar projection images (2D) of the radiotracer distribution. 3D images are obtained by the combination of these planar images using tomographic reconstruction algorithms.

The spatial resolution in SPECT is dominated by the collimator. The resolution of the collimator is given by

$$Resolution = 2\frac{d}{l}\left(z+\frac{l}{2}\right), \tag{1.1}$$

where *d* and *l* are the diameter and the length of the collimator holes, respectively, and *z* is the distance from the collimator surface to the patient. It can be seen that the resolution can be increased reducing the factor *d/l*, but this results in a reduction of the efficiency, given by

$$Efficiency = \left(\frac{d}{2l}\right)^2. \tag{1.2}$$

Thus, the main limitation of SPECT comes from the employment of mechanical collimators and the fact that spatial resolution and efficiency in them are inversely related: an increase in one implies a decrease in the other.

1.2 Compton imaging

Compton imaging is a variety of SPECT in which mechanical collimators are replaced by a stack of detection planes working in time coincidence (electronic collimation). The gamma rays interact in the first detector by Compton scattering and the scattered photons interact in a second detector by photoabsorption. The employment of electronic collimation allows to eliminate the resolution-efficiency tradeoff imposed by mechanical collimators, making it possible to improve both simultaneously under the appropriate conditions.

1.2.1 Compton scattering

The interaction process of Compton scattering [1] takes place between an incident gamma ray photon (γ) and an electron in the absorbing material (*e*). The electron is assumed to be at rest (free), since its kinetic and binding energies are usually much lower than the energy transferred by the gamma ray. As a result of the interaction, the electron recoils (*e'*) and the scattered gamma ray (γ') propagates at an angle θ with respect to the original incidence direction. Figure 1.2 shows a representation of the interaction.

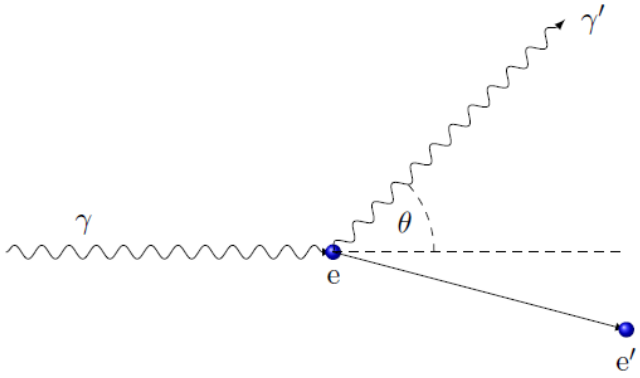

Figure 1.2: Compton scattering of a photon (γ) with a free electron (*e*). The electron recoils (*e'*) and the scattered gamma ray (γ') propagates at an angle θ with respect to the original incidence direction.

The expression that relates the energy of the scattered photon with the energy of the incident photon and the scattering angle can be obtained from the conservation of energy and momentum

$$E' = E_0 - E_e = \frac{E_0}{1+\alpha(1-cos\theta)}, \tag{1.3}$$

where *E'* is the energy of the scattered photon, E_0 is the initial energy of the photon, E_e is the energy of the recoil electron in the scatter detector and $\alpha = E_0/m_0c^2$, being m_0c^2 = 511 keV the electron rest-mass energy.

The cross section for Compton scattering is given by the *Klein-Nishina* formula

$$\frac{d\sigma}{d\Omega} = \frac{r_e^2}{2}\frac{1}{[1+\alpha(1-cos\theta)]^2}\left(1+cos^2\theta+\frac{\alpha^2(1-cos\theta)^2}{1+\alpha(1-cos\theta)}\right), \tag{1.4}$$

where r_e is the classical electron radius (r_e=2.81794 fm).

The integration of this formula over $d\Omega$ gives the total probability per electron for a Compton scattering to occur

$$\sigma_c = 2\pi r_e^2\left\{\frac{1+\alpha}{\alpha^2}\left[\frac{2(1+\alpha)}{1+2\alpha}-\frac{1}{\alpha}\ln(1+2\alpha)\right]+\frac{1}{2\alpha}\ln(1+2\alpha)-\frac{1+3\alpha}{(1+2\alpha)^2}\right\}. \tag{1.5}$$

The Klein-Nishina formula is derived considering free electrons at rest. This is not the case in real situations, where the electrons involved in the interaction are bound to a nucleus and have a momentum different from zero. The effect caused by the momentum distribution of the electrons is known as *Doppler broadening* and it depends

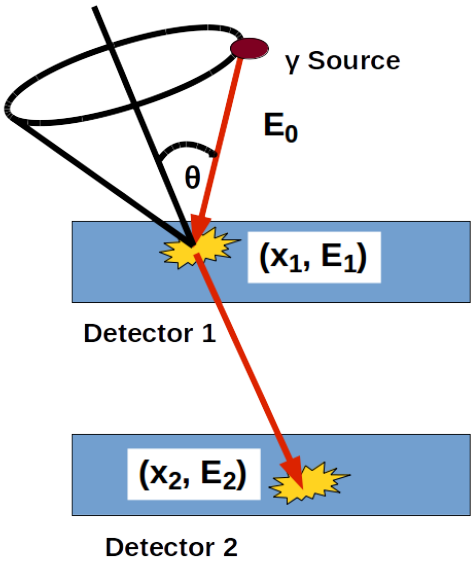

Figure 1.3: Schematic representation of a Compton camera. Photons of unknown propagation direction are Compton scattered at the first (scatter) detector and then low energy gammas are fully absorbed in the second (absorption) detector.

on the detector material, increasing with the atomic number, and on the atomic shell of the detectors, imposing a physical limit in the scattering angle uncertainty.

1.2.2 Compton camera

A Compton camera is employed to carry out Compton imaging. The most common detector configuration is based on a two-layer approach [2, 3, 4], each of them measuring the energy deposition and the interaction position of the interacting photons. Photons of unknown propagation direction are Compton scattered in the first (*scatter*) detector and then low energy gammas are fully absorbed in the second (*absorption*) detector. Both detectors are operated in time coincidence (electronic collimation), without restricting their incoming direction as mechanical collimators do and therefore eliminating the resolution-efficiency tradeoff imposed by them. A schematic representation of a Compton camera can be seen in figure 1.3.

The scattering angle θ can be calculated from equation 1.3 using the energy deposited in both detectors

$$cos\theta = 1 - m_0c^2 \left(\frac{1}{E_0 - E_e} - \frac{1}{E_0} \right). \tag{1.6}$$

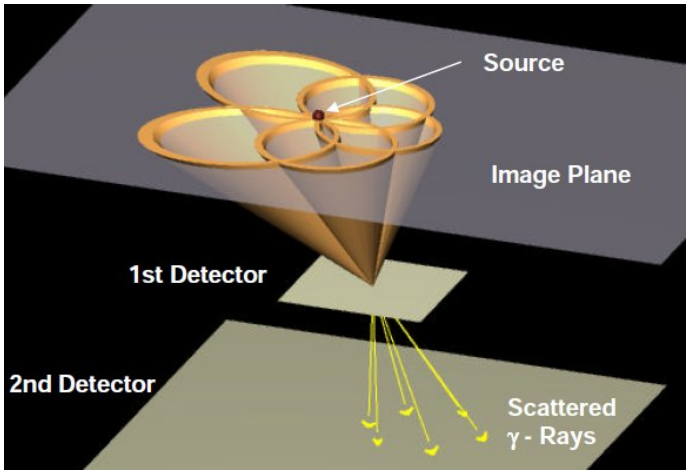

Figure 1.4: The source position is determined by the intersection of several cones.

Since only the propagation direction of the scattered photon is known, the incident direction of the incoming photon cannot be recovered univocally. However, determining the interaction positions in both detectors allows to reconstruct a cone surface. The apex of the cone corresponds to the interaction position in the scatter detector and the propagation direction of the scattered photon defines the cone axis. The half angle of the cone is the scattering angle θ and the original direction of the incoming photon could be any generatrix contained in the cone surface. From the intersection of the cones generated in several events, the source position can be determined (figure 1.4).

The spatial resolution of the Compton detector depends on the spatial resolution of both the scatter and absorption detectors, and on their relative distance. The effects of these factors have been analytically evaluated for a parallel plate Compton detector [5]. The spatial resolution of the absorption detector affects the uncertainty in the orientation of the cone axis, while the spatial resolution of the scatter detector affects both the orientation of the axis and the position on the apex. To achieve an appropriate spatial resolution, the scatter detector should be placed as close as possible to the source, and the uncertainty in the scattering angle must be minimized. The effects of the spatial resolution of the scatter and absorption detectors are minimized when the distance between them is increased [6].

For a given geometry, the scatter detector is the key in the performance of the Compton detector. The main requirements are therefore a high probability of Compton interaction, a good spatial resolution, and an excellent energy resolution, that affects the determination of the scattering angle.

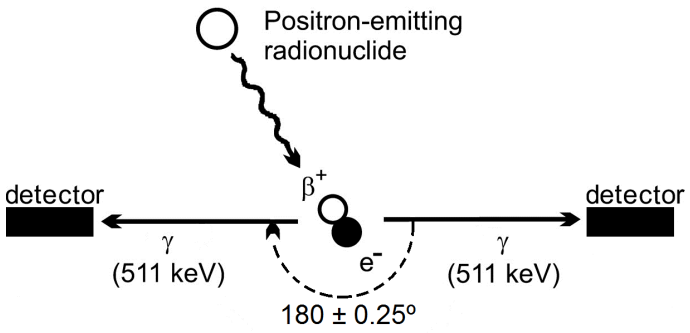

Figure 1.5: Positron emission and annihilation. Two 511 keV gamma photons are emitted in nearly opposite directions.

1.3 PET

PET is a nuclear medicine imaging technique that makes use of positron emitting radiotracers, which are specifically designed depending on the organ or tissue to be imaged [7]. The most commonly used positron emitting radioisotopes are ^{11}C, ^{13}N, ^{15}O and ^{18}F.

In PET imaging, there are different radiotracers depending on their chemical and biological properties and how they interact with the metabolism of the patient. One of the most commonly used radiotracer is 18F-fluorodeoxyglucose (FDG), which is created by adding fluorine-18 into deoxyglucose.

The most widespread application for PET has been the detection and staging of cancer, through whole-body FDG studies. FDG is also used with diagnostic purpose in several neurodegenerative diseases and dementia, epilepsy and psychiatric disorders.

1.3.1 PET physics

In PET, the radiotracers have an excess of protons and they decay through positron emission, also known as β^+ decay. A proton (p^+) is converted to a neutron (n), emitting a positron (e^+) and an electron neutrino (ν_e) in the process:

$$p^+ \rightarrow n + e^+ + \nu_e. \tag{1.7}$$

The positron emitted by β^+ decay undergoes a series of inelastic collisions as it passes through the surrounding tissues, losing its kinetic energy, until its annihilation

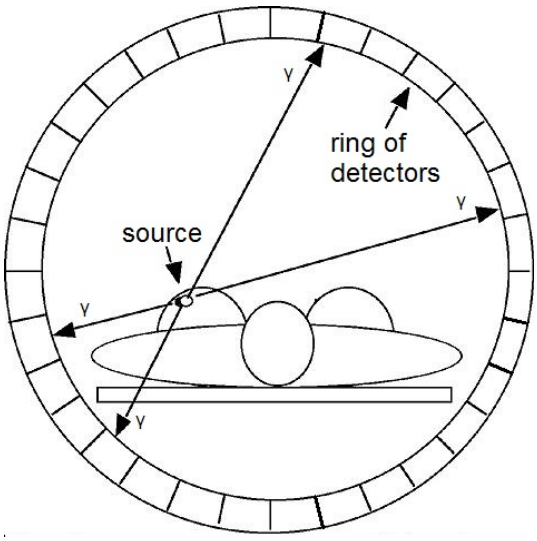

Figure 1.6: Schematic representation of a PET scanner consisting of a ring of detectors.

with an electron (its antiparticle). From this reaction, two gamma rays of 511 keV are emitted in almost opposite directions. If the momentum of the positron at the time of annihilation with the electron is different from zero, the trajectories of the two photons are not completely collinear and slightly deviate from 180°. The net distance traveled by the positron until the annihilation with an electron is known as positron range. The process of positron emission and annihilation is illustrated in figure 1.5.

1.3.2 PET scanner

For the detection of the two emitted gamma photons, a ring of detectors working in time coincidence is usually employed. The detection of two events in time coincidence defines a line, the line of response (LOR), along which the annihilation took place. From the intersection of many LORs, a map of the concentration of the radionuclide can be generated employing a tomographic reconstruction algorithm. If the detector finite size is considered, the shape of the region in which the annihilation took place is the tube-like volume connecting them, called volume of response (VOR). A schematic representation of a PET scanner can be seen in figure 1.6.

The use of electronic collimation allows to know the direction of both photons from the LOR, so there is no need to use a mechanical collimator to define (and therefore restrict) the acceptance angle, as in SPECT. The wider acceptance angle in PET translates into a gain in sensitivity two or three orders of magnitude higher than for SPECT [8].

Table 1.1: Properties of the most commonly used radionuclides in PET.

Isotope	Half-life (min) [10]	β^+ average energy (MeV) [10]	FWHM in water (mm) [9]	FWTM in water (mm) [9]
^{11}C	20.4	0.385	0.188	1.86
^{13}N	9.97	0.492	0.282	2.53
^{15}O	2.03	0.735	0.501	4.14
^{18}F	110	0.250	0.102	1.03

1.3.3 Sources of response degradation

The quality of the information available in a LOR is degraded by several physical effects related to the emission and detection of the annihilation photons: positron range, acollinearity of the emitted gamma rays, detector size and depth of interaction (DOI).

Positron range

Positron range is the distance between the place where the positron is emitted and where it undergoes annihilation with an electron. This distance ranges from a few hundred micrometers to a few millimeters and it depends on the energy with which the positron is emitted and the material through which it travels. The quantity that directly affects the spatial resolution is the effective positron range, defined as the component of the net positron displacement vector perpendicular to the line defined by the annihilation photons. The distribution of the effective positron range is characterized by a sharp peak with long exponential tails, rather than a Gaussian. For this reason, in addition to the full width at half maximum (FWHM) of the distribution, the full width at one-tenth maximum (FWTM) should be given to characterize the distribution [9]. Table 1.1 shows the half-life, the average positron energy and the effective positron range in water for the most commonly used radionuclides in PET.

Acollinearity

Due to the fact that the momentum of the positron at the time of the annihilation with the electron is different from zero, the trajectories of the two generated photons are not completely collinear and slightly deviate from 180°. The angular distribution is

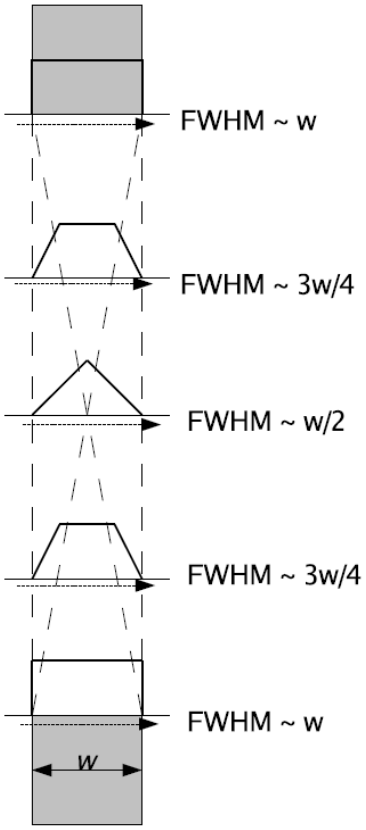

Figure 1.7: Intrinsic spatial resolution of a pair of face-to-face detectors. Figure based on [12].

approximately Gaussian with a FWHM of 0.5° [11]. The effect on spatial resolution due to acollinearity R_{acol} can be expressed as

$$R_{acol} = 0.5 \cdot D \cdot \tan(0.25^\circ) = 0.0022 \cdot D, \tag{1.8}$$

where D is the diameter of the PET scanner or the distance between detectors.

Detector size

The coincidence response function (CRF) is the probability that a point source, which is moved perpendicular to the LOR corresponding to a detector pair, is detected as a coincidence event. The size of the detectors determines the precision with which an annihilation event is located inside the VOR and therefore the CRF. PET scanners typically use identical detectors around the ring, so the CRF of a pair of any of these is

symmetric about the midpoint between the two. For LORs near the center of the field of view (FOV) the CRF forms a triangle at the center of the FOV and becomes rectangular near the ends. At intermediate positions the CRF is trapezoidal in shape, with a plateau whose width is equal to the distance between two lines joining opposite sides of the two detectors. The width of the base of the CRF is the same as the detector width *w* [12]. Figure 1.7 shows the CRF at different positions for a pair of face-to-face detectors of the same size. The spread of the CRF is given by its FWHM and is a measure of intrinsic resolution. Resolution is highest when the CRF is triangular, in the centre, and degrades as the function spreads out to be trapezoidal and, finally, rectangular. For LORs located away from the centre of the FOV, where the detector pairs are not directly facing each other, the shape of the CRF varies due to the effect of the depth of photon interaction in the detector and becomes asymmetric.

Depth of interaction

A degradation of the intrinsic spatial resolution, known as parallax error, is caused by the uncertainty regarding the depth of interaction (DOI) when a photon enters a detector at an oblique angle [13]. Figure 1.8 illustrates the problem. As it has been just explained (figure 1.7), the spatial resolution for a source located near the center of the scanner is determined by the width of the detector element, R_{det}=*w/2*. However, for a source located away from the center, the apparent width of the detector element becomes

$$w' = w\cos\theta + l\sin\theta, \tag{1.9}$$

where *w*, *l* and θ are the width, length and inclination angle of the detector, respectively. The apparent change in width results from the angulation between the detectors and from the lack of knowledge about the depth at which an interaction has occurred within the detector crystal. The FWHM of the spatial resolution then becomes R'_{det}=*w'/2*. Using equation 1.9:

$$R'_{det} \approx \left(\frac{w}{2}\right)\cdot\left[\cos\theta + \left(\frac{l}{w}\right)\sin\theta\right] \approx R_{det}\cdot\left[\cos\theta + \left(\frac{l}{w}\right)\sin\theta\right]. \tag{1.10}$$

It can be seen from this equation that the DOI effect is described by a multiplicative factor applied to the value of detector resolution at the midpoint between a pair of directly opposed detectors. Thus, degradation increases with the scanner radius.

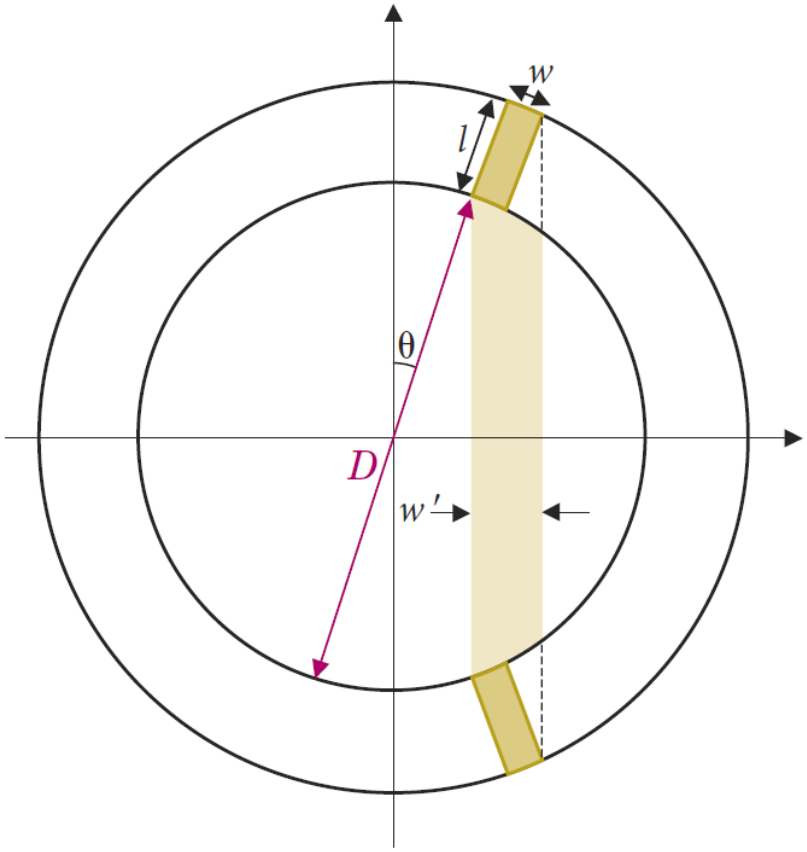

Figure 1.8: Uncertainty regarding the depth of interaction (DOI) caused by a photon entering a detector at an oblique angle. Figure based on [13].

Chapter 2

Detectors for medical imaging

Detectors based on a scintillator crystal optically coupled to a photodetector are the most widely used radiation detectors in medical physics applications for the detection of gamma rays and the type employed in this thesis. The crystal produces scintillation light when radiation interacts with it and the photodetector converts the scintillation light into an electrical signal. In this chapter, a brief overview of the main characteristics of these components is given.

The position determination method applied to the prototypes was not developed inside the framework of this thesis. Nevertheless, since it was used in this thesis, a brief explanation is given.

2.1 Scintillators

A scintillator is a material that emits light when ionizing radiation interacts with it. In medical physics, one of the most common ways to produce ionizing radiation is through gamma rays. When a gamma ray photon interacts with a scintillator material, the scintillator absorbs its energy totally or partially, converting the deposited energy to visible and ultraviolet light [14].

The two important interaction mechanisms for detecting gamma photons in medical physics are photoelectric absorption and Compton scattering. If the photon interacting with the scintillator undergoes photoelectric effect, the entire energy of the gamma photon is transferred to the release of a photoelectron. The place where the interaction takes place will produce a scintillation center. If the photon interacting with the scintillator undergoes Compton scattering, only part of the energy of the incident gamma ray will be transferred to the electron of the scintillator. The scattered photon can

then escape from the scintillator material or interact again in it suffering new Compton scattering or photoelectric absorption. For this reason, photons undergoing Compton scattering can produce several scintillation centers, which will affect the interaction position determination in the form of position blurring.

Scintillator materials show the *luminescence* property. Three different types of luminescence can be distinguished. In *fluorescence*, the incoming energy is absorbed and promptly re-emitted in the form of light. If the excited state is metastable, the re-emission is delayed some time and it takes place in longer wavelenghts light than fluorescence. This process is called *phosphorescence* or *afterglow*. Finally, in *delayed fluorescence* the re-emission is also delayed some time but it takes place in the same wavelenghts as prompt fluorescence. In phosphorescence and delayed fluorescence, the time between absorption and re-emission can range from microseconds to hours depending on the material.

There are several types of scintillating materials: organic crystals, organic liquids, plastics, inorganic crystals, gases and glasses. Each of them has different properties and is therefore suitable for a different application. Inorganic scintillators offer a high cross-section to gamma ray photons and a high light yield, making them the perfect candidates for medical imaging detectors.

A good scintillation material should satisfy the following properties [14]:

- High scintillation efficiency to convert the incident radiation energy to prompt fluorescence, avoiding or reducing as much as possible the appearance of phosphorescence and delayed fluorescence.
- The light output should be proportional to the deposited energy over a range as wide as possible. Otherwise, the energy resolution would worsen.
- High light yield (number of emitted scintillation photons per MeV absorbed energy). A high light yield ensures a high number of photons reaching the surface of the photodetector. This implies a good energy, timing and position resolution.
- The optical self-absorption of the scintillation material should be minimal. This means that it should be transparent to its own radiation in order to allow transmission of the light. In this sense, the scintillator can be surrounded by a reflector to prevent light from escaping and therefore increase the number of photons reaching the photodetector.

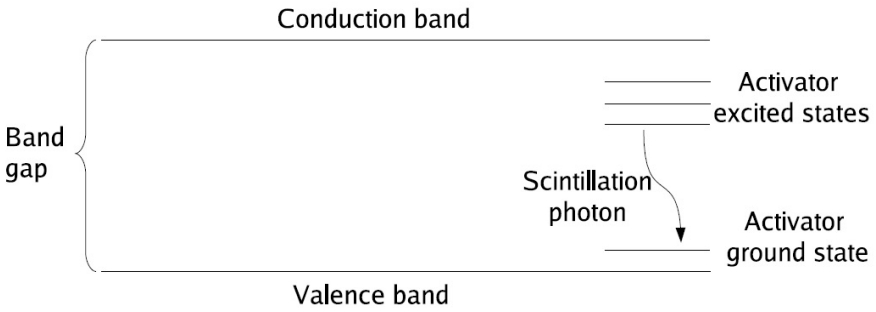

Figure 2.1: Energy band structure of an inorganic scintillator crystal with activators. Figure based on [14].

- The emission spectrum should overlap with the spectral sensitivity of the photodetector.
- The decay time should be short. A fast decay time allows a high count rate of the detector since the dead time is reduced. Besides, a fast scintillator also improves the timing capabilities of the detector.
- The scintillation material should have a high density for a high absorption probability and a high atomic number for a large fraction of events undergoing photoelectric absorption.

2.1.1 Inorganic scintillators

The scintillation mechanism in inorganic scintillators is determined by the electronic band structure and the energy states of its crystal lattice. The mechanism is illustrated in figure 2.1. Electrons in the *valence band* are bound at lattice sites, but electrons in the *conduction band* have enough energy to move through the crystal. In pure crystals, electrons can never be found in the *forbidden band*. Ionizing radiation interacting with the scintillator may cause electrons from the valence band to absorb sufficient energy to jump to the conduction band, leaving a hole in the valence band. During the de-excitation process, the electron returns to the valence band emitting a photon. In pure crystals, this process is inefficient and the typical gap widths are such that the photons released are too energetic to be in the visible spectrum.

To overcome this problem, small amounts of impurities, called *activators*, are introduced into the scintillator material. These activators change the existing energy band structure, creating energy states within the forbidden gap through which the

Table 2.1: Properties of some used scintillators for PET.

	NaI	**BGO**	**LYSO:Ce** [15]	**$LaBr_3$:Ce** [16]
Peak emission [nm]	410	480	420	380
Light yield [ph/MeV]	41000	7000	32000	63000
Density [g/cm^3]	3.67	7.13	7.1	5.08
Z_{eff}	50	74	65	47
Decay time [ns]	230	300	41	16
Index of refraction	1.85	2.15	1.81	1.9
ΔE/E at 662 keV [%]	6.0	9.0	8.0	2.9
1/μ at 511 keV [mm]	25.9	11.6	12	21.3
Hygroscopic	Yes	No	No	Yes

electron can de-excite back to the valence band. The energy of this transition is less than the energy required to elevate an electron from the valence band to the conduction band, releasing photons in the visible light spectrum. For this reason, scintillators are transparent to scintillation light, since the emission and absorption spectra do not overlap and self-absorption by the crystal is therefore minimal. These de-excitation sites are the *luminescence centers* (also called *recombination centers*) from which scintillation can take place. The energy structure of the luminescence centers in the crystal lattice determines the emission spectrum of the scintillator. The time characteristics of the emitted scintillation light is determined by the decay time of electrons from an excited state to the valence band, which eventually depends on the scintillation material and the impurities chosen as activators.

The two inorganic scintillator crystals employed in this thesis are *LYSO* (Lutetium Yttrium Oxyorthosilicate, $Lu_{1.8}Y_{0.2}SiO_5$) and *LaBr*$_3$ (Lanthanum (III) Bromide). Both of them are co-doped with Cerium (Ce^{3+}) as an activator. This ion is an efficient luminescence centre with a fast response and an effective atomic number Z_{eff} = 58. It has one electron in the 4f state that is excited to the empty 5d shell through interaction with radiation. The subsequent de-excitation by emitting a scintillation photon will occur by an allowed 5d to 4f electric dipole transition with a decay time in the range of 20 to 80 ns [14]. *NaI* (Sodium Iodide) and *BGO* (Bismuth Germanium Oxide, $Bi_4Ge_3O_{12}$) are inorganic scintillators that were commonly used in PET for the detection of gamma rays before the emergence of LYSO. The main characteristics of these inorganic scintillator crystals can be found in table 2.1.

LYSO is nowadays widely used in commercial clinical PET scanners as well as in preclinical small animal PET scanners. It has a high detection efficiency, a high light yield and a short decay time. It is not hygroscopic and shows good mechanical properties. The main drawback of LYSO is the presence of the ^{176}Lu isotope, with a half-life of 4×10^{10} years. This isotope adds a natural radiation background in spectroscopy measurements. In PET detectors, this effect is reduced since the detectors are operated in time coincidence mode.

$LaBr_3$ is a relatively new scintillator [17]. It has a very high light yield, a very short decay time and a very good energy resolution. Compared to other scintillator crystals, $LaBr_3$ has a lower photoelectric absorption probability and a higher Compton probability due to its lower effective atomic number Z_{eff}. The main drawback of $LaBr_3$ is its hygroscopicity, requiring an hermetic housing and careful handling.

2.2 Photodetectors

The photodetector converts the light coming from the scintillator into an electrical signal. This signal can be analyzed to obtain information about the incident radiation, such as the energy deposited in the scintillator or the position where the interaction of the gamma ray inside the scintillator took place.

Photomultipliers tubes (PMTs) have been the most widely used photodetector for the detection of gamma rays. In the last years, a new kind of semiconductor photodetector, called Silicon Photomultiplier (SiPM), has gained a lot of attention because of its interesting properties. The detectors developed in this thesis employ SiPMs as photodetectors.

2.2.1 Photomultiplier tubes

A photomultiplier tube is a photodetector consisting of a light transmitting window (usually glass), a photosensitive layer (the photocathode), a series of electrodes (dynodes) and an anode, all housed in an envelope with high vacuum conditions inside. A schematic view of a PMT can be seen in figure 2.2.

The first component that scintillation light interacts with is the light transmitting window, that is usually made of glass. The index of refraction of the transmitting window is typically 1.5, meanwhile the index of refraction of inorganic scintillators is around 1.8 or more. This difference produces losses of photons because of optical

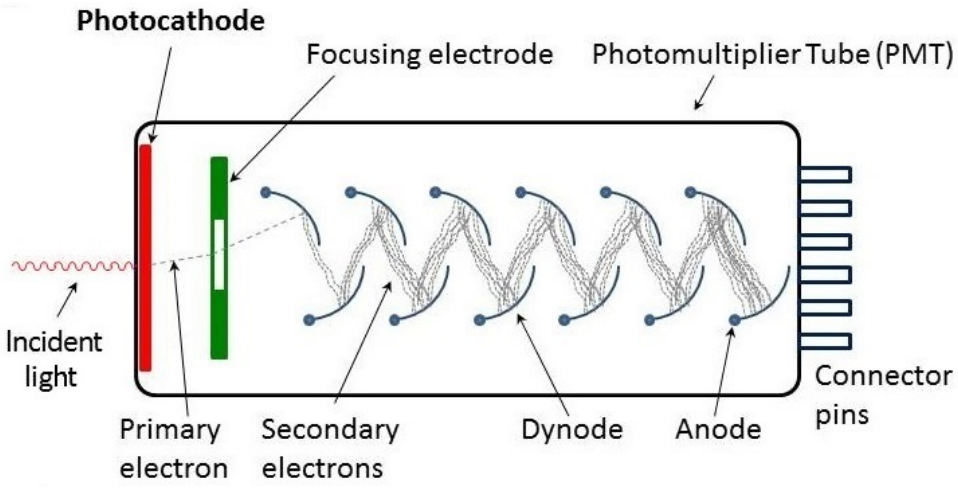

Figure 2.2: Schematic view of a PMT. Reproduced and modified from [18].

refraction. Optical grease or glue is commonly used to optically couple the scintillator crystal with the photodetector and attenuate this problem. The photocathode converts part of the incident photons into low-energy electrons by the photoelectric effect. The photocathode essentially determines the light response characteristic of the PMT as a function of the wavelength. The probability that the photocathode liberates a photoelectron after the interaction of an incident photon is the *quantum efficiency* (QE). The QE depends on the wavelength of the incident light as well as on the properties of the transmitting window and photocathode. After the release of photoelectrons from the photocathode, the photoelectrons are accelerated through a vacuum chamber under very high voltage to the first dynode. The impact of these photoelectrons in the dynode liberates secondary electrons, which in turn, are accelerated towards the next dynode where more electrons are released and further accelerated. The repeated structure creates an electron cascade which is finally collected by the anode in the form of a current pulse. The gain of a PMT is determined by the number of dynodes and the voltage difference between the photocathode and the anode. Typical PMT gains are in the order of 10^7-10^{10}. Finally, the time response of a PMT is primarily determined by the time required for the electrons to travel from the photocathode to the anode.

It is worth to mention the existence of a type of PMTs called multianode PMTs (MAPMTs). MAPMTs consist of a focusing mesh of metal channel dynodes with minimal dead space. Each dynode cascade system (channel) is distributed on the MAPMT surface and has its own anode. In this way, each channel of the MAPMT

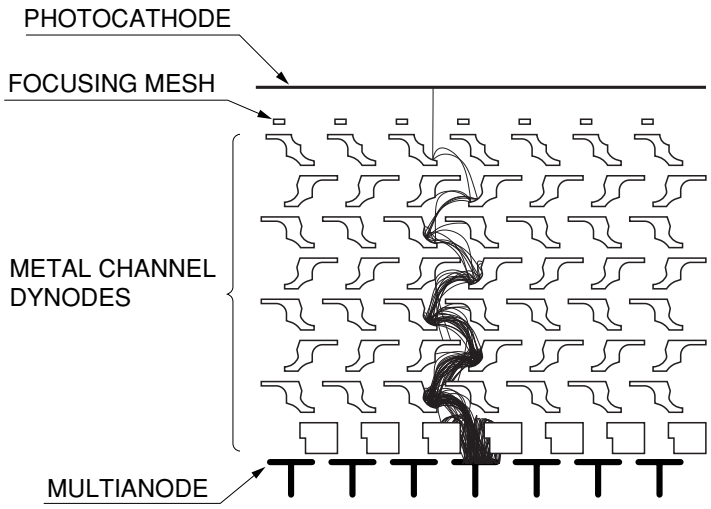

Figure 2.3: Schematic view of a MAPMT. Reproduced from [19].

performs as an independent PMT, being position sensitive to the spatial distribution of the scintillation light from the crystal. A schematic view of a MAPMT can be seen in figure 2.3.

2.2.2 Semiconductor detectors

Semiconductor detectors present an electronic band structure consisting of a *valence band*, a *forbidden energy gap* and a *conduction band*. Electrons in the conduction band are detached from their parent atoms and are free to move around the material. Electrons in the valence band are more tightly bound and remain associated to their respective lattice atoms.

Silicon is a semiconductor material used in medical physics as a photodetector. It is a tetravalent atom, so it has four valence electrons to create four covalent bonds, forming an atomic crystal. In solid-state physics, an electron hole (usually referred to simply as a hole) is the absence of an electron at a position where one could exist in an atom or atomic lattice. In pure silicon, the number of holes is equal to the number of electrons in the conduction band. Doping a semiconductor with small amounts of impurities modifies its lattice, introducing allowed energy states within the band gap. Depending on the silicon dopant, two types of silicon can be created, *n-type* or *p-type*.

N-type doping is achieved employing a pentavalent dopant. It has five electrons in the valence band so four covalent bonds will be formed, leaving one free electron. This

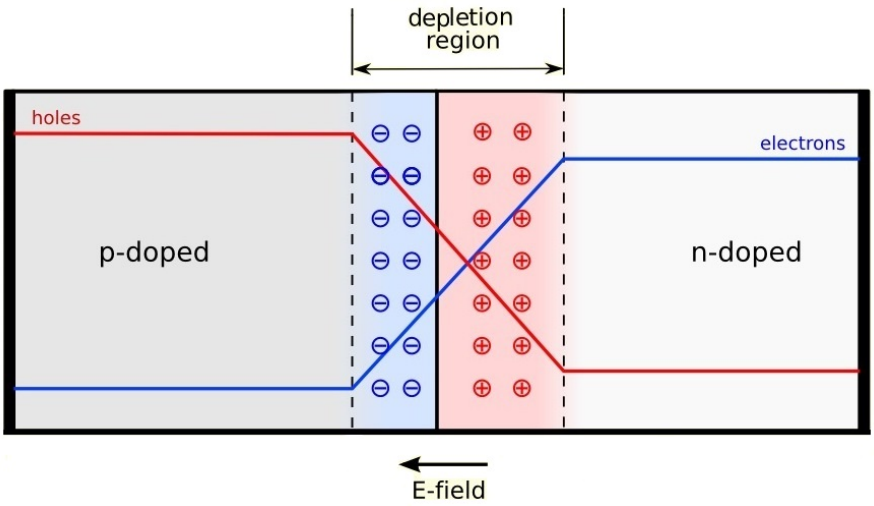

Figure 2.4: Scheme of a p-n junction. Reproduced and modified from [20].

free electron will create a new state in the energy gap, close to the conduction band. In n-type configuration, electrons are the majority charge carriers. Impurities typically used to create n-type silicon are arsenic (As) or phosphorus (P).

P-type doping is achieved employing a trivalent dopant. It has three electrons in the valence band so three covalent bonds will be formed, generating an excess of holes in the crystal. This excess of holes will create a new state in the energy gap, but this time close to the valence band. In p-type configuration, holes are the majority charge carriers. Impurities typically used to create p-type silicon are gallium (Ga) or boron (B).

A p-n junction consists of n-type silicon and p-type silicon placed into adjacent regions on a silicon substrate. The difference in electron and hole concentrations causes diffusion between the regions, producing an electric field E which opposes the diffusion process. The diffusion continues until the electric field is strong enough to balance it, creating a stable state in which a thin layer around the junction is left without free carriers. The layer is called *depletion region*. A schematic view of a p-n junction can be seen in figure 2.4.

Photodiodes

A photodiode is a p-n junction sensitive to photons. They are usually operated in *reverse bias* configuration, with the p-type region connected to the negative terminal and the n-type region connected to the positive terminal (see figure 2.5). When a bias voltage is applied, the electrons of the n-type region will move to the positive terminal

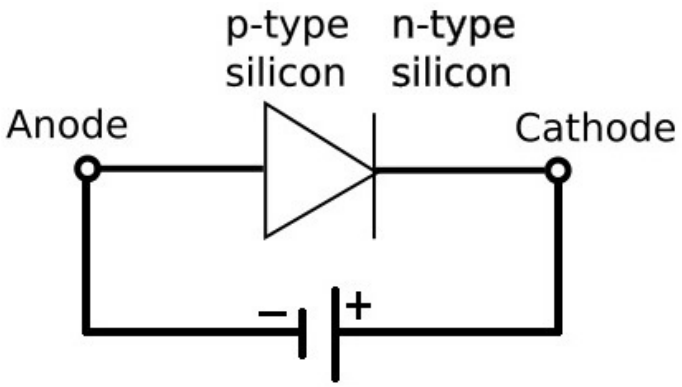

Figure 2.5: Photodiode working in reserve bias configuration.

meanwhile the holes of the p-type region will move to the negative terminal, leaving the depletion region void of charges. When a photon with sufficient energy interacts in the depletion region, electron-hole pairs are created. The electron-hole pairs are swept away of the depletion region by the electric field resulting from the applied voltage: holes move toward the anode and electrons toward the cathode, producing a current signal. Conventional photodiodes have no internal gain, so the current signals generated by incident light have small amplitudes and therefore electronic noise is its major drawback. For these reasons, photodiodes are not used as photodetectors.

Avalanche photodiodes

An Avalanche Photodiode (APD) is a kind of photodiode that is operated at a bias voltage higher than photodiodes, but still below the *breakdown voltage*. The breakdown voltage (V_{bd}) is the value of the reverse bias at which the p-n junction breaks down and starts to conduct. Optical photons interacting in the sensitive volume of the photodetector produce electron-hole pairs. At these values of bias voltage, electrons are sufficiently accelerated by the electric field to create additional electron-hole pairs along the collection path due to *impact ionization*. The electrons of these secondary carriers are then themselves accelerated and collide with further atoms, releasing more electron-hole pairs and subsequently repeating the process (*avalanche multiplication*), acting as an internal gain stage. This gain pulls the signal up from the electronic noise level and allows good energy resolution compared to conventional photodiodes. Typical APD gain is in the range of 10^2 to 10^3.

2.2.3 Silicon Photomultipliers

A Silicon Photomultiplier (SiPM) consists of a densely packed matrix of light-sensitive microcells all connected in parallel (see figure 2.6). Each microcell is an APD operated at a bias voltage above the breakdown voltage (*Geiger mode*). In Geiger mode, the internal electric field of each microcell becomes so high that when optical photons interact with it, both electrons and holes are involved in the multiplication process, creating a self-sustaining avalanche. A quenching resistor (R_q) is employed to stop the avalanche and avoid damage to the device. C_d is the diode capacitance introduced by the depletion region. Each microcell has three different states: quiescent mode, discharge phase and recovery phase.

In quiescent mode, the diode is reversed biased to

$$V_{bias} = V_{bd} + V_{ov}, \tag{2.1}$$

where V_{ov} is the overvoltage (the excess bias beyond V_{bd}). When an avalanche occurs (discharge phase), the current flowing through the microcell is quenched through the series resistor R_q. This quenching process limits the diode current during the breakdown and reduces the reverse voltage applied to C_d from V_{bias} to a value below its V_{bd}, effectively stopping the avalanche. In the recovery phase, C_d recharges back to V_{bias} through R_q and the microcell returns to the quiescent mode.

The signal obtained in a microcell due to an avalanche is always the same, independently of the energy and the number of the incoming photons. Each microcell detects photons identically and independently, functioning as a photon-triggered switch with a binary ”on” or ”off” response. The energy information about the incoming photon flux is obtained by adding up the signals of all microcells since they are connected in parallel. Typical microcell size ranges from 20×20 μm^2 to 100×100 μm^2.

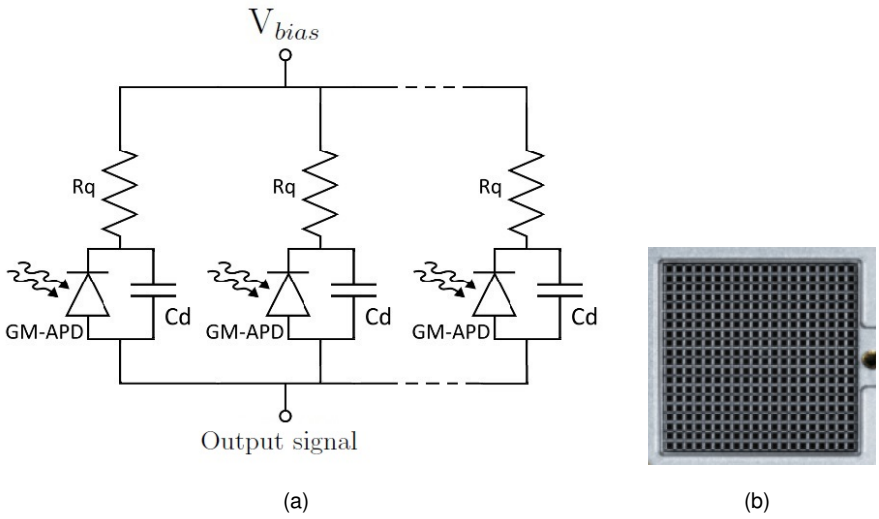

Figure 2.6: (a) Schematic representation of a SiPM. The microcell capacitance is represented by C_d and the quenching resistor by R_q. (b) Detail of the microcell array structure in a SiPM from Hamamatsu.

Photon detection efficiency

The photon detection efficiency (PDE) of a silicon photomultiplier is the statistical probability that an incoming photon will produce an avalanche and therefore a measurable output signal. The PDE is a function of wavelength and V_{bias}:

$$PDE(\lambda, V_{bias}) = QE(\lambda) \cdot P_{av}(V_{bias}) \cdot FF, \tag{2.2}$$

where *QE* is the quantum efficiency of silicon, P_{av} is the avalanche initiation probability in the depleted region and *FF* is the geometric fill factor. The quantum efficiency is the probability that an incident photon will produce an electron-hole pair by photoelectron conversion. The quantum efficiency of silicon depends on the wavelength. The geometrical fill factor represents the ratio of the effective sensitive detection area with respect to the total detector area. Some of the microcell area is dedicated to quenching resistors and electrical pads, which are insensitive to light. For this reason, SiPMs with big microcells have a high fill factor meanwhile small microcells have a low fill factor. Typical fill factor values range from 25% to 75%, depending on the microcell size. The quantum efficiency *QE* and the avalanche initiation probability P_{av} can be designed to be close to unity, so the fill factor *FF* becomes a highly relevant parameter for the PDE. Figure 2.7 shows a typical PDE curve as a function of the overvoltage.

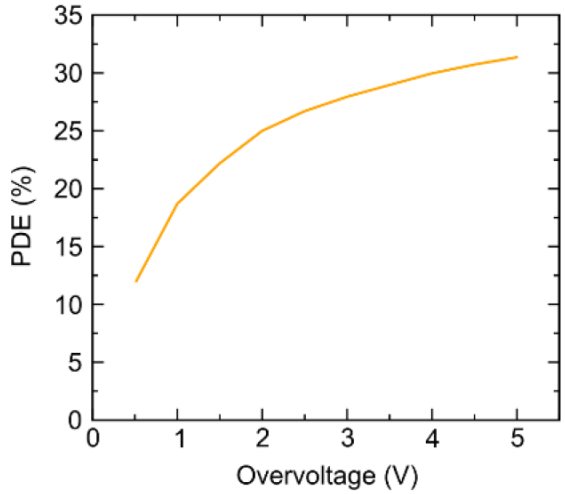

Figure 2.7: Photon detection efficiency (PDE) as a function of the overvoltage. 560 nm incident light. Plot from AdvanSiD [21].

Gain

The gain of a microcell (and therefore the SiPM) is the ratio between the output charge over the charge of an electron. The output charge can be obtained from the overvoltage V_{ov} and the microcell capacitance C_d:

$$G = \frac{C_d \cdot V_{ov}}{q}. \tag{2.3}$$

Assuming C_d constant for $V_{bias} > V_{bd}$, gain increases linearly with the overvoltage due to the widening of the depletion region. Since V_{ov} = V_{bias} - V_{bd} and V_{bd} strongly depends on temperature, both V_{bias} and temperature need to be stable for constant gain. Typical SiPM gain is in the order of 10^5-10^6. Figure 2.8 shows a typical gain curve as a function of the overvoltage. The slope represents C_d/q.

Dynamic range

In Geiger mode, the output charge generated by a microcell due to an avalanche breakdown is almost the same in all the microcells of a SiPM. For this reason, the total output charge in a SiPM is the sum of the charge produced by the firing microcells at that moment. Due to the limited number of microcells in a SiPM, the response to an incoming photon flux obeys a Poisson distribution rather than a linear dependency. The output of a SiPM is only linear when the number of incident photons is significantly

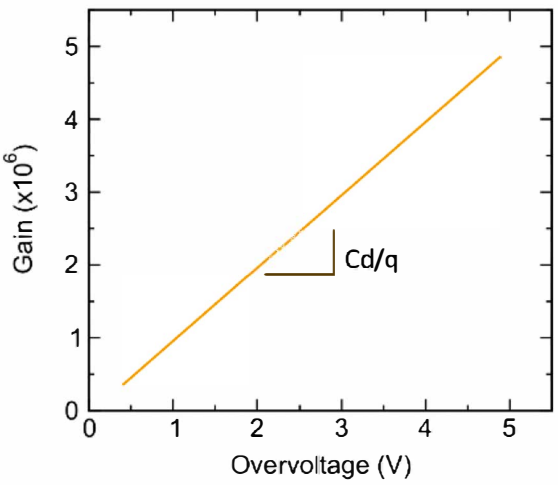

Figure 2.8: SiPM gain as a function of the overvoltage. The slope is the diode capacitance C_d. Plot from AdvanSiD [21].

smaller than the number of available cells. The SiPM output begins to saturate when the number of detected photons begins to approach the number of microcells. Above a certain signal level, and before saturation, the SiPM response becomes sub-linear. As the number of incident photons per microcell per unit of time increases, the probability that two or more photons will interact in the same microcell at the same time increases as well. The output signal is completely saturated when no microcells are available to detect incoming photons and remains saturated until some of the microcells recover back to their quiescent mode.

The number of fired microcells as a function of the number of incident photons can be approximated by the following expression

$$N_{fired} = N_{cells} \cdot (1 - exp(-\frac{PDE(\lambda, V_{bias}) \cdot N_{ph}}{N_{cells}})), \tag{2.4}$$

where N_{fired} is the number of fired microcells, N_{cells} is the number of SiPM microcells and N_{ph} is the number of incident photons. This equation is not exact, since it does not take into account the recovery time of a microcell and it assumes that a microcell can only fire once during a scintillation event.

Large microcell sizes imply a low dynamic range since there are less cells per unit area, but a high PDE due to a larger fill factor. Small microcell sizes imply a high dynamic range, but a low PDE. The choice of the microcell size will therefore depend on the particular application.

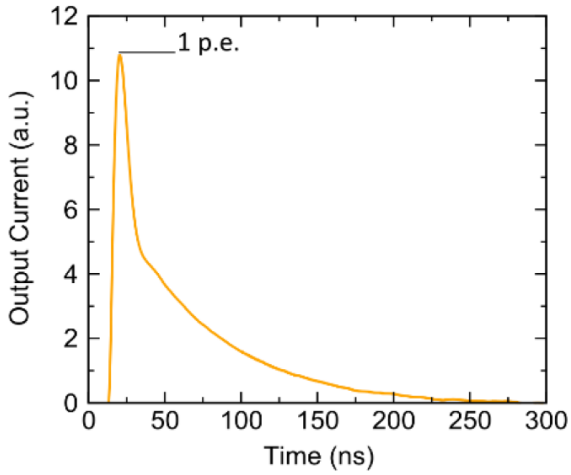

Figure 2.9: Current pulse produced by a microcell in response to photon absorption. The pulse has a very fast rising edge and a slower trailing edge (microcell recovery). Plot from AdvanSiD [21].

Recovery time

The discharge and recovery process of a microcell produces a typical current signal as the one shown in figure 2.9. Its amplitude is defined to be 1 p.e. (photo-electron). The rising edge corresponds to the discharge phase and the slower trailing edge corresponds to the recovery phase. The recovery time is the time needed to reestablish the electric field of a fired microcell. The recovery time constant τ of a microcell is proportional to the quenching resistance R_q and the microcell capacitance C_d:

$$\tau = R_q \cdot C_d. \tag{2.5}$$

The microcell capacitance depends on its area, so the recovery time will depend on the microcell size. Large microcell sizes have significantly longer recovery times than small microcell sizes.

During recovery the voltage across the microcell is increasing from V_{bd} to V_{bias}, following the exponential recharge of C_d through R_q. Consequently, the detection efficiency goes from zero to the value at V_{ov} with the same time constant. Therefore, the microcells are not completely blind during recovery, they feature increasing detection efficiency.

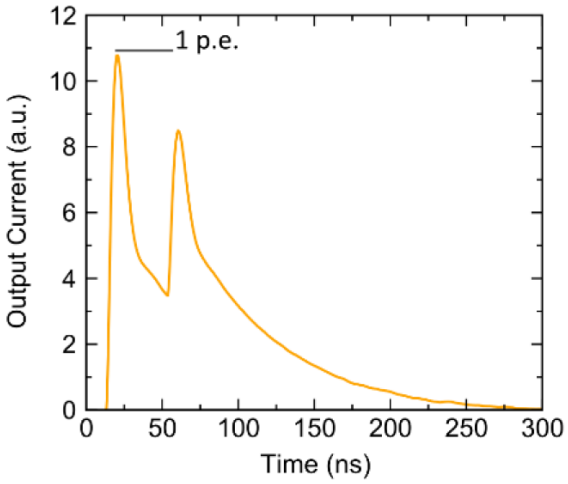

Figure 2.10: Afterpulse in a microcell. The same microcell fires again during the recharge phase due to a carrier being released from a previously filled silicon trap. To note that the amplitude of the afterpulse is $<$1 p.e. since C_d has not recharged to V_{bias} yet when afterpulse occurs. Plot from AdvanSiD [21].

Dark count rate

Spurious generation of free carriers inside the active region of a microcell initiates an avalanche with an output signal indistinguishable of an output signal generated by a photoelectron. These free charge carriers are mainly due to thermal generation or tunneling effect, being produced even in absence of light and therefore receiving the name of dark noise or dark event. The number of dark events per unit of time is the *dark count rate* (DCR) and it is usually expressed in Hz (typically kHz or MHz) or counts per second (cps). The DCR is the main source of noise in a SiPM and it can not be completely removed, forming a contribution to the measured signal and ultimately limiting the smallest signal that can be detected. The DCR increases with overvoltage, temperature, microcell size and overall detector area.

Afterpulsing

Doping a semiconductor with impurities creates lattice defects inside the silicon wafer. Electron and holes generated after an avalanche can be trapped in those semiconductor defects, having some probability to be released after a characteristic time. Typical release times range from few ns to several hundreds ns. The released carriers might produce a secondary avalanche in a process called *afterpulsing*. The net

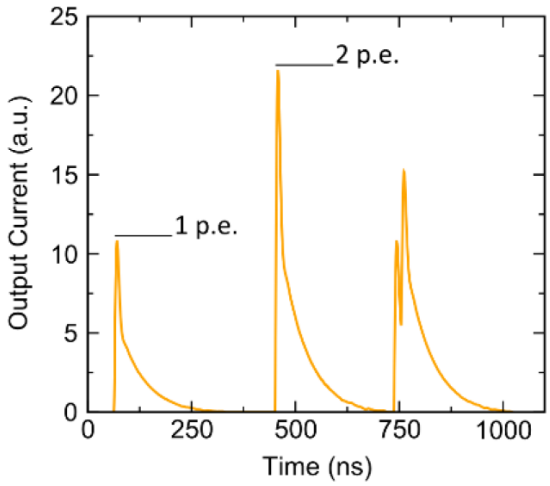

Figure 2.11: Optical crosstalk in SiPMs. From left to right: a single-cell signal (1 p.e.), a direct crosstalk signal (2 p.e., two cells firing at the same time), and a delayed crosstalk (a second cell fires few nanoseconds after a first one). Plot from AdvanSiD [21].

effect is that a new current pulse is generated on the tail of the original current pulse, as it can be seen in figure 2.10. The amplitude of the afterpulse is $<$1 p.e. since C_d has not recharged to V_{bias} yet when afterpulse occurs. Afterpulsing probability increases more than linearly with the overvoltage and quadratically with the cell size. Afterpulses represent a source of correlated noise, since it is originated from an existing pulse.

Optical crosstalk

An additional source of correlated noise in a SiPM is *optical crosstalk* between neighboring microcells. During avalanche multiplication, optical photons are emitted. These photons may reach adjacent microcells and initiate an avalanche there, generating a signal unrelated to the original one but indistinguishable from it. This signal will be integrated with the original one, resulting in a misinformation of the number of detected incoming photons and limiting the photon counting capabilities of the SiPM. *Direct optical crosstalk* occurs when an emitted photon reaches the active region of another cell triggering an additional avalanche practically at the same time of the original avalanche. The result is the double pulse shown in the second signal of figure 2.11. *Delayed optical crosstalk* occurs when photons are re-absorbed in the inactive regions of the SiPM. The generated electron (or hole) must then diffuse to the active region of a cell before being able to trigger an avalanche. The correlated pulse has

therefore a certain time delay (in the order of few ns) with respect to the original one. The result is the third signal of figure 2.11. The crosstalk depends on the overvoltage and the distance between surrounding microcells.

2.3 Position determination

The determination of the interaction position of the gamma rays is a critical issue with continuous crystals and it represents a challenge due to the intrinsic characteristics of the crystal itself.

In this thesis, a method based on the solid angle subtended by the interaction position with the photodetector elements, including the reflections of the photons on the sides of the crystal, was employed. As mentioned before, the algorithm was not developed in this thesis and it is fully explained in [22]. It is based on the number of photons arriving to each pixel from a light source, which is the generation point of optical photons in the scintillator crystal, as a consequence of the energy deposited of the gamma rays. The model to estimate the number of optical photons detected in each pixel is

$$np_i = C_{est} + A_0\Omega(x,y,z) + A_0\sum_j \Omega(x_j,y_j,z_j), \tag{2.6}$$

where np_i is the number of detected optical photons in pixel i, C_{est} is a constant that represents the contribution of the reflected photons on the diffuse reflector around the crystal, A_0 represents the total number of optical photons produced by the light source and $\Omega(x,y,z)$ represents the solid angle subtended by pixel i from the light source located at (x,y,z). The last two terms represent the number of photons impinging in pixel i. $A_0\ \Omega(x,y,z)$ represents the number of photons impinging directly the pixel and $A_0\ \sum_j \Omega(x_j,y_j,z_j)$ the number of photons that are reflected in any of the five sides of the scintillator that are not coupled to the SiPM. This mirror-like internal reflections are modelled as if there was a virtual source at a symmetric position on the other side of each surface. The difference between the real number of detected photons and the estimation performed by the model is optimized using a non-linear least squares minimization.

The main advantage of this method is that no previous calibration is needed and in addition it can provide the depth of interaction (DOI) in the crystal.

Chapter 3

Detector based on SiPMs and continuous $LaBr_3$ crystals for a Compton telescope

3.1 Introduction

Hadron therapy is a cancer treatment technique based on the irradiation of tumours with light ions, generally protons or carbon ions. During treatment, beam particles excite nuclei in the patient and secondary particles are emitted. Prompt gammas are generated from nuclear de-excitation in a characteristic spectrum, being most abundant in the energy range from 1 to 7 MeV [23]. Since the prompt gammas production distribution is closely correlated to the absorbed dose and their emission takes place within nanoseconds of irradiation [24, 25], their detection can be used for real time treatment delivery assessment.

Collimated [26] and Compton cameras are being investigated as possible candidates to locate the origin of the prompt gammas emitted during hadron therapy treatments. Among these two types of cameras, Compton cameras offer a higher efficiency and 3D information, along with the advantage of discarding the negative impact of passive collimator in terms of weight and signal attenuation. Several research groups are investigating the application of Compton cameras to range verification in hadron therapy [6, 27, 28, 29, 30, 31, 32].

The ENVISION (European NoVel Imaging Systems for ION therapy) European project [33] aimed to develop novel devices for the detection of prompt gammas employing Compton cameras based on different detector approaches such as silicon

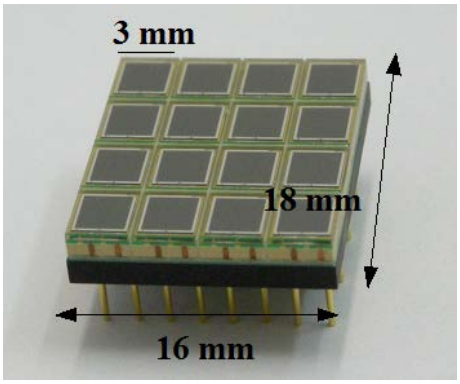

Figure 3.1: MPPC from Hamamatsu Photonics model S11064-050P composed of 16 elements of size 3 mm $\times$ 3 mm.

[6] and CZT (Cadmium Zinc Telluride) [34] detectors. Another detector approach was developed at IFIC-Valencia, consisting of a Compton telescope (multilayer Compton camera) based on several planes of continuous $LaBr_3$ crystals coupled to SiPM arrays. $LaBr_3$ meets all the requirements mentioned in section 1.2.2 and combined with the compactness of SiPMs make these materials suitable candidates for most Compton imaging applications.

A first prototype of such a detector was assembled. In this chapter, the results of the characterization and coincidence tests carried out to assess the performance and the operability of the proposed technology are presented.

3.2 Detector description

The detector planes employed in this proof-of-concept of the Compton telescope consisted of a continuous $LaBr_3$ crystal coupled to a 16-channel SiPM array.

3.2.1 SiPM array

The SiPM employed was a Multi Pixel Photon Counter (MPPC) from Hamamatsu Photonics, model S11064-050P. This MPPC array was the first SiPM array available at the time these tests started. It was a SiPM array consisting of 16 (4 $\times$ 4) channels. Each channel had an effective area of 3 $\times$ 3 mm^2 and contained 3600 microcells of 50 μm $\times$ 50 μm size. The pitch was 4.05 mm in one direction and 4.5 mm in the other direction. The external dimensions of the device were 16 $\times$ 18 mm^2. Due to the gaps

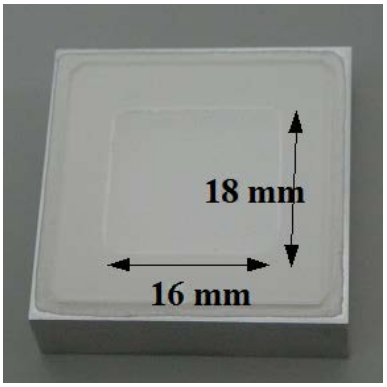

Figure 3.2: $LaBr_3$ crystal from Saint-Gobain Crystals of $16\times18\times5$ mm^3 surrounded by reflective material and encapsulated in an aluminium housing.

between the detector elements, this MPPC array had a 50% loss of active area. A picture of the MPPC array can be seen in figure 3.1.

The MPPC array was connected to a custom-made printed circuit board (PCB) for bias and mechanical support. The PCB routed the signal coming from each pixel to the corresponding channel of the readout electronics through a flat cable. A common bias voltage was applied to the 16 photodetector elements in the MPPC array. A plastic holder ensured the correct positioning of the crystal on the MPPC array and the PCB. In this board, the signal from each MPPC element was split and part of the signals from all MPPC elements were summed and driven to a common analog output. This output was employed in some of the timing resolution measurements.

3.2.2 $LaBr_3$ crystal

The continuous $LaBr_3$ crystal employed was manufactured by Saint-Gobain Crystals (BrilLanCe 380) and it had an effective volume of 16 mm $\times$ 18 mm $\times$ 5 mm (figure 3.2), matching perfectly the size of the MPPC array. The crystal was surrounded by highly reflective material in five faces, and encapsulated in an aluminium housing due to its hygroscopicity. The open face in contact with the MPPC array was covered by a 1 mm thick optical guide. Usually, optical grease is employed to couple the scintillator crystal to the photodetector. Nevertheless, tests performed in such a way showed an increase in the current flowing through the MPPC array, probably due to the fact that the MPPC elements were not covered by a common coating. For this reason, no optical grease was employed to couple the crystal to the MPPC.

For the detector uniformity tests, a pixelated crystal array was coupled one-to-one to the MPPC array. The crystal array was composed of 16 LYSO crystals of 3 mm $\times$ 3 mm $\times$ 15 mm size, separated with white epoxy resin.

3.3 Readout electronics

The readout electronics employed was based on the SPIROC1 (SiPM Integrated Read-Out Chip) ASIC [35] developed at the Linear Accelerator Laboratory (LAL, Orsay). This ASIC was designed for the readout of SiPMs with positive output polarity, making it suitable to work with the output polarity of the MPPC array described in section 3.2.1.

The SPIROC1 ASIC was a 36-channel, low noise, high dynamic range front-end circuit developed to read out SiPM outputs. Each channel had a preamplifier with an 8-bit input DAC to fine-tune the input voltage of the SiPM bias of each channel individually up to 5 V in 20 mV steps. The high dynamic range (up to 2000 photoelectrons) was achieved by means of two variable gain input preamplifiers. Each preamplifier was followed by a slow shaper with variable shaping time (50-100 ns). In parallel, trigger signals were obtained via a fast shaper (15 ns) followed by a level discriminator. A common threshold was applied to all discriminators that could be adjusted by means of a 4-bit DAC. The trigger signal generated by the SPIROC1 ASIC was given by the logic *OR* of the 36 trigger outputs of the ASIC channels. The diagram of one channel of the SPIROC1 ASIC can be seen in figure 3.3.

For each event recorded, the pulse amplitude was stored using a 12-bit ADC located on the test board. The ASIC was connected to a test board driven by an Altera Cyclone FPGA that controlled the ASIC operation and the communication with the computer through a USB connection. A picture of the evaluation board can be seen in figure 3.4. A dedicated LabView program was employed for the ASIC test and data acquisition.

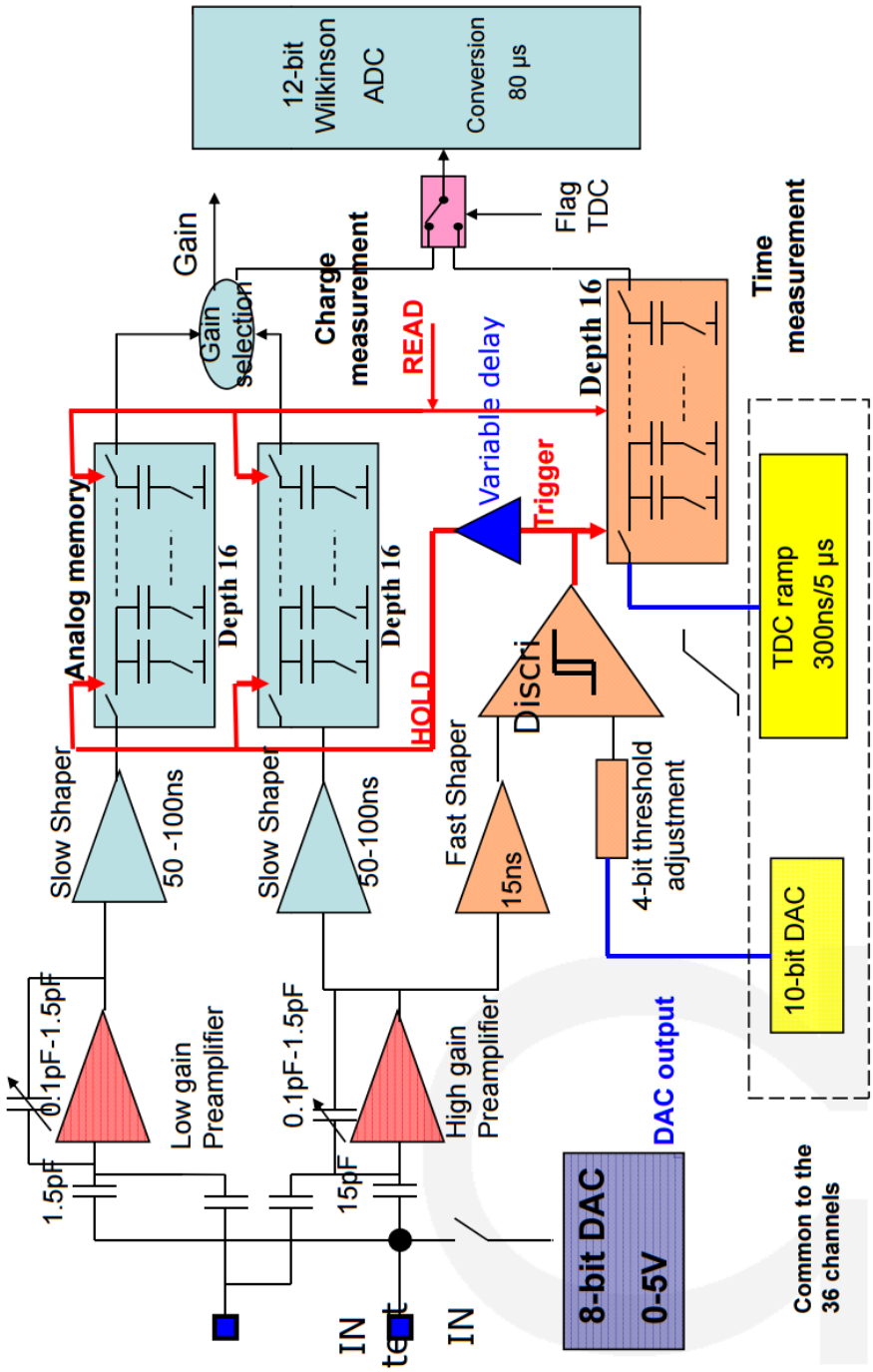

Figure 3.3: SPIROC1 single channel diagram.

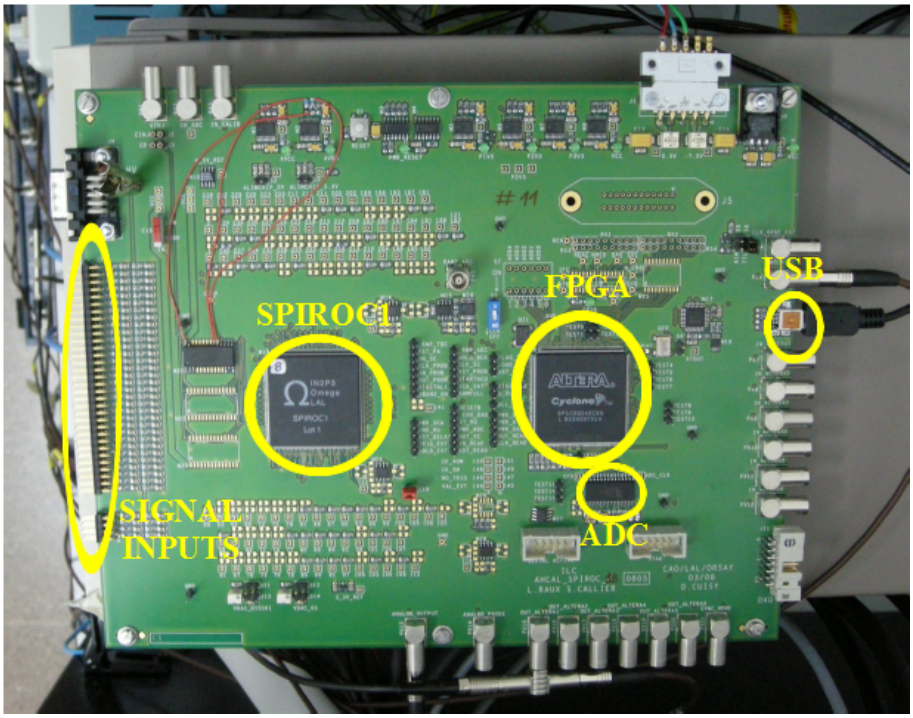

Figure 3.4: SPIROC1 ASIC evaluation board.

3.4 Detector characterization

Characterization tests were carried out to determine the performance of the detector. Results were published in [36] and [31].

3.4.1 Uniformity

The manufacturing process of the MPPC array produced photodetector elements with different operating voltages, which could result in variations in the response of the photodetector elements and therefore produce a degradation of the detector performance as a whole. The operation voltages recommended by the manufacturer ranged from 71.08 V to 71.12 V. The common bias applied to all elements was the average of the operating voltages of the 16 elements, 71.10 V.

The differences in the response of the photodetector elements were tested by coupling the pixelated LYSO crystal array described in section 3.2.2 to the MPPC matrix. Data were taken with a ^{22}Na source placed at a distance far enough from the detector to ensure a homogeneous distribution of the emitted gamma rays among the photodetector elements. This method assumed that, for a high number of events, the average charge per channel would be similar if the response of all channels was the same. An energy spectrum was obtained for each detector channel and the 511 keV photopeak was fitted with a Gaussian function.

The input DACs in the ASIC were employed to adjust the bias voltage applied to each channel and therefore compensate for the differences among the detector elements and achieve a similar response in all of its channels. A small increment or decrement of the bias voltage was applied to each channnel by means of the input DAC. Then, data were taken with the ^{22}Na source again. Figure 3.5 shows the difference in the photopeak position in ADC units for each channel before (dashed histogram) and after (solid histogram) applying the DAC corrections to the individual input voltage, achieving an 8% of improvement.

The effect of these corrections in the energy spectra was also assessed. Figure 3.6 shows the ^{22}Na energy spectrum obtained from all channels without applying the input DAC voltage corrections (dashed histogram) and applying them (solid histogram). It can be clearly seen that the corrected spectrum is significantly narrower than the non-corrected one.

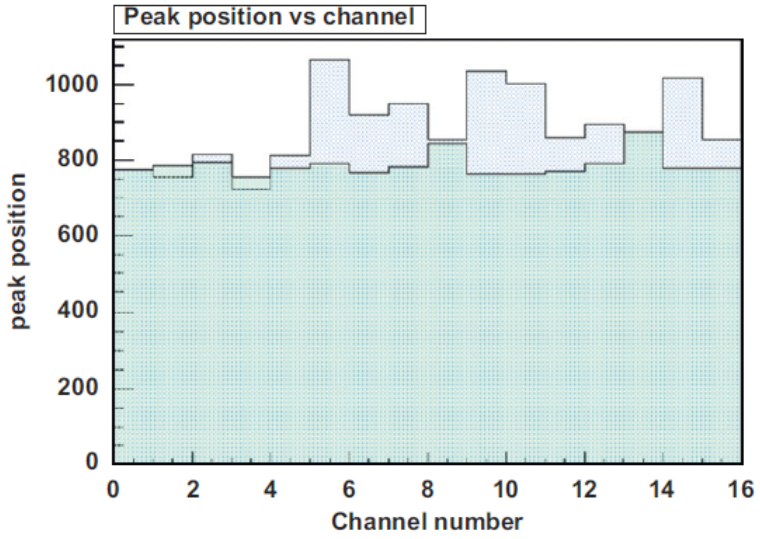

Figure 3.5: Position of the ^{22}Na 511 keV photopeak in ADC units for each channel before (dashed histogram) and after (solid histogram) applying the DAC corrections to the individual input voltage.

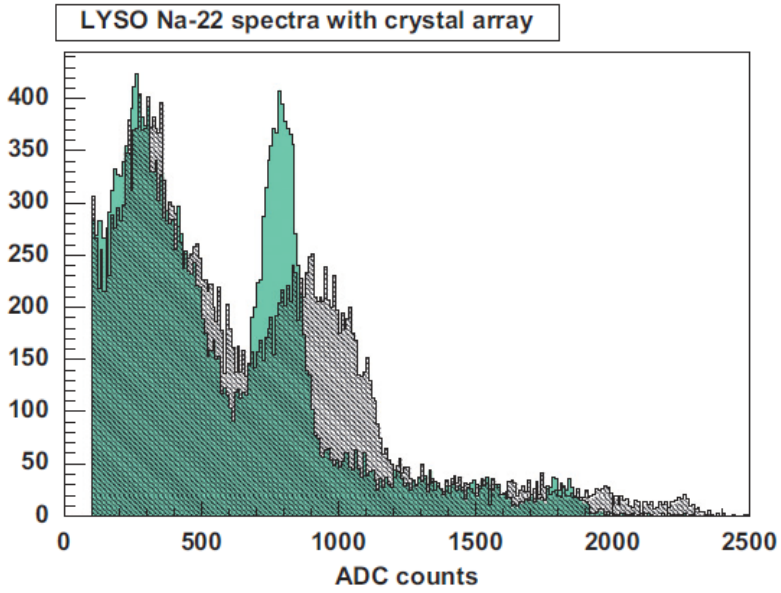

Figure 3.6: ^{22}Na energy spectrum obtained from all channels without applying the input DAC voltage corrections (dashed histogram) and applying them (solid histogram).

Table 3.1: Sources employed for the detector calibration.

Isotope	Energy (keV)
^{57}Co	122
^{22}Na	511
^{137}Cs	662
^{54}Mn	835
^{22}Na	1275

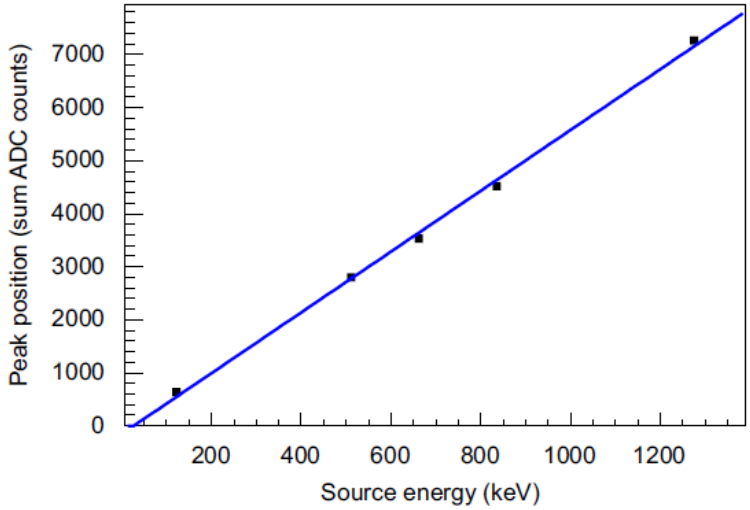

Figure 3.7: Photopeak position in ADC units as a function of the source energy. The behaviour is linear up to 1275 keV.

3.4.2 Linearity

Spectra with different radioactive sources were acquired with the $LaBr_3$ crystal in order to test the linearity of the detector in the range of 122 keV up to 1275 keV. A list of the radioactive sources employed with their corresponding energy can be found in table 3.1.

For each event, the signals acquired in all the photodetector elements were added to calculate the total energy deposited in the crystal. The photopeak position was fitted with a Gaussian function and its position in ADC units was plotted as a function of the source energy. The detector shows a linear behaviour up to 1275 keV, as it can be seen in figure 3.7.

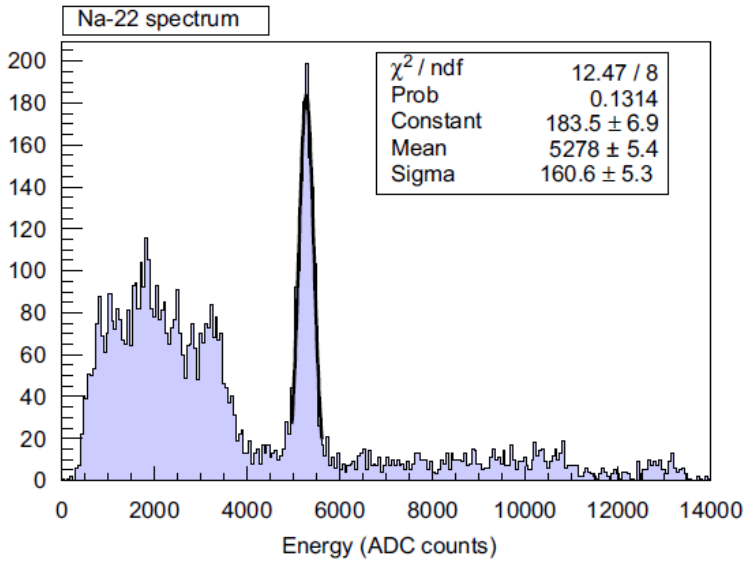

Figure 3.8: ^{22}Na energy spectrum. The energy resolution obtained was 7% FWHM at 511 keV.

3.4.3 Energy resolution

The energy resolution of the $LaBr_3$ scintillator crystal was first measured with a PMT in order to compare it to the value given by the manufacturer. The PMT model employed was a Hamamatsu R6236 read out by an Atomki MCA8k-01 Multichannel Analyzer (MCA). The energy resolution obtained was 5.8% FWHM at 511 keV. The value given by the manufacturer was around 4% FWHM.

The energy resolution obtained with the $LaBr_3$ crystal coupled to the SiPM array and read out by the SPIROC ASIC, without applying any input DACs corrections, was 7% FWHM at 511 keV (figure 3.8). Applying input DACs corrections, the energy resolution obtained was 6.5% FWHM at 511 keV.

The energy resolution results could be limited due to the fact that the MPPC model employed in the measurements had a 50% loss of active area because of the gaps between SiPM elements, meaning that, in an interaction, half of the photons reaching the sensor were lost.

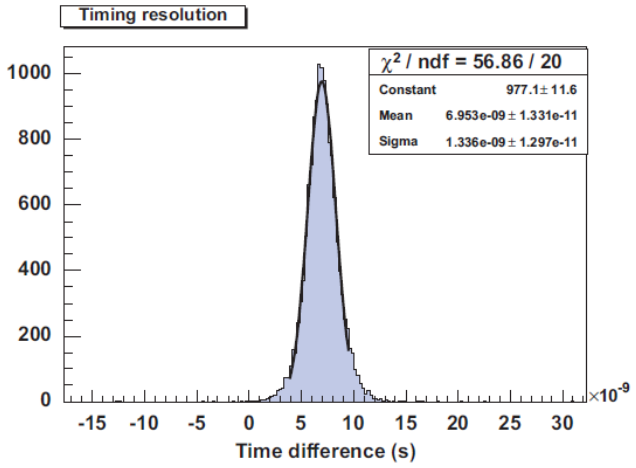

Figure 3.9: Time difference distribution triggering on the sum signal of all channels. The timing resolution obtained was 3.1 ns FWHM.

3.4.4 Timing resolution

The timing resolution of the $LaBr_3$ crystal coupled to the MPPC array and read out by the SPIROC1 ASIC was measured in coincidence with a 1 mm $\times$ 1 mm $\times$ 10 mm LYSO crystal wrapped in Teflon and coupled to a 1 mm $\times$ 1 mm MPPC from Hamamatsu. A ^{22}Na source was employed for this measurement. The trigger signal provided by the SPIROC1 ASIC was connected to one channel of a LeCroy WavePro 940 oscilloscope. The output signal of the 1 mm $\times$ 1 mm MPPC was connected to another channel of the oscilloscope. The time difference between these two signals was histogrammed and the distribution was fitted with a Gaussian function.

A timing resolution of 7.2 ns FWHM was obtained with this method [36]. As mentioned in section 3.3, the trigger signal generated by the SPIROC1 ASIC was given by the logic OR of the 16 channels connected, with a common threshold value set for all channels. This approach was appropriate for pixelated crystals, in which each crystal behaved as an independent detector. But this approach was not optimized for timing measurements with continuous crystals.

With the aim of improving the timing measurement with continuous crystals, an alternative method was tested employing the sum output of the detector PCB, described in section 3.2.1, as the detector trigger signal. With this method, the result obtained was 3.1 ns FWHM, as it can be seen in figure 3.9. This result supported the idea that triggering on the sum signal of all channels could be more appropriate for continuous crystals rather than an OR trigger.

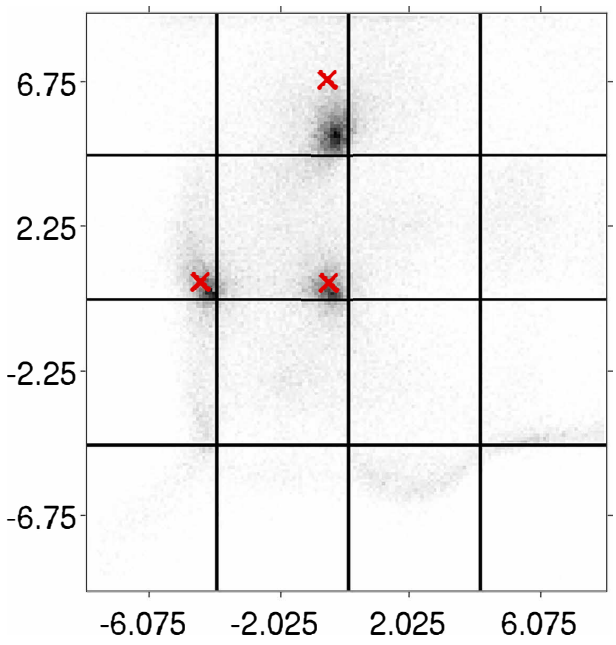

Figure 3.10: Recovered planar interaction location for a ^{22}Na point-like source placed in three different positions. Red crosses represent the real position of the source.

3.4.5 Position determination

The position determination capabilities of this detector were tested employing the position estimation method explained in section 2.3. A ^{22}Na point-like source of 0.25 mm diameter was placed at different positions of the detector surface and operated in time coincidence with a second detector (electronic collimation). The second detector consisted of a 1 mm $\times$ 1 mm $\times$ 10 mm LYSO crystal coupled to a single SiPM of the same area. The source was placed 5 mm away from the continuous crystal and at 30 mm distance from the second detector.

In figure 3.10, the recovered planar interaction location for the ^{22}Na source placed in three different positions is shown. The red crosses represent the real position of the source. A spatial resolution of 0.7 mm FWHM was achieved in the whole surface of the crystal selecting only the events that interacted close to the photodetector surface [37].

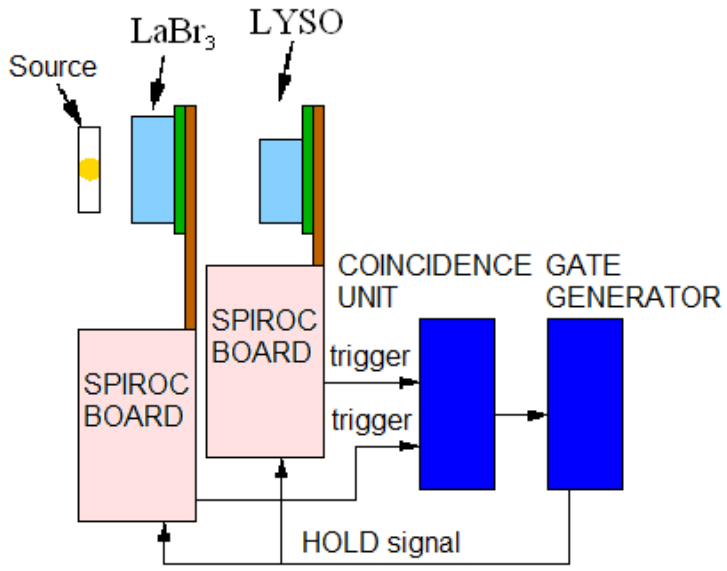

Figure 3.11: Schematic representation of the experimental coincidence setup.

3.5 Coincidence tests

3.5.1 Experimental setup

In order to determine the detector performance in time coincidence, tests were carried out using the previously described detector as a first layer of the telescope. A second layer was added, consisting of a 12 mm $\times$ 12 mm $\times$ 5 mm LYSO crystal, painted white in five faces and coupled to another 16 mm $\times$ 18 mm S11064-050P MPPC array from Hamamatsu. The crystal was placed in one corner of the MPPC array, covering 9 out of the 16 pixels. Each detector was attached to a PCB that provided a common bias to the detector elements and routed the signal coming from each pixel to the corresponding channel of the SPIROC1 ASIC. A plastic holder attached to the PCB ensured the correct positioning of the crystal on the MPPC. A schematic representation of the setup can be seen in figure 3.11.

A ^{22}Na source was employed in the coincidence tests. Photons underwent Compton scattering in the first detector and interacted in the second detector through a second Compton interaction or suffering photoelectric absorption. Each detector was connected to a SPIROC1 board that generated an individual trigger signal. The triggers generated in the two boards were led to a NIM coincidence unit to determine when a photon interacted in both detectors. A hold signal was then generated and sent back to

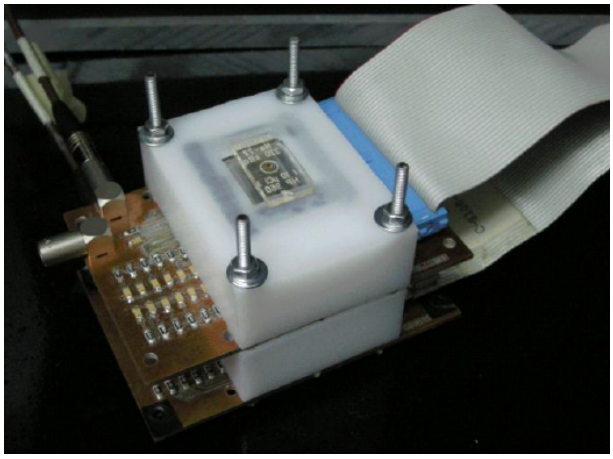

Figure 3.12: Picture of the experimental setup with the source located on the first detector.

the ADCs in each board to digitize the data. A dedicated LabView program capable of handling two SPIROC1 boards was employed as data acquisition software. A picture of the experimental setup is shown in figure 3.12.

3.5.2 Energy spectra

Energy spectra were taken from the two detectors in two different ways: from each detector independently (without coincidence) for energy calibration purposes, and from both detectors working in time coincidence. A ^{22}Na (511 keV and 1275 keV) source with 8 kBq activity was employed.

The energy spectra obtained with the two detectors can be seen in figure 3.13. As a reference, the spectra acquired without coincidence are shown in figure 3.13 (a) for the $LaBr_3$ and in (b) for the LYSO. The energy resolution obtained for the $LaBr_3$ crystal alone was 8.3% FWHM at 511 keV biased at the operating voltage indicated by the manufacturer. For the LYSO crystal alone, an energy resolution of 18.3% FWHM at 511 keV was obtained in this test.

Figure 3.13 (c) and (d) show the spectra acquired when both detectors were operated in time coincidence. In the first detector (figure 3.13 (c)), only the low energy region of the Compton continuum was recorded because only forward scattered photons could be detected due to the geometrical distribution of the detectors. A small peak in the Compton region can be seen in figure 3.13 (c) around 280 keV. This peak was due to the photons that interacted first in the second detector and backscattered to the first detector. In the second detector (figure 3.13 (d)), higher energy events were

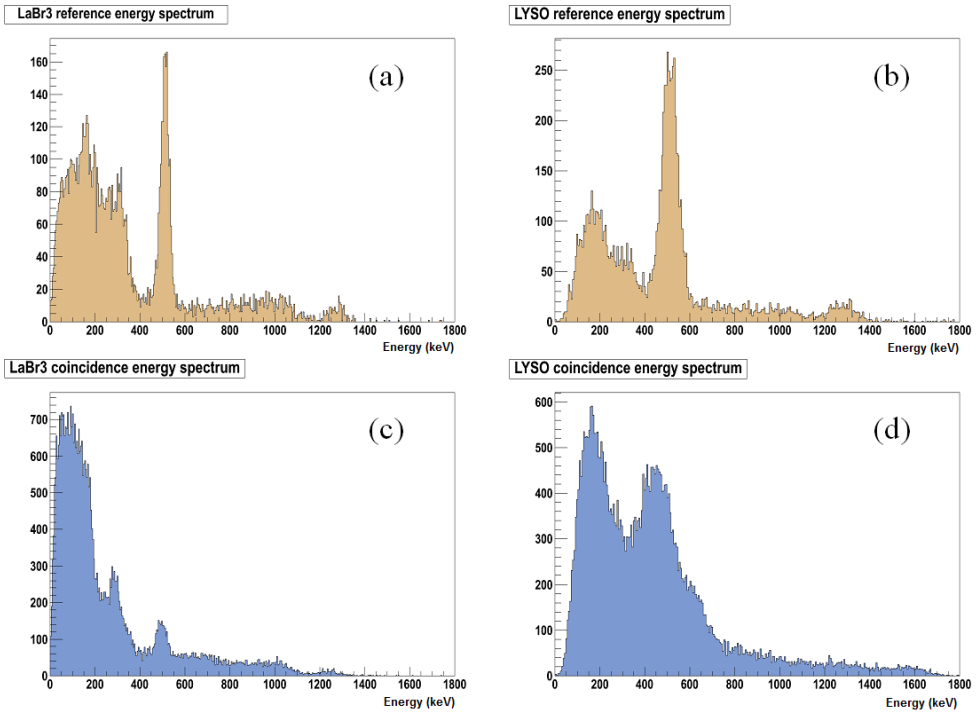

Figure 3.13: Reference energy spectra of $LaBr_3$ (a) and LYSO (b). Coincidence energy spectra of $LaBr_3$ (c) and LYSO (d).

recorded because in most events the photon was fully absorbed. In both detectors, the photopeaks should disappear when working in time coincidence mode, but peaks can be seen in figure 3.13 (c) and (d) at 511 keV. Further studies showed that these peaks were mostly due to coincidence events between a 511 keV and a 1275 keV gamma.

Figure 3.14 shows the sum of the energies recorded in both detectors when operated in time coincidence (figure 3.13 (c) and (d)). The photopeak appeared again, as a result of summing the energies of the photons scattered in the first detector and fully absorbed in the second detector. Events at energies lower than the photopeak corresponded to the events that Compton scatter in both detectors. The events corresponding to 1275 keV gamma rays that escaped the second detector can be seen at energies higher than 511 keV.

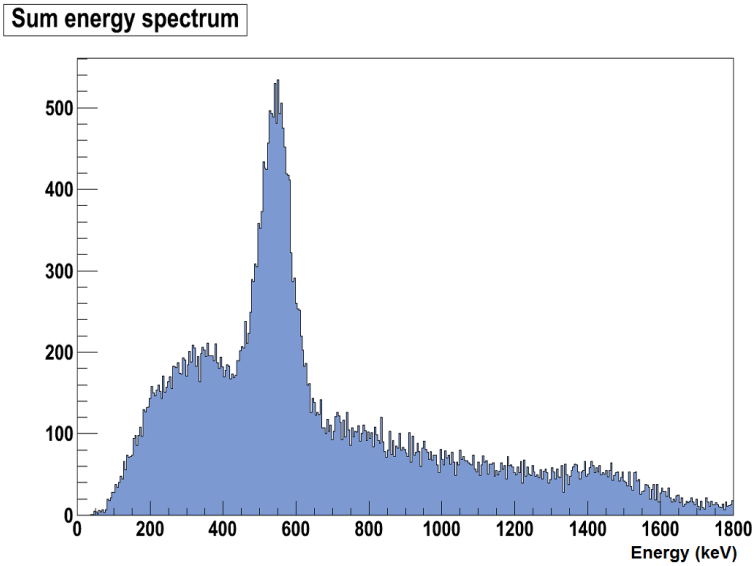

Figure 3.14: Sum energy spectrum of both detectors.

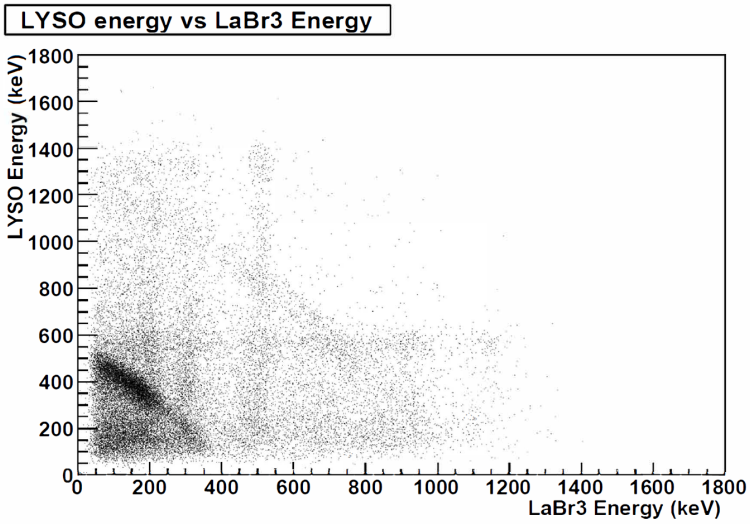

Figure 3.15: Energy recorded in the second detector (LYSO) versus the energy recorded in the first detector ($LaBr_3$) in the data taken with the ^{22}Na source.

Figure 3.15 shows the energy recorded in the second detector (LYSO) versus the energy recorded in the first detector ($LaBr_3$) in the data taken with the ^{22}Na source. The diagonal lines corresponded to the photons scattered in the first detector, and absorbed in the second detector, with 511 keV or 1275 keV total energy. The horizontal and vertical lines corresponded to random coincidences with full absorption in one layer.

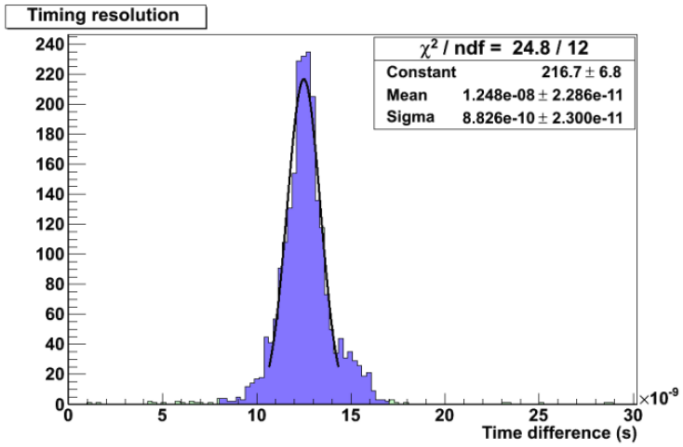

Figure 3.16: Coincidence timing resolution distribution obtained of 2 ns FWHM.

3.5.3 Coincidence timing resolution

The coincidence timing resolution of the two detector layers also was measured. The trigger signal provided by the SPIROC1 ASIC of the first layer was connected to one channel of an oscilloscope. The trigger signal provided by the SPIROC1 ASIC of the second layer was connected to another channel of an oscilloscope. The coincidence signal provided by the coincidence unit was used as an external trigger in order to record only coincidence events. The time difference between the trigger signals from the two detectors provided by the SPIROC1 boards was histogrammed and the distribution was fitted with a Gaussian function. A timing resolution of 10 ns FWHM was obtained with this method.

The coincidence timing resolution was also measured employing the sum output in the PCBs of both detectors, as described in section 3.2.1. With this method, the result obtained was 2 ns FWHM, as it can be seen in figure 3.16. Again, this results indicates that triggering on the sum signal of all channels is important for continuous crystals.

3.6 Work beyond this thesis

The tests described in this chapter were part of the first proof of concept of a Compton telescope. Images of point-like sources were obtained with this prototype and published in [38]. The results obtained demonstrated the feasibility of operating the system and led to a second version of the prototype consisting of a three-layer telescope with detectors four times bigger [39]. The increase in the number of channels made it necessary to move from the SPIROC1 ASIC and its 36 channels to another ASIC. The electronics employed in the second version of the prototype was based on the VATA64HDR16 ASIC, fully described in chapter 5. The performance of this second prototype of the Compton telescope was tested in-beam and the results were published in [40].

The author of this thesis is currently working on the third generation of the Compton telescope. The MPPC arrays employed as photodetectors are going to be updated to the last available model from Hamamatsu (S13361-3050AE-08), improving several specifications. Besides, the suitability of $CeBr_3$ (Cerium (III) Bromide) for this application is being investigated.

Chapter 4

First prototype of a small animal PET based on SiPMs and continuous LYSO crystals

4.1 Introduction

In a PET scanner, the two main parameters to maximize are sensitivity and spatial resolution. Traditionally, commercial PET scanners employ detector blocks consisting of segmented scintillation crystals coupled to an array of PMTs. The position of the interaction is determined by identifying the crystal in which the interaction took place. The pixelated crystals are surrounded by reflective material to separate them and channel the scintillation light generated in an interaction. Thus, the spatial resolution depends on the crystal size and the photodetector ability to separate the crystals in the block. Reducing the crystal size improves the spatial resolution, but it increases the amount of dead space due to segmentation and therefore it reduces the sensitivity. Reducing the crystal size also increases the complexity of the readout electronics and the detector cost.

The use of continuous crystals can improve both sensitivity and spatial resolution simultaneously [41, 42, 43, 44, 45, 46, 47, 48, 49, 50, 51, 52]. The lack of segmentation increases the active volume and therefore sensitivity. Spatial resolution is not longer limited by crystal size and the position of the interaction is now determined by the scintillation light distribution over the photosensor array. Moreover, monolithic crystals are significantly lower in cost than pixelated crystals, since no segmentation is needed.

PMTs are the most used photosensors in commercial PET scanners. Their main properties are a high sensitivity for extremely low light intensities and a fast response, at the expense of being bulky photodetectors. Besides, PMTs cannot be operated in the presence of a magnetic field, preventing the development of multimodality PET-MR systems. In the last years, SiPMs have emerged as a candidate to substitute PMTs in PET applications [53, 54, 55, 56, 57, 58, 59, 60], offering high gain, fast timing properties, compactness and insensitivity to magnetic fields.

The first part of this chapter describes the characterization of a PET detector head based on continuous LYSO crystals and SiPM arrays as photodetectors for its use in the development of a first prototype of a small animal PET scanner. In the second part of this chapter, two detector heads were mounted and operated in time coincidence, obtaining tomographic images. In the last part of this chapter, test of novel geometries were carried out employing GEANT4 simulations.

4.2 Detector description

The detector heads employed in the first prototype of a small animal PET consisted of a continuous LYSO crystal coupled to a 64-pixel SiPM matrix. Three LYSO crystals with different types of painting (white, black and black and white) were tested, and a pixelated crystal array was employed to evaluate the matrix uniformity.

4.2.1 SiPM matrices

The Center for Scientific and Technological Research (FBK-irst) developed the monolithic SiPM matrices employed in the first prototype of a small animal PET. Monolithic matrices have the advantage that the signal is routed from each pixel to the side of the detector by means of readout lines, instead of wire-bonds that require more space, thus minimizing the dead area between the pixels. They consisted of 64 SiPM elements distributed in an array of 8 $\times$ 8 pixels in a common substrate. The matrices had readout pads on two sides, with 32 channels on each side. Each channel had an active area of 1.5 mm $\times$ 1.4 mm and had 840 microcells of 50 μm $\times$ 50 μm size with a fill factor of about 35%. The microcells had a n-on-p structure optimized to enhance the photon detection efficiency (PDE) at 420 nm. The pitch was 1.5 mm in both directions. There was no gap between the 8 pixels in each row, but below each row there was a dead space of 0.1 mm for the readout lines to reach the sides of the detector. The

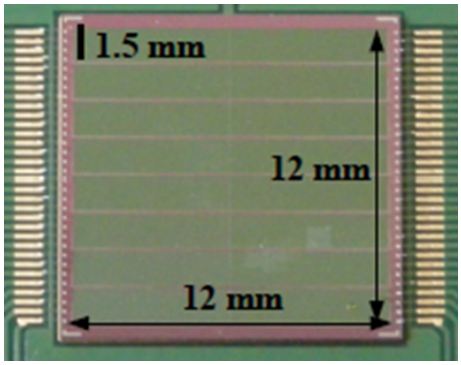

Figure 4.1: SiPM matrix from FBK-irst composed of 64 elements of 1.5 mm $\times$ 1.4 mm and readout in two sides.

active area of the SiPM matrix was 12 $\times$ 12 mm^2. A picture of the matrix can be seen in figure 4.1.

The matrix was glued and wire-bonded to a custom-made printed circuit board (PCB) for bias and mechanical support. Since the matrix was fabricated on a common substrate, the same bias voltage was applied to all channels in the matrix through the backplane. The output polarity of the SiPM elements was negative. The PCB routed the signal coming from each pixel to the corresponding channel of the readout electronics. The breakdown voltage of the SiPM matrix was around 30 V. The measurements performed in the following sections were obtained with the matrix operated at 4.5 V above the breakdown voltage, unless otherwise stated.

4.2.2 LYSO crystals

The continuous LYSO crystals employed were manufactured by Hilger Crystals. Their dimensions were 12 mm $\times$ 12 mm $\times$ 5 mm, matching perfectly the area of the SiPM matrix. The effect of the color of the painting on the surface of the crystal was investigated. To do so, three different LYSO crystals with three different types of painting were evaluated. All of them were painted in five faces, leaving one 12 mm $\times$ 12 mm without painting to couple to the photodetector. The so-called *white slab* was painted in white in five faces. The *black slab* was painted in black in five faces. The *black and white slab* was painted in white on the face opposite to the SiPM matrix and in black on the sides.

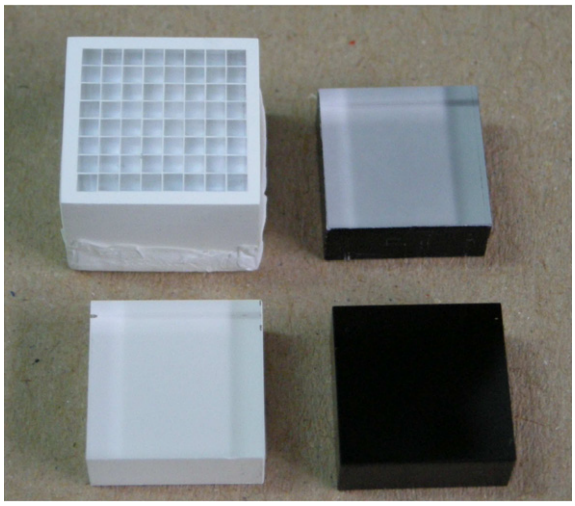

Figure 4.2: Crystals employed in the tests. Top left: crystal array. Top right: black and white slab. Bottom left: white slab. Bottom right: black slab.

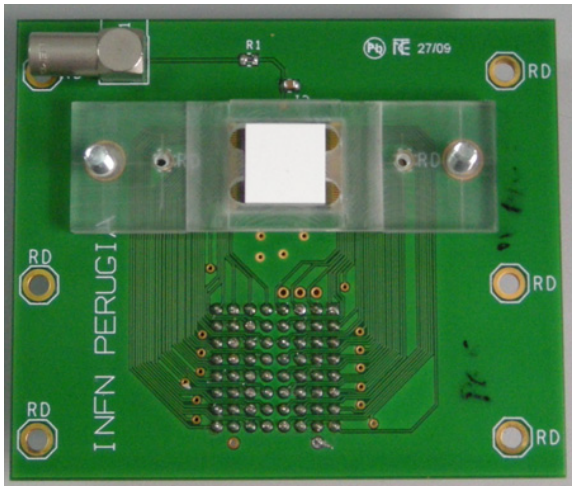

Figure 4.3: Detector head consisting of a 12 mm $\times$ 12 mm $\times$ 5 mm LYSO crystal painted in white coupled to a SiPM matrix. A PCB provides electrical connections and mechanical support. A plastic holder ensures the correct positioning of the crystal.

For the detector uniformity tests, a pixelated crystal array was coupled one-to-one to the SiPM matrix. The crystal array was composed of 64 LYSO crystals of 1.4 mm $\times$ 1.4 mm $\times$ 10 mm size, separated with 100 μm of white epoxy resin. A picture of the crystals employed in the tests can be seen in figure 4.2.

A plastic holder ensured the correct positioning of the crystal on the SiPM matrix and the PCB. A picture of the whole detector head can be seen in figure 4.3.

4.3 Readout electronics

The readout electronics employed was the MAROC2 (Multi Anode Read-Out Chip) ASIC [61] developed at the Linear Accelerator Laboratory (LAL, Orsay). This ASIC was originally designed for the readout of multi-anode PMTs (Hamamatsu H7546) employed in the Roman Pots of the ATLAS luminometer, at CERN. Those multi-anode PMTs had negative output polarity, as well as the SiPM matrices employed in the prototype and described in section 4.2.1. Nevertheless, the ASIC was not optimized for the readout of SiPMs nor for PET applications, and its performance could be improved in some aspects.

The MAROC2 ASIC had 64 channels. Each channel had a preamplifier with a 6-bit adjustable gain stage. A slow shaper with variable shaping time provided the shaped signal, the amplitude of which was proportional to the input charge. The preamplifier was followed by a slow shaper with variable shaping time. The shaping time was set to the longest possible (about 120 ns) to integrate the LYSO signals. In parallel, trigger signals were obtained via a fast shaper (15 ns) followed by a level discriminator. A common threshold was applied to all discriminators that could be adjusted by means of a 12-bit DAC. The trigger signal generated by the MAROC2 ASIC was given by the logic *OR* of the 64 trigger outputs of the ASIC channels. The trigger was employed to generate a *HOLD* signal in an external NIM gate generator, which was sent back to the board to sample the shaped signal at its maximum. The diagram of one channel of the MAROC2 ASIC can be seen in figure 4.4

For each event recorded, the signals coming from the 64 slow shapers were digitized using a 12-bit ADC located on the test board and multiplexed in a single analog charge output. The ASIC was connected to a test board with a FPGA Altera Cyclone that controlled the ASIC operation and the communication with the computer through USB protocol. A picture of the evaluation board can be seen in figure 4.5. A dedicated LabView program was employed for the ASIC test and data acquisition.

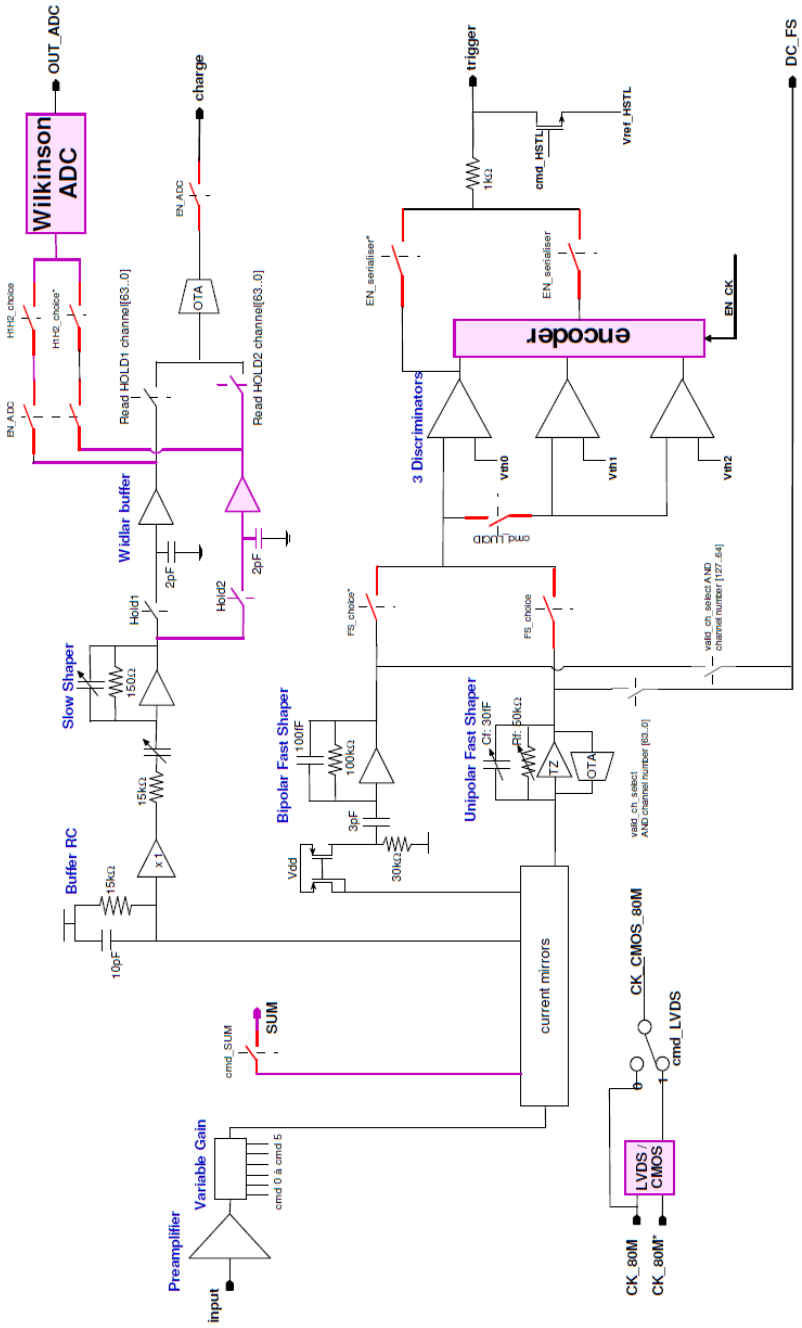

Figure 4.4: MAROC2 single channel diagram.

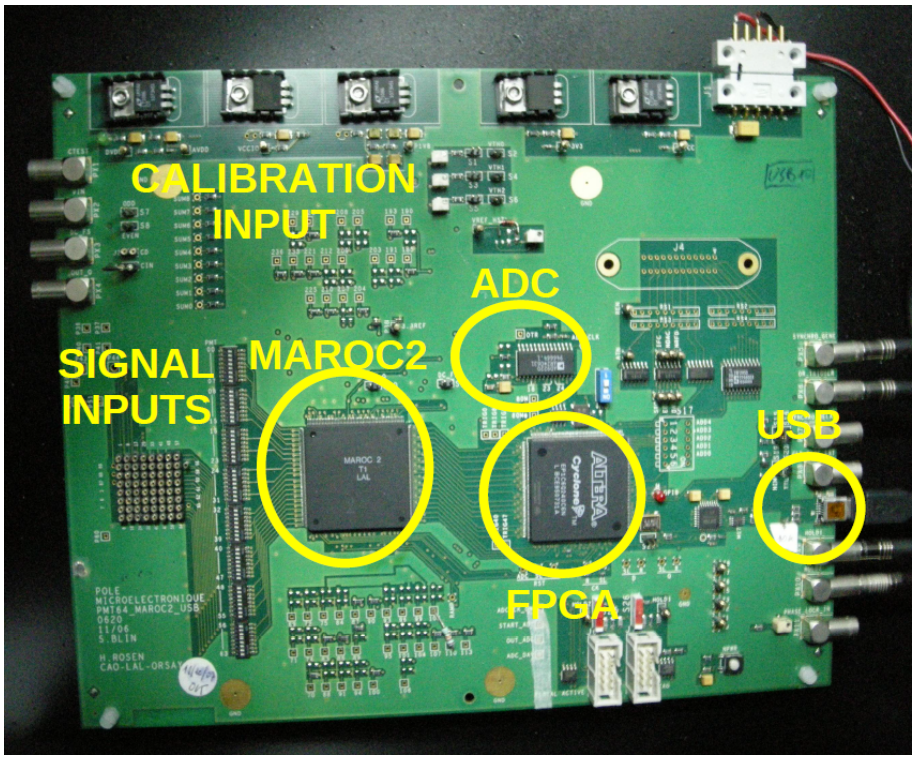

Figure 4.5: MAROC2 ASIC evaluation board.

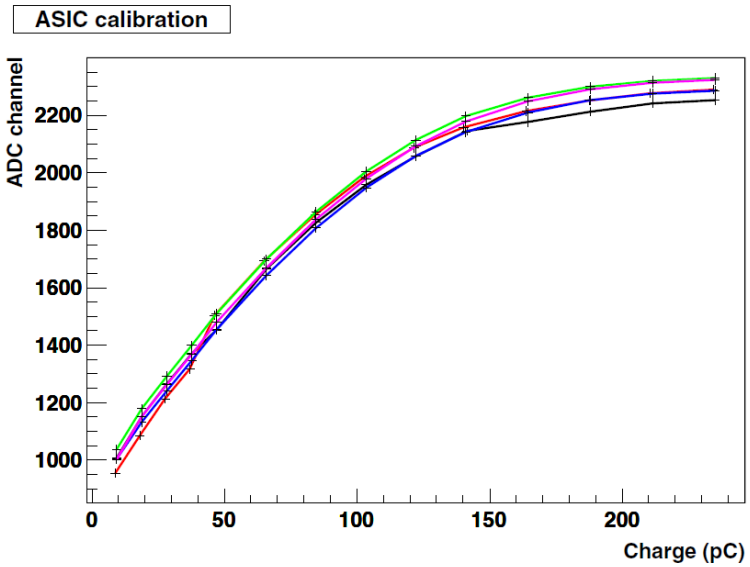

Figure 4.6: MAROC2 ASIC relationship between input charge and ADC units for five different channels.

4.4 Detector characterization

Characterization tests were carried out to determine the performance of the detector. Results were published in [48].

4.4.1 Input charge range

In order to establish a correlation between input charge and ADC units, a voltage pulse was sent through a 47 nF capacitor to one channel of the ASIC. Figure 4.6 shows the ASIC response to an injected calibration pulse as a function of the injected charge for five channels. The ASIC had a linear response from 10 pC up to 80 pC, with a uniformity in the channel response of about 1%, and then it started to deviate from linearity until it reached complete saturation. The typical signals coming from the SiPM matrix were in the linear region.

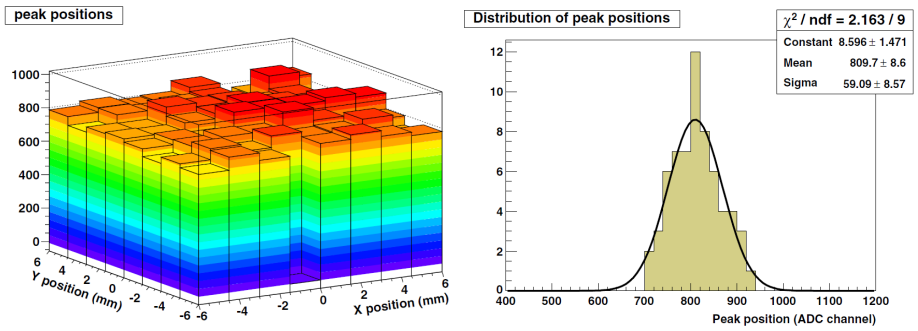

(a) (b)

Figure 4.7: (a) 2D plot of the ^{22}Na photopeak position for all pixels in the matrix. (b) Distribution of the mean values of the fitted photopeak positions. The standard deviation was 7.3%.

4.4.2 Uniformity

The uniformity of the 64 channels was evaluated coupling the pixelated LYSO crystal array described in section 4.2.2 one-to-one to the pixels in the SiPM matrix. The amount of light per channel in pixelated crystals is larger than in continuous crystals. Thus, in order to have signals in the individual pixels in a range comparable to the ones obtained with continuous crystals, a 2 V overvoltage was employed in this measurement. Data were taken with a ^{22}Na source placed at a distance far enough from the detector to ensure an homogeneous distribution of the emitted gamma rays among the photodetector elements. An energy spectrum was obtained for each detector channel and the 511 keV photopeak was fitted with a Gaussian function in each case.

Figure 4.7 (a) shows the mean value of the photopeak position in ADC units for each channel, as a function of the pixel location. The channel with no signal corresponded to a dead channel in the ASIC, and it was excluded from the calculations of the uniformity. Figure 4.7 (b) shows the distribution of the peak positions of the 64 channels, fitted with a Gaussian function. The distribution of the peak positions, which included variations of the electronics and crystals, had a standard deviation of 7.3%. No corrections were applied to the individual photodetector elements.

Table 4.1: Sources employed for the detector calibration.

Isotope	Energy (keV)
^{57}Co	122
^{133}Ba	356
^{22}Na	511
^{137}Cs	662
^{54}Mn	835
^{22}Na	1275

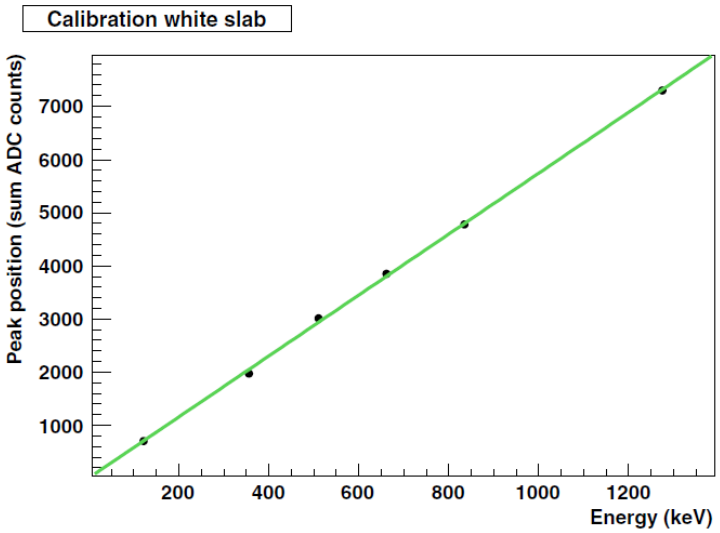

Figure 4.8: Photopeak position in ADC units as a function of the source energy. The behaviour was linear up to 1275 keV.

4.4.3 Linearity

Among the crystals employed in the tests, the white slab was the one that gave the highest amount of light per pixel, therefore having a higher probability of saturating the photodetector. For this reason, spectra with different radioactive sources were acquired with the white slab to test the linearity of the detector in the range of 122 keV up to 1275 keV. A list of the radioactive sources employed with their corresponding energy can be found in table 4.1. For each event, the signals acquired in all the photodetector elements were added to calculate the total energy deposited in the crystal. The photopeak position was fitted with a Gaussian function and its position in ADC units was plotted as a function of the source energy. The detector shows a linear behavior up to 1275 keV, as it can be seen in figure 4.8.

Table 4.2: Energy resolution measured for the three crystals.

Crystal	Energy resolution (FWHM)
White	15%
Black	26%
Black and white	30%

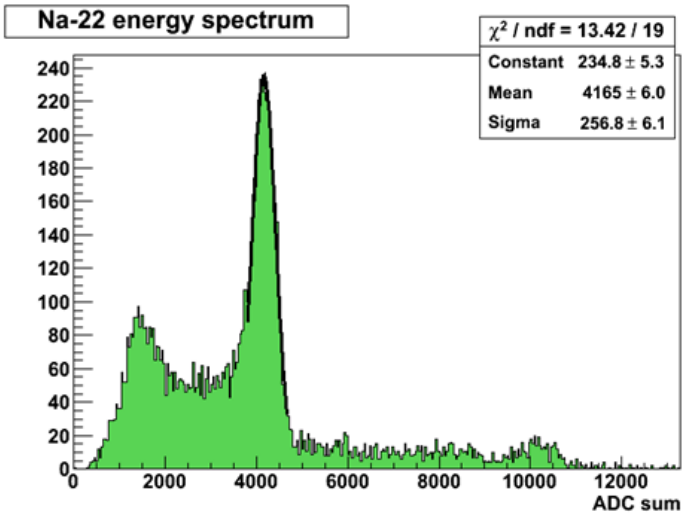

Figure 4.9: ^{22}Na energy spectrum for the white slab. The energy resolution obtained was 15% FWHM at 511 keV.

4.4.4 Energy resolution

The energy resolution of the three LYSO crystals coupled to the same SiPM matrix and read out by the MAROC2 ASIC was evaluated employing a ^{22}Na source. The 511 keV photopeak was fitted with a Gaussian function and the energy resolution was calculated for each of the three crystals.

Table 4.2 shows the energy resolution measured for the three crystals. The energy resolution at 511 keV was 15% FWHM for the white slab, 26% FWHM for the black slab and 30% for the white and black slab. Figure 4.9 shows the ^{22}Na spectrum obtained with the white slab. The white crystal offered the best energy resolution because the reflection of the light on the sides and the back of the crystal resulted in a larger amount of light reaching the photodetector.

Table 4.3: Timing resolution measured for the three crystals in coincidence with a BaF_2 crystal coupled to a PMT.

Crystal	Timing resolution (ns FWHM)
White	6.0
Black	6.8
Black and white	8.7

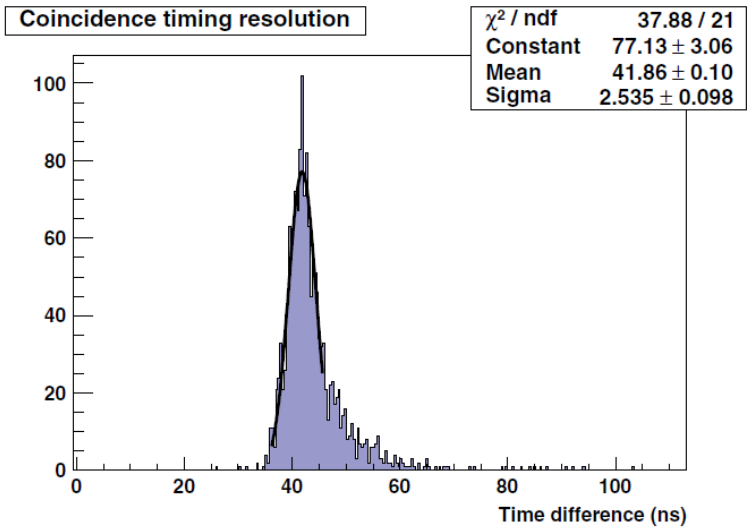

Figure 4.10: Timing distribution for the white slab in coincidence with a BaF_2 crystal coupled to a PMT. The timing resolution obtained was 6.0 ns FWHM.

4.4.5 Timing resolution

The timing resolution of the three LYSO crystals described in section 4.2.2 coupled to the same SiPM matrix and read out by the MAROC2 ASIC was measured in coincidence with a 5.5 mm $\times$ 5.5 mm $\times$ 5 mm BaF_2 crystal coupled to a PMT Hamamatsu H5783. The trigger signal provided by the MAROC2 ASIC was connected to one channel of a LeCroy WavePro 940 oscilloscope. The output signal of the PMT was discriminated and then split in two. One part of the signal was connected to another channel of the oscilloscope for the timing measurement. The other part of the signal was connected to the MAROC2 ASIC as an external trigger in order to perform the coincidences between this external trigger and the internal trigger coming from detected events in the SiPM matrix. The coincidence signal generated by the MAROC2 ASIC was also connected to the oscilloscope and employed as a trigger. The time difference between the trigger signals provided by both detectors was histogrammed

and the distribution was fitted with a Gaussian function.

Table 4.3 shows the timing resolution obtained with the three different crystals. The timing resolution was 6.0 ns FWHM for the white slab, 6.8 ns for the black slab and 8.7 ns for the black and white slab. Figure 4.10 shows the timing distribution obtained with the white slab. The white crystal provided the best timing resolution due to the higher amount of photons reaching the photodetector per event detected. Nevertheless, the use of continuous crystals results in a relatively low amount of light per pixel, which gives poor timing performance. The trigger signal of the detector head was generated by the FPGA as the OR signal of the 64 trigger outputs of the ASIC channels. This approach was not optimized for timing measurements with continuous crystals. Possible improvements would be to employ a signal given by the sum of the signals of all the pixels in the matrix to generate a trigger. Another option would be to implement a double threshold system that allows to trigger at low threshold levels, while selecting only the photopeak events.

4.4.6 Position determination

The main disadvantage of continuous crystals is the difficulty to determine accurately the interaction position of the gamma rays in the crystal, in particular when it takes place close to the crystal edges. Center Of Gravity (COG) and Maximum Likelihood (ML) methods were tested in the early stages of the prototype [48]. The COG method failed to reconstruct the real interaction position close to the edges with the black crystal and in the whole surface for the white crystal, suffering from a compression effect. The ML method was successfully applied and it improved the position determination also in the case of white crystals, providing the correct positioning in the whole surface with the three crystals. The main drawback of this method was that it required a previous calibration of the Light Response Function (LRF) of the whole surface of the detector, and the calibration needed to be repeated each time the detector conditions changed.

To overcome the problems of the above mentioned approaches, the position determination method explained in section 2.3 was employed. In order to test the position determination algorithm, a ^{22}Na point-like source of 0.25 mm diameter was placed at different positions of the detector surface and operated in time coincidence with a second detector (electronic collimation). The second detector consisted of a 1 mm $\times$ 1 mm $\times$ 10 mm LYSO crystal coupled to a single SiPM of the same area. The

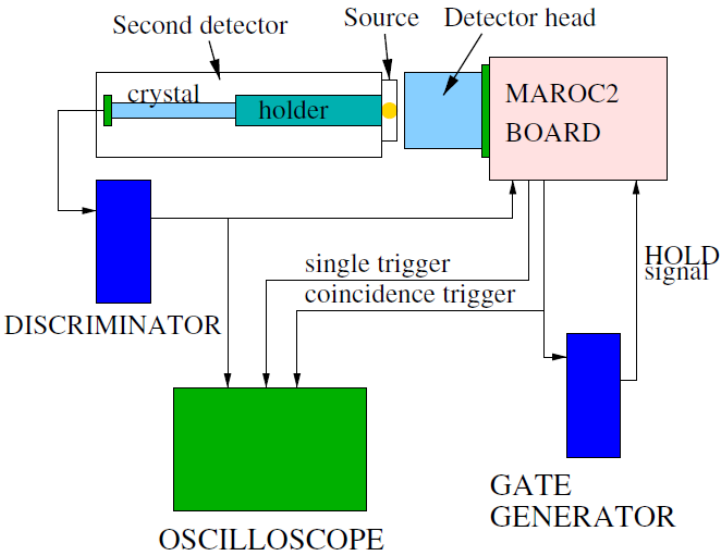

Figure 4.11: Schematic representation of the setup employed for the position determination tests.

source was placed 5 mm away from the continuous crystal and at 30 mm distance from the second detector. A schematic representation of the setup employed can be seen in figure 4.11.

Experimental data were obtained with the 5 mm and 10 mm thick white crystals [62]. For the 5 mm thick crystal, data were taken at four different interaction points. Figure 4.12 shows the distribution of the reconstructed positions at the four different interaction points. The average spatial resolution of the reconstructed positions for the 5 mm thick crystal was 0.69 $\pm$ 0.08 mm FWHM. Figure 4.13 shows a profile in x through the maximum of the distribution for the position A, the closest to the center of the crystal in figure 4.12. The FWHM of the profile was 0.7 mm.

For the 10 mm thick crystal, data were taken at nine different interaction points. Figure 4.14 shows the distribution of the reconstructed positions at the nine different interaction points. The average spatial resolution of the reconstructed positions for the 10 mm thick crystal was 0.73 $\pm$ 0.11 mm FWHM.

Results obtained for the 5 mm and 10 mm thick white crystal are summarized in table 4.4. It must be noted that at that point events interacting far from the photodetector were cut due to a high threshold operation. This resulted in an artificially improved spatial resolution that gets closer to 1 mm FWHM when events in the whole crystal thickness are considered [22].

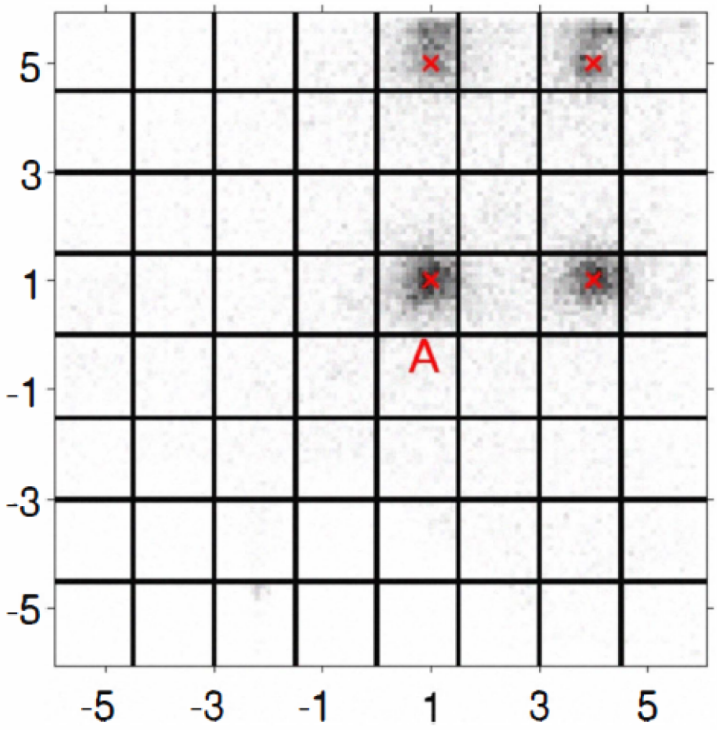

Figure 4.12: Distribution of reconstructed interaction positions at four different interaction points for the 5 mm thick white crystal.

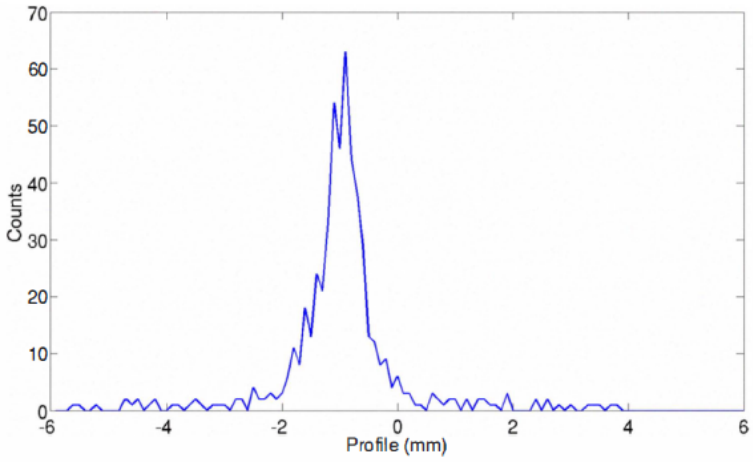

Figure 4.13: Profile through the maximum of the distribution of reconstructed positions for an interaction point close to the center of the crystal. The FWHM is 0.7 mm.

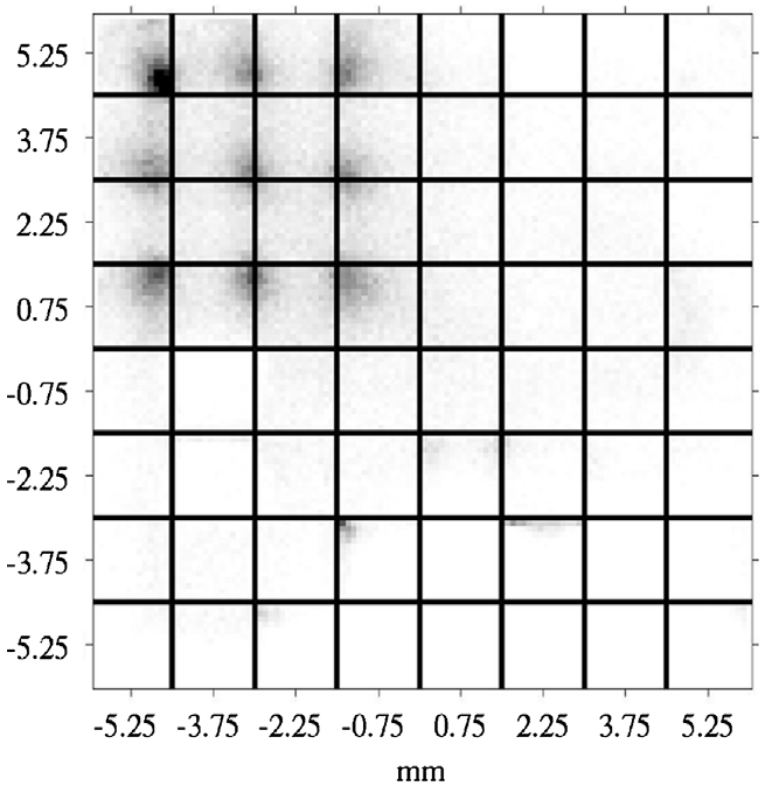

Figure 4.14: Distribution of reconstructed interaction positions at nine different interaction points for the 10 mm thick white crystal.

Table 4.4: Average position reconstruction results for the 5 mm and 10 mm thick white crystal.

	5 mm thick	**10 mm thick**
FWHM (mm)	0.69 ± 0.08	0.73 ± 0.11
FWTM (mm)	1.89 ± 0.22	2.0 ± 0.1

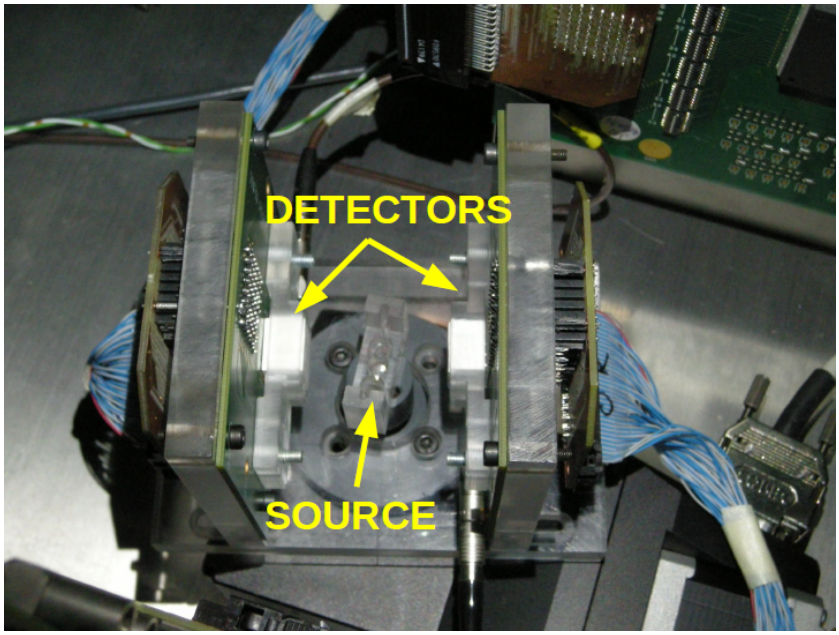

Figure 4.15: Picture of the experimental rotating system employed to take tomographic data at different angles.

4.5 Coincidence tests

4.5.1 Experimental setup

In order to test the imaging capabilities of the detector described in the previous sections, a first prototype of a small animal PET was assembled. The prototype consisted of two detector heads placed in front of each other. Tests were carried out with continuous crystals of size 12 mm $\times$ 12 mm $\times$ 5 mm painted white on five faces. The detector heads were fixed to a methacrylate frame for mechanical support and alignment of the system. The frame was attached to a rotating stage MICOS DT-65N and the sources to be imaged were stationary at the center of the system in a field of view (FOV) of 12 $\times$ 12 $\times$ 12 mm^3. The distance between detectors was 45.8 mm, making it possible to cover six angular positions from 0° to 150° at 30° steps.

Each detector was connected to a MAROC2 board through a ribbon cable. The trigger signals generated by the two boards were led to a NIM coincidence unit CAEN N455. The coincidence signal was sent to a custom made NIM gate generator to produce a HOLD signal that was sent back to the two boards to digitize the recorded event. A dedicated DAQ program developed in LabView controlled the rotation stage and the data acquisition of the two detectors simultaneously, and stored the digitized

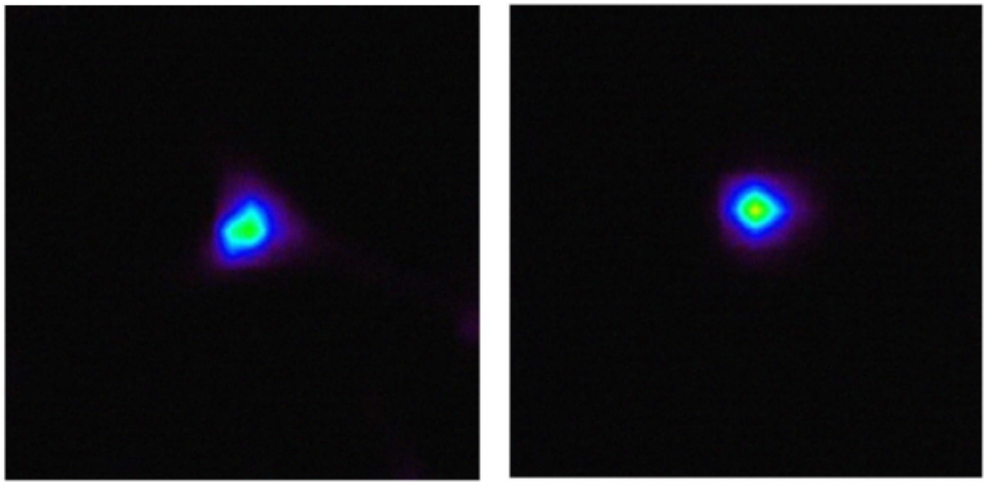

Figure 4.16: Transaxial (left) and sagittal (right) views of a point-like source reconstructed with the MLEM algorithm employing continuous white crystals. The FWHM was 0.9 mm in average.

data from all channels of the two detectors for each coincidence event for further processing. A picture of the experimental rotating system can be seen in figure 4.15.

4.5.2 Image reconstruction

To reconstruct the first tomographic images, a standard Maximum Likelihood Expectation Maximization (MLEM) algorithm was implemented [63]. In order to model the scanner, the volumes of the continuous crystals were divided into virtual subvolumes. Lines of response (LORs) were obtained by taking all the possible pairs of subvolumes between the two detectors. The format used in the reconstruction was LOR-histogram [64]. The system matrix employed in the MLEM algorithm was computed using the Siddon multi-ray tracing technique. The system matrix took into account the main geometrical component (solid angle), as well as finite size of the (virtual) detectors. Positron range and acollinearity were ignored. A Gaussian filter was applied to the image volumes to reduce the noise. The FOV of the reconstructed image volumes was $12 \times 12 \times 12$ mm^3 and the image voxel was 0.5 mm^3.

Figure 4.16 shows a reconstructed ^{22}Na point-like source of 1 mm nominal diameter placed close to the center of the FOV with continuous white crystals. The FWHM obtained averaging the results of the two dimensions was 0.9 mm.

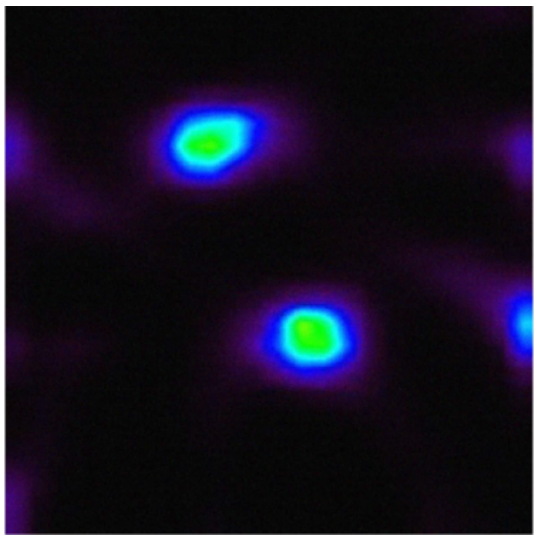

Figure 4.17: Transaxial view of two point-like sources reconstructed with the MLEM algorithm employing continuous white crystals. The FWHM was 1.1 mm in average.

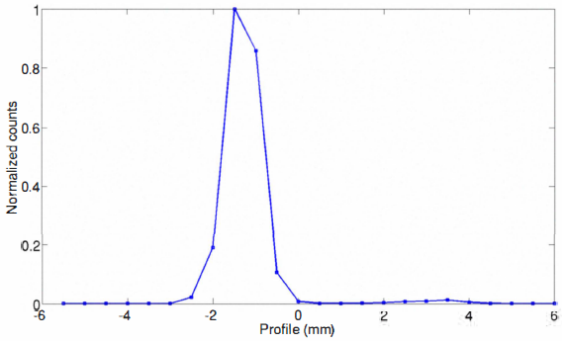

Figure 4.18: Example of a profile through the maximum of the reconstructed image of one of the sources of figure 4.17. The FWHM was 0.95 mm.

Figure 4.17 shows the reconstructed image of two point-like sources in the same transaxial plane with continuous white crystals. The average FWHM for the two sources was 1.1 mm. In order to determine these values, the profile through the maximum of the source distribution along the axes was obtained. The FWHM was determined employing linear fits. Fig 4.18 shows an example of one of these profiles, with a FHWM of 0.95 mm.

Figure 4.19 shows the reconstructed image of a disc source of non-uniform activity distribution. The image represents the field of view of 12 mm $\times$ 12 mm. The source diameter was known to be about 5 mm, which is consistent with the reconstructed image.

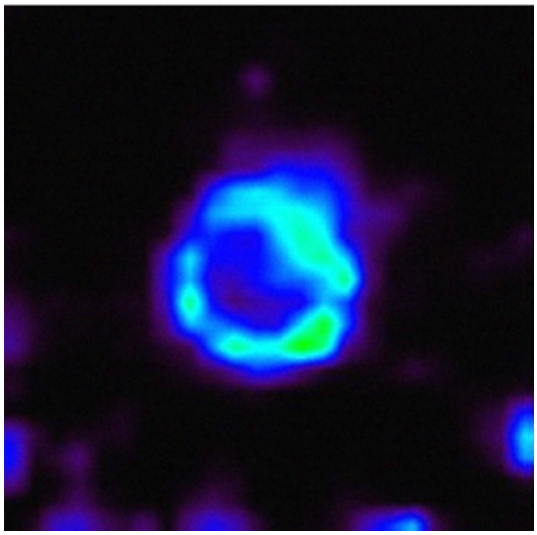

Figure 4.19: Reconstructed image of a disc source of non-uniform activity distribution. The source diameter was about 5 mm.

The version of the MLEM algorithm employed for the reconstruction of the previous images did not take advantage of the continuous nature of the crystals because of the discretization of the volumes of the crystals in order to obtain the LORs. With the aim of fully take advantage of continuous detectors, a second version of the MLEM algorithm was implemented [65], in which the coordinates of the estimated interaction position were stored in list-mode format. If the acquired data were represented in continuous space, the elements of the transition matrix required for MLEM could not be pre-calculated and stored, hence they were calculated on the fly. For accurate calculation of the transition matrix elements, the ray-end points corresponding to the estimated position interactions of two events of a given coincidence without discretization were used, including an uncertainty model. This algorithm, called Simulated One-Pass List-Mode (SOPL) [66], was adapted to this detector.

In order to test this approach, data were taken with a ^{22}Na point-like source of 0.25 mm nominal diameter at five different positions along the diagonal line of the detector and reconstructed with SOPL with the 5 mm thick white crystal, moving 1 mm in both x and y for each step. The absolute positions in the detector could not be determined. The nominal (0,0) position was taken as the closest achievable by the positioning system to the center of the crystal. The relative positions from one point to the next one were set with an accuracy about 0.3 mm FWHM. Figure 4.20 shows a profile of the reconstructed images of the five different positions. The differences in the peak height

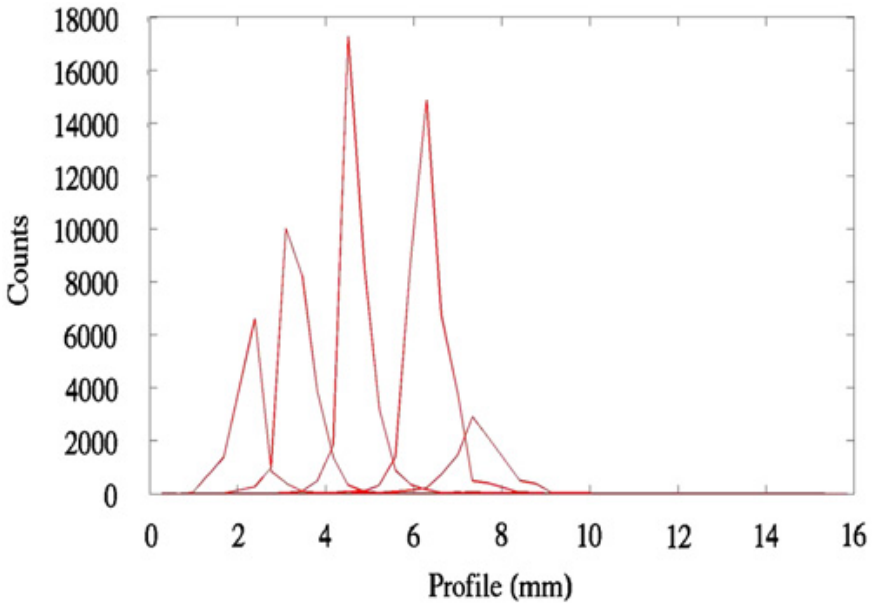

Figure 4.20: Profile of the reconstructed images along a diagonal line for the 5 mm thick crystal.

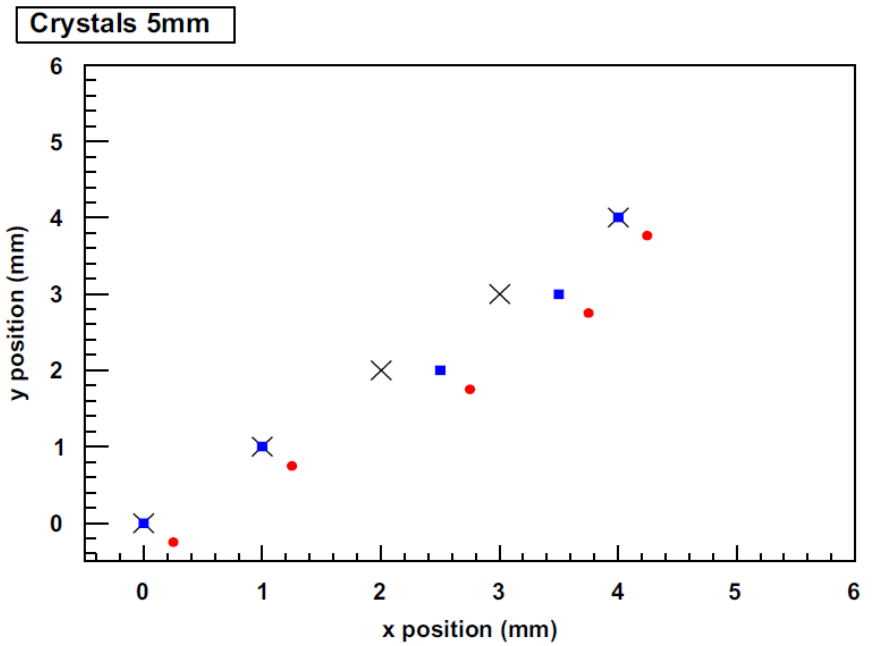

Figure 4.21: Nominal source positions along the diagonal (crosses) and maximum of the reconstructed positions (circles) for the 5 mm thick crystal. The squares represent the maximum of the reconstructed positions, shifted by the same offset.

Table 4.5: Reconstructed position along a diagonal for the 5 mm thick crystal.

Nominal	Reconstructed	X FWHM (mm)	Y FWHM (mm)	Average FWHM (mm)
0 , 0	0.25 , -0.75	0.93	0.66	0.78
1 , 1	1.25 , 0.75	1.04	0.7	0.87
2 , 2	2.75 , 1.75	0.72	0.67	0.70
3 , 3	3.75 , 2.75	0.8	0.71	0.76
4 , 4	4.25 , 3.75	0.67	0.79	0.73

were mainly due to misalignments in the source position along the diagonal, so that the profile was not taken at the maximum for all positions. Figure 4.21 shows the nominal source positions along the diagonal (crosses) and the maximum of the reconstructed positions (circles) for the 5 mm thick crystal. If a common shift was applied to the reconstructed positions (squares), the coincidence with the nominal positions was quite good in spite of the approximate source positioning system, with three points matching perfectly with the nominal position, and two more containing a constant shift in the *x* direction, and a perfect match in the *y* direction. The reconstructed position for each point is shown in table 4.5. The average FWHM measured from all of the positions, including *x* and *y* profiles, was 0.77 mm for the 5 mm thick crystal. The measurement was repeated with the 10 mm thick white crystal and the average FWHM obtained from all the positions was 0.81 mm.

4.6 Test of novel geometries

One of the most important and critical choices to be made was the selection of the scintillator crystal geometry. Apart from the traditional cuboid crystals, innovative scintillator geometries such as tapered crystals were considered for reduction of the gaps between detectors and therefore increase the full-ring sensitivity [67].

Simulations are a powerful tool for testing different geometries and their impact on detector behavior in an easy way. They also help to understand complex physical processes that take place inside the scintillator crystal or in the crystal-detector interface. A GEANT4 [68, 69] simulation of one detector head was implemented including generation and transportation of optical photons for a better understanding of its response and to predict its performance in different conditions [70]. The aim of the simulations carried out was not to have a perfectly accurate model of the detector, but to have a

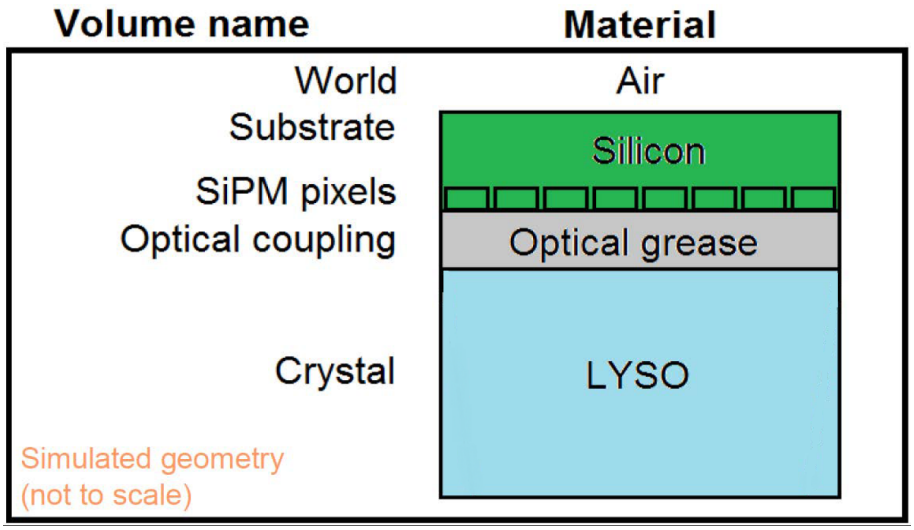

Figure 4.22: Schematic cross-section of the simulated geometry.

Table 4.6: Materials and properties

Material	Chemical composition	Density (g/cm^3)	Refractive index
Air	$N_{0.7}O_{0.3}$	1.29	1.00
Silicon	Si_1	2.23	4.24
Optical grease	$C_1H_1O_1$	1.00	1.70
Crystal	$Lu_{1.8}Y_{0.2}Si_1O_5$	7.1	1.81

relatively simple and fast tool to reproduce the experimental tests. This allowed us to understand the behavior of optical photons independently from other effects, like the readout electronics chain. Some approximations were made: the non-inclusion of the LYSO natural radioactivity and the simulation of 511 keV photons instead of a ^{22}Na source. This entailed excluding the second 1275 keV photopeak, the acolinearity and the scatter produced by the radioactive source holder. No energy cuts were applied.

The optical model employed to simulate the reflections of the optical photons in the crystal was the *unified* model. The crystal-air surface was simulated with the attribute *polished* and a reflectivity of 0.8. The SiPM elements were declared as sensitive detectors embedded on an inactive common silicon substrate. Each SiPM element is 1.5 mm $\times$ 1.4 mm with a 0.1 mm gap in one direction, reproducing the distribution of the real prototype described in section 4.2.1. A schematic cross-section of the simulation can be seen in figure 4.22 and a description of the material properties employed is

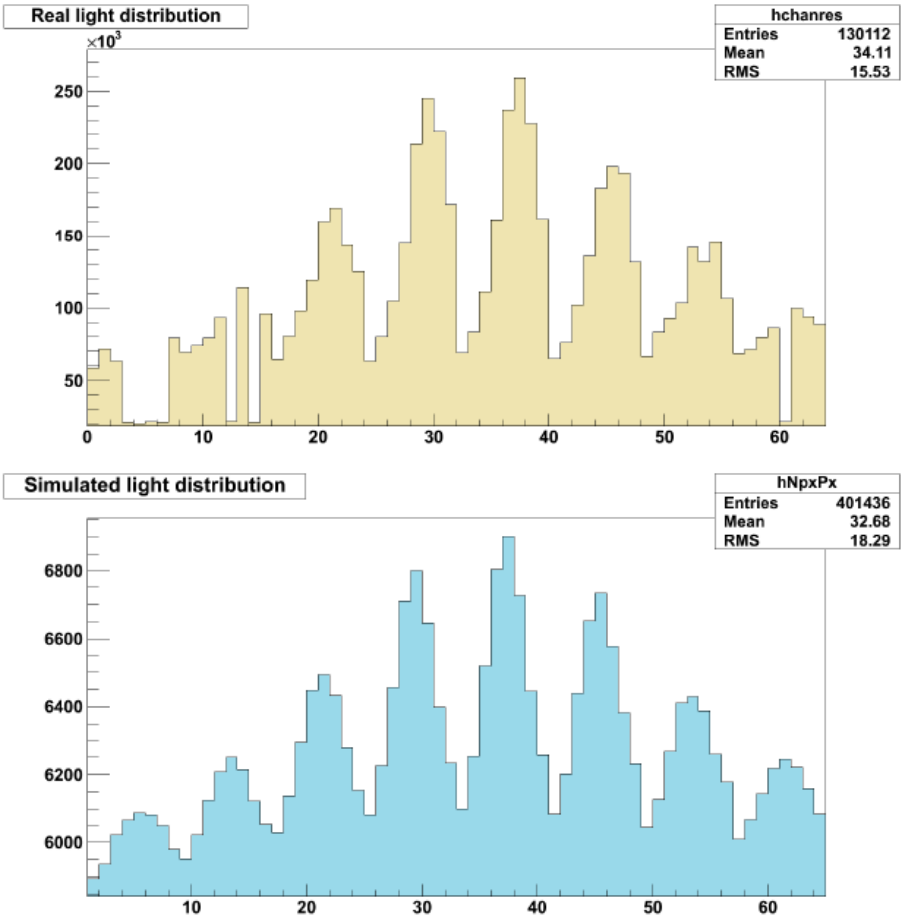

Figure 4.23: (Top) Real light distribution inside the 5 mm width cuboid crystal. (Bottom) Simulated light distribution inside the 5 mm width cuboid crystal.

shown in table 4.6. An intrinsic energy resolution of 7.3% was considered for the LYSO crystal [71].

The comparison of the simulated and experimental data was done in terms of light distribution, plotting the number of events measured in the photodetector versus the channel number. The optical photons that interacted in the sensitive elements of the SiPM array were considered for the data analysis. The 511 keV photon source simulated was a pencil beam oriented normally to the crystal surface and placed at different positions. Once a gamma ray had interacted inside the scintillator crystal, light was spread all over the crystal. Those SiPM elements immediately under the interaction position received more light, creating peaks in the light distribution. SiPMs elements further from the interaction position received less light, creating valleys. Groups of 8 channels were expected due to the geometric positioning of the SiPM pixels.

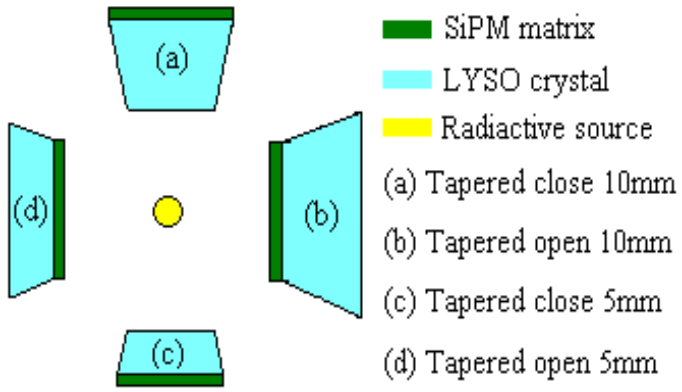

Figure 4.24: Tapered crystal geometries that were simulated.

For all crystal geometries, channels 3, 4, 5, 6, 12, 14 and 60 in the real detector gave no signal because they corresponded to dead channels.

4.6.1 Cuboid crystal geometry

A simulation of a cuboid geometry of a 12 mm $\times$ 12 mm LYSO crystal was carried out, with 5 mm and 10 mm width. Photons were simulated to interact in the center of the crystal and results were compared to real data obtained in the same position.

Figure 4.23 shows the comparison for the 5 mm width squared crystal between experimental data (top) and simulated data (bottom). Results showed good agreement between real and simulated data, demonstrating that our simulation was capable of reproducing experimental results.

4.6.2 Tapered crystals geometries

Once we had a simulation for cuboid crystals, tapered crystal geometries were implemented. The use of tapered crystals allows to reduce the gap between detectors. In addition, the placement of the photosensor in the entrance surface of the crystal was expected to improve the performance of the detector in comparison with the conventional placement of the photosensor on the rear surface of the crystal in terms of DOI positioning accuracy [72], so this approach was also included in the simulations. A schematic view of the four simulated tapered geometries can be seen in figure 4.24. Two main configurations based on tapered crystals were implemented. One of them was with the placement of the photosensor on the rear surface of the crystal, so in order

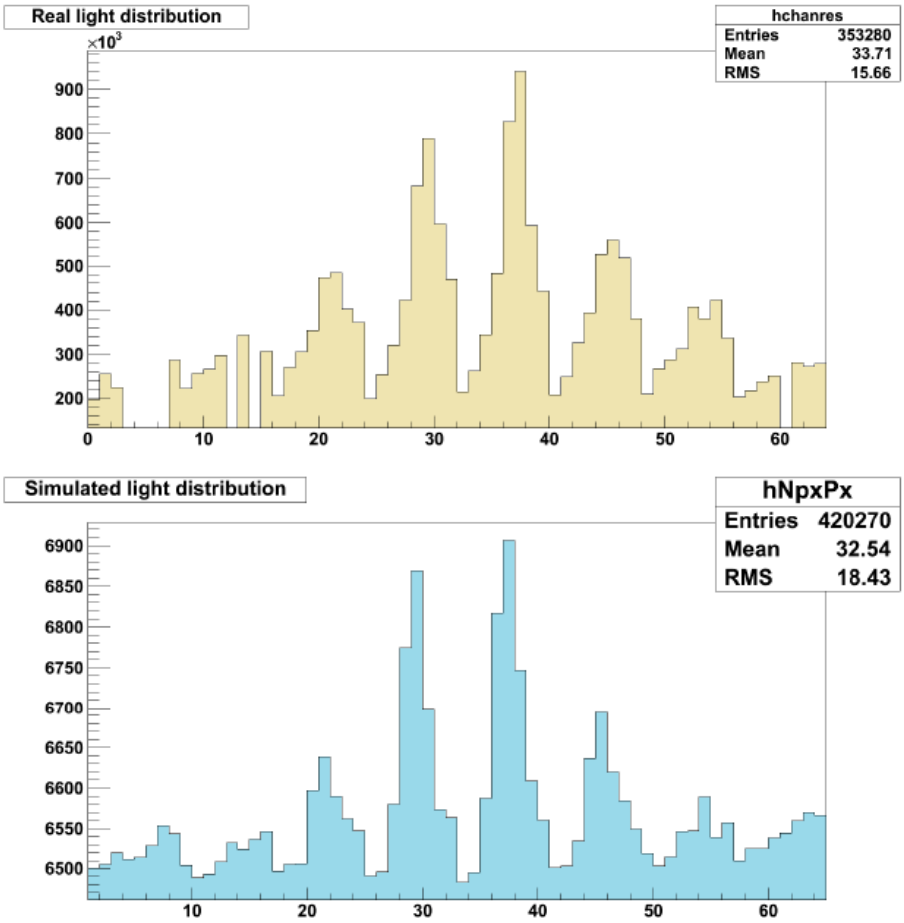

Figure 4.25: (Top) Real light distribution inside the 5 mm tapered close crystal. (Bottom) Simulated light distribution inside the 5 mm tapered close crystal.

to form a ring of detectors the crystal must *close* towards the center of the scanner to allow the positioning of the rest of the crystals (*tapered close*, figure 4.24 a and c). The other one was with the placement of the photosensor in the entrance surface of the crystal, so in order to form a ring of detectors the crystal must *open* to allow the positioning of the rest of crystals (*tapered open*, figure 4.24 b and d).

First, a simulation for the 5 mm width tapered crystal was carried out and the light distribution was compared to experimental data. Figure 4.25 shows the comparison for the 5 mm width tapered close crystal between experimental data (top) and simulated data (bottom). Results showed good agreement between real and simulated data, so the remaining tapered geometries were simulated.

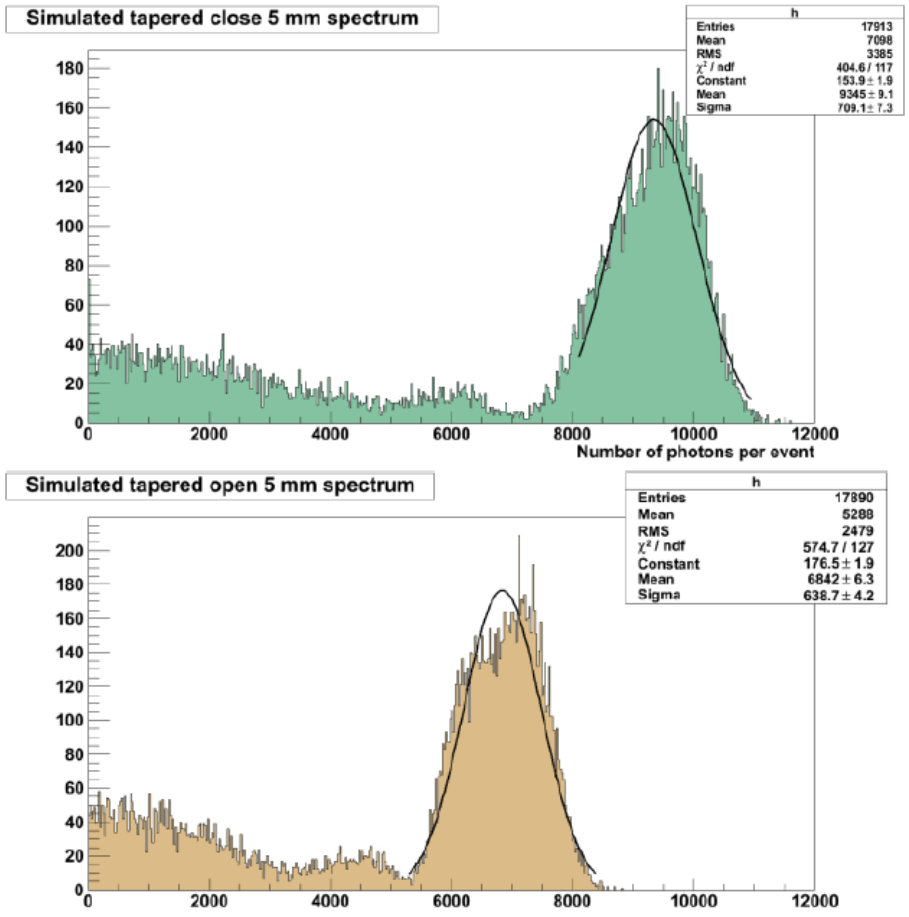

Figure 4.26: (Top) Simulated tapered close 5 mm spectrum. (Bottom) Simulated tapered open 5 mm spectrum.

Table 4.7: Tapered close vs. tapered open

Crystal	Peak position	Energy resolution
Tapered close 5 mm	9345	17.8% FHWM
Tapered open 5 mm	6842	21.9% FWHM

4.6.2.1 Tapered open vs. tapered close

In order to obtain more information about the behavior of the optical photons inside the different tapered geometries, a 5 mm width tapered open crystal was simulated and compared to the previous 5 mm width tapered close crystal simulation.

Figure 4.26 shows the simulated energy spectrum for the 5 mm tapered close crystal and the 5 mm tapered open crystal. Based on the photopeak position, more

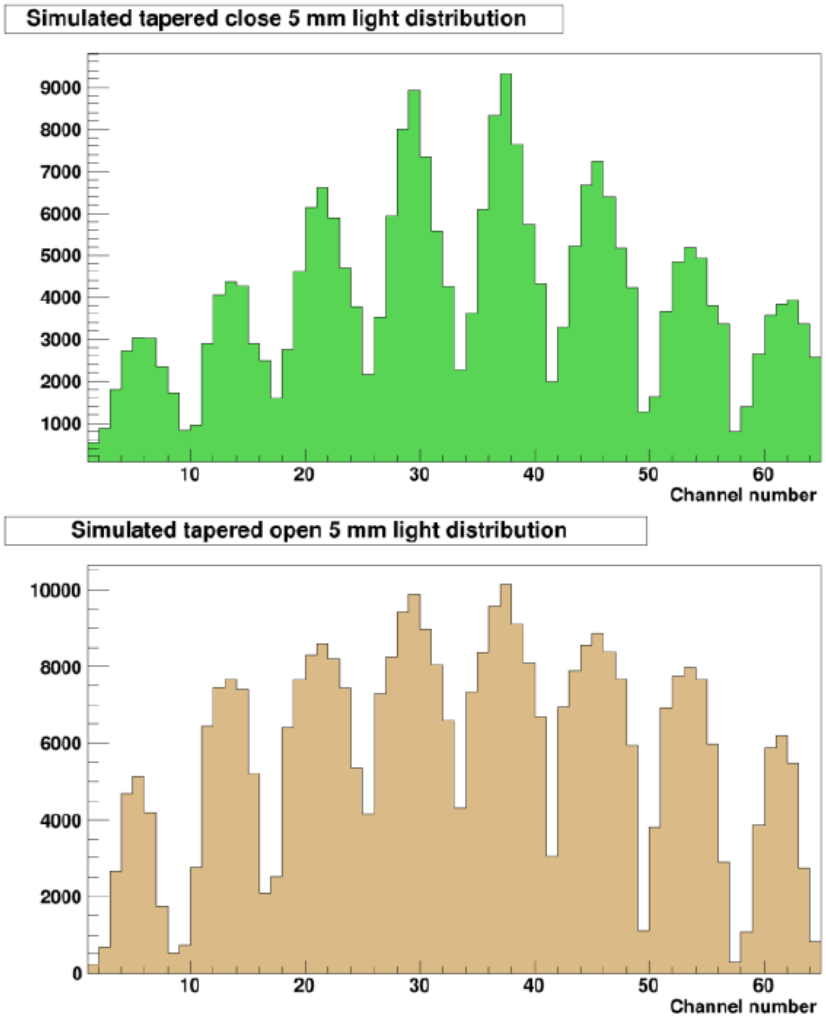

Figure 4.27: (Top) Simulated tapered close 5 mm light distribution. (Bottom) Simulated tapered open 5 mm light distribution.

photons reached the photodetector in the tapered close configuration. The energy resolution of the 5 mm tapered close configuration was 17,8% FWHM meanwhile the 5 mm tapered open configuration was 21,9% FWHM. These results are summarized in table 4.7. The anomalies in the photopeak shape were probably due to geometrical factors and how the light was reflected on the sides of the tapered crystals.

Figure 4.27 shows the difference in the simulated light distribution inside the crystal between the 5 mm tapered close crystal and the 5 mm tapered open crystal when the same number of channels were illuminated. It can be seen that the background produced in the tapered open crystal is larger than the background in the tapered close.

4.6.2.2 Position determination

The position determination method explained in section 2.3 was applied to the tapered open and tapered close geometries employing the coincidence setup mentioned in 4.4.6 and represented in figure 4.11. Real data were obtained in four different points of the crystal and compared to simulations carried out in the same four points. The center of the crystal was taken as the (0,0) position. The experimental measurements did not have an absolute reference frame, but the relative distances were set with micrometer accuracy. Points 1, 2 and 3 were separated 2 mm in x direction and point 4 was separated 2 mm in y direction from point 2.

Figure 4.28 shows a comparison between real data and simulated data for the 5 mm tapered close crystal in the position determination. Quantitative results can be seen in table 4.8.

Figure 4.29 shows a comparison between real data and simulated data for the 5 mm tapered open crystal in the position determination. Quantitative results can be seen in table 4.9.

Results obtained with the simulations of tapered crystals showed a different light behaviour for different geometries, as expected, showing also good agreement with experimental data. This demonstrated that our simulation could also be employed with tapered crystals geometries. Nevertheless, the position determination algorithm employed was exactly the same developed for cuboid crystals and it was not adapted to tapered crystals. For this reason, position determination results are expected to improve if the algorithm were adapted and took into account the particularities of each of the tapered geometries employed.

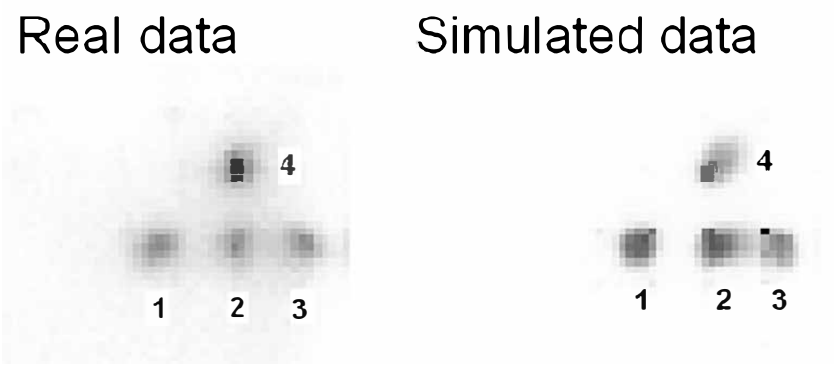

Figure 4.28: Position estimation in tapered close 5 mm in real data (left) and simulated data (right).

Table 4.8: Reconstructed FWHM (mm) in tapered close 5 mm

Point	Nominal position	Real data	Simulated data
1	1 , 1	1.07	1.02
2	3 , 1	1.02	1.05
3	5 , 1	0.71	1.23
4	3 , 3	0.95	0.77

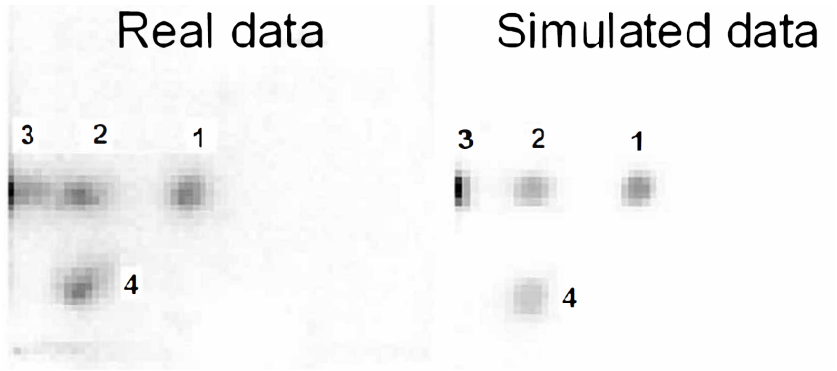

Figure 4.29: Position estimation in tapered open 5 mm in real data (left) and simulated data (right).

Table 4.9: Reconstructed FWHM (mm) in tapered open 5 mm

Point	Nominal position	Real data	Simulated data
1	-1 , -1	1.00	0.88
2	-3 , -1	0.89	0.98
3	-5 , -1	0.78	1.03
4	-3 , -3	0.61	1.12

4.7 Conclusions

In this chapter, different characterization tests were carried out to assess the feasibility of applying the technology based on continuous crystals and SiPMs in the development of a first prototype of a small animal PET scanner.

The comparison study between three different types of painting applied to the crystal surfaces showed that the white crystal offered a much better performance in terms of energy and timing resolution. Besides, the interaction position determination method applied showed that it was capable of reconstructing the interaction position with submillimetre spatial resolution, even near the edges of the crystal and without any previous calibration. For these reasons, white crystals were chosen to mount a rotating system consisting of two detector heads. First tomographic images of point-like sources were obtained with a FWHM close to one millimetre.

Since the performance of the detector head was good, a GEANT4 simulation was carried out to assess the possibility of employing different types of geometries, including tapered crystals, in a future version of the prototype. Out of the framework of this thesis, more simulations of the system were carried out, together with the acquisition of more experimental data, in order to improve the position determination method. Results were published in [22] and they represent the core of another thesis developed inside the IRIS group.

The results presented in this chapter were promising, encouraging the development of a second version of a small animal PET. The idea of building a full-ring scanner made it necessary to consider new readout electronics, being the VATA64HDR16 ASIC the chosen option. A full characterization of this ASIC is shown in chapter 5. The second prototype of the small animal PET is fully explained in chapter 6.

Chapter 5

Performance of VATA64HDR16 ASIC for medical physics applications based on continuous crystals and SiPMs

5.1 Introduction

As explained in previous chapters, both hadron therapy and PET applications reached a point in which the readout electronics employed in the detectors needed to increase the number of readout channels. In this situation, a cost effective approach was to develop a versatile Data Acquisition (DAQ) system employing the same ASIC for both applications. This approach allowed us to unify both research lines and to carry out the developments within our research group. The main issue was that the hadron therapy application employed MPPC arrays with positive output polarity and the PET application employed SiPM matrices with negative output polarity. Besides, SiPMs available at that time had a wide spread in the breakdown voltage of the pixels in the array due to the manufacturing technology available.

The search of ASICs in the market at that time was very limited because there were no ASICs specifically designed to work with continuous crystals. Some available ASICs were under development and they had a reduced number of channels. Moreover, these ASICs were usually designed for a specific input polarity, limiting the type of SiPMs used with them. Some ASICs employed for the readout of scintillator crystals and SiPMs were: NINO [73], MAROC [61], SPIROC [35], PETA [74], BASIC [75],

Table 5.1: Some characteristics of ASICs employed for the readout of SiPMs.

ASIC	Number of channels	Input polarity	Dynamic range
NINO	8	+	300 pC
MAROC	64	-	80 pC
SPIROC	36	+	200 pC
PETA	40	+	-
BASIC	32	-	70 pC
TOFPET	64	-/+	200 pC
VATA64HDR16	64	-/+	-20 to 55 pC

VATA64HDR16 [76] and TOFPET [77]. Some characteristics of these ASICs can be seen in table 5.1. The use of any of these ASICs with continuous crystals would lead to a limited performance and results.

The VATA64HDR16 ASIC from Ideas [78] was chosen for several reasons: it had a large enough number of channels, it was capable of working with both positive and negative input signals and it allowed to adjust the bias for each channel independently. Besides, the research group had previous experience with other chips of the same family for other applications and a DAQ board previously developed by the group could be adapted to operate this ASIC.

This chapter describes the tests carried out with the VATA64HDR16 ASIC, which was employed in the second version of the Compton telescope and PET prototypes. The results presented here are not intended to achieve the best possible performance of the ASIC, but to evaluate its response in a particular situation for a given application [79].

5.2 Experimental setup

5.2.1 ASIC

The VATA64HDR16 is a 64-channel, charge sensitive ASIC optimized for energy and timing measurements with SiPM detectors. It is developed under a 0.35 μm CMOS manufacturing process. It is based on a combination of the existing ASICs VA32_HDR14.2 and TA32cg from Ideas. The functionality of these previous ASICs

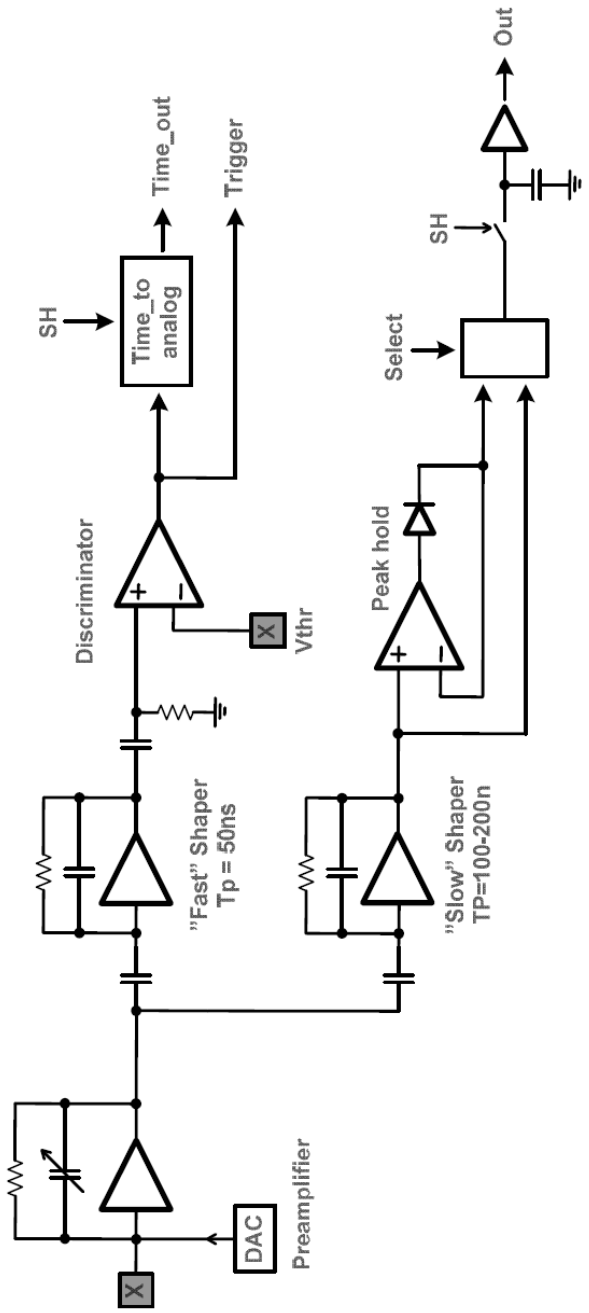

Figure 5.1: VATA64HDR16 single channel diagram.

had been complemented with new functionalities tailored for SiPM read-out [80]. Tests performed with this ASIC by other research groups are shown in [76, 81].

Each channel consists of a charge sensitive preamplifier, a circuit for amplitude spectroscopy and a circuit for triggering and timing. The preamplifier gain can be set

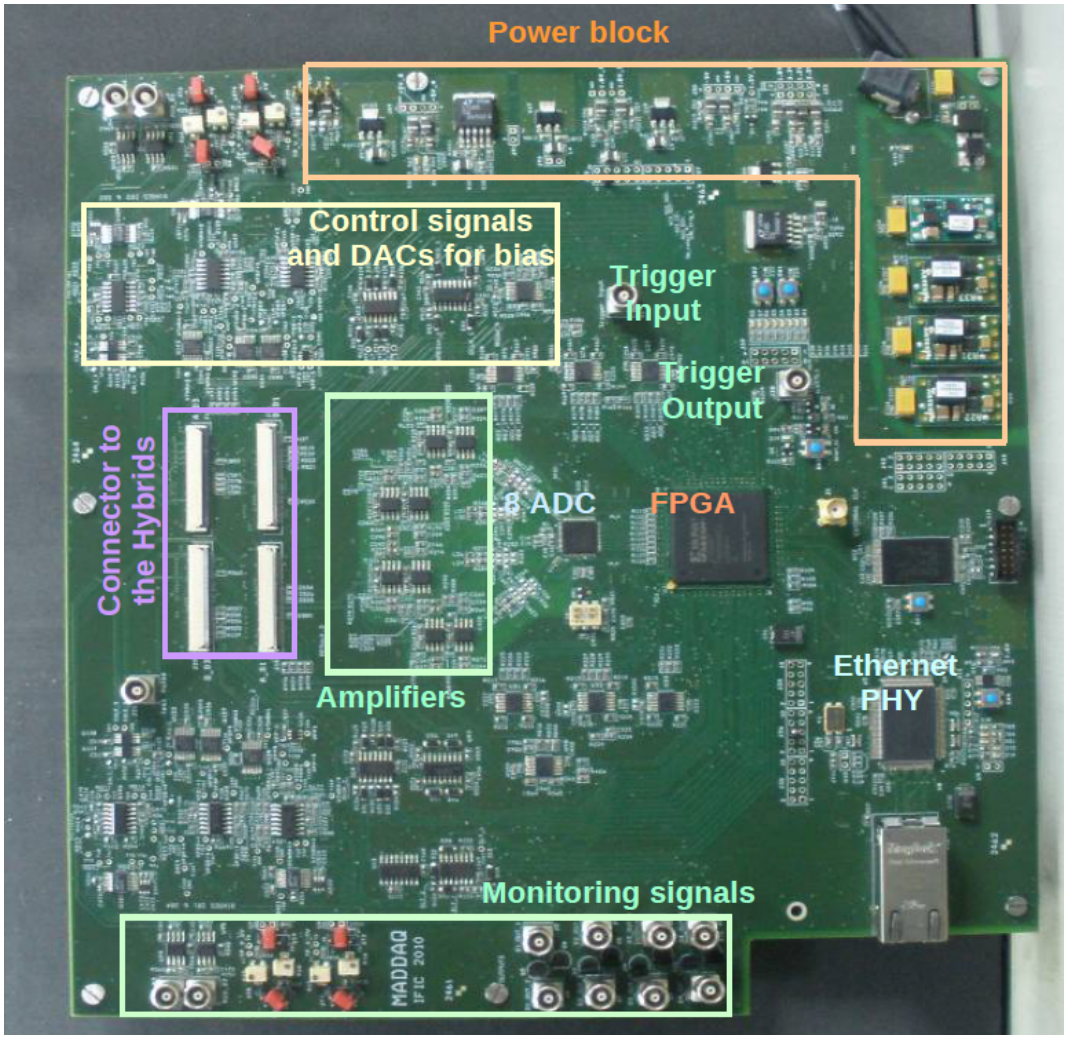

Figure 5.2: Custom made data acquisition system based on the VATA64HDR16 ASIC.

to a low gain mode or a high gain mode by changing the feedback capacitance. The preamplifier input works with both positive and negative input charges, although it is optimized for positives, and it can be connected directly to the SiPM. The preamplifier input potential can be programmed through a 8-bit digital-to-analog converter (input DAC) in each readout channel allowing to adjust the bias voltage of each SiPM individually. The input potential can be decreased from a reference voltage in steps of 3.5 mV within a range of almost 1 V. In systems with many SiPMs, the input DACs can be used to adjust variations in the operating voltage or to actively control the operating point as the SiPMs temperature or bias voltage changes. A block diagram of one channel of the VATA64HDR16 ASIC can be seen in figure 5.1.

The ASIC has a slow shaper and a fast shaper. The slow shaper is meant for amplitude spectroscopy and its shaping time can be set to 50 ns, 100 ns, 150 ns or 300 ns. The default value for the slow shaper is 100 ns and all measurements shown in this paper are performed with that value. The fast shaper provides the trigger signal. The fast shaping time is fixed to 50 ns. The discriminator triggers when the output of the fast shaper exceeds the discriminator programmable threshold. All channels can be read out via the back-end which contains a multiplexer and an output buffer that delivers a differential current and a differential voltage output. Both current and voltage outputs were tested and differential current output showed a more linear behavior than the differential voltage output. For this reason, all measurements performed in this chapter were carried out with the differential current output.

5.2.2 Detector

The VATA64HDR16 ASIC was glued and wire-bonded on a custom made printed circuit board (PCB) that provided the bias voltage for the SiPM arrays and mechanical support. The ASIC was encapsulated with Dymax Multi-cure 9001-E-V3.5 [82] to protect the bonds. Each PCB was connected to a custom made data acquisition (DAQ) board equipped with a 12-bit ADC on board and an FPGA Spartan3 from Xilinx that controlled the acquisition process and that was connected to the computer through Ethernet connection [83]. A picture of the DAQ board can be seen in figure 5.2. A graphical C++ user interface allowed to control the ASIC parameters. Data taking generated an ASCII output file with a line per event detected. For each event, the ADC value of the 64 channels was recorded.

The SiPM employed in the measurements performed in this chapter was a MPPC array from Hamamatsu Photonics model S11064-050P(X1) with 16 channels of 3×3 mm^2 size and 3600 microcells, as the ones employed for the Compton telescope in chapter 3. The external dimensions of the device were 16×18 mm^2. This model was chosen because each channel had an independent anode and cathode, so a positive or a negative output polarity could be obtained depending on the bias scheme. The 16-channel MPPC array covered one quarter of the 64 channels of the ASIC, as it can be seen in figure 5.3 (a).

For the energy resolution studies, LYSO and $LaBr_3$ monolithic scintillator crystals of $16\times18\times5$ mm^3 were employed (figure 5.3 (b) and (c), respectively), covering the whole MPPC surface. LYSO crystals were polished and painted in white in five faces,

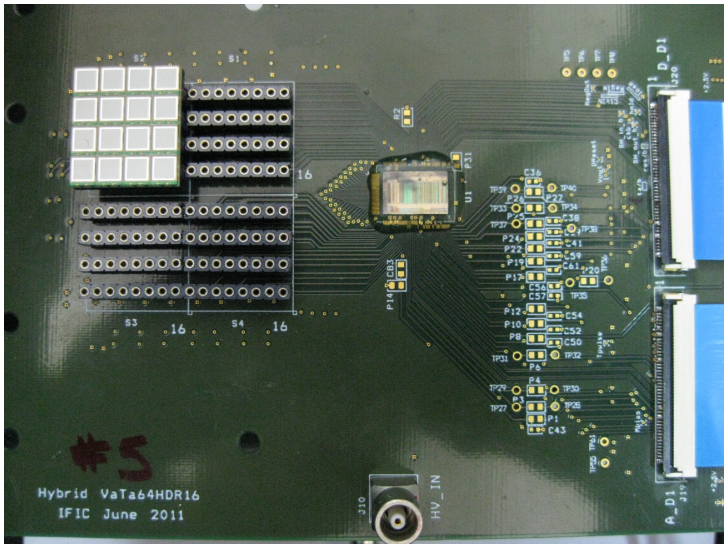

(a)

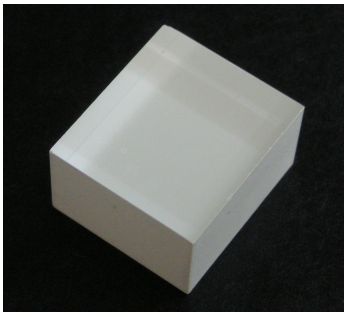

(b)

(c)

Figure 5.3: (a) Picture of the PCB containing the VATA64HDR16 ASIC and the MPPC array. (b) LYSO crystal of $16\times18\times5$ mm^3. (c) $LaBr_3$ crystal of $16\times18\times5$ mm^3 surrounded by reflective material and encapsulated in an aluminum housing.

being the non-painted face the one attached to the SiPM. The $LaBr_3$ crystal was surrounded with reflective material and encapsulated in an aluminum housing because of its hygroscopicity.

For the coincidence timing resolution measurement, two LYSO crystals of $12\times12\times5$ mm^3 covering 9 out of the 16 MPPC channels were employed in order to perform the measurement with two equal crystals. No optical grease has been employed to couple the scintillator crystals to the MPPCs because tests performed in the laboratory showed a malfunctioning of the MPPC array and a dramatic increase in its current when optical grease was used to attach the scintillator crystal to the SiPM, probably due to the fact that there was no coating between SiPM elements in the MPPC.

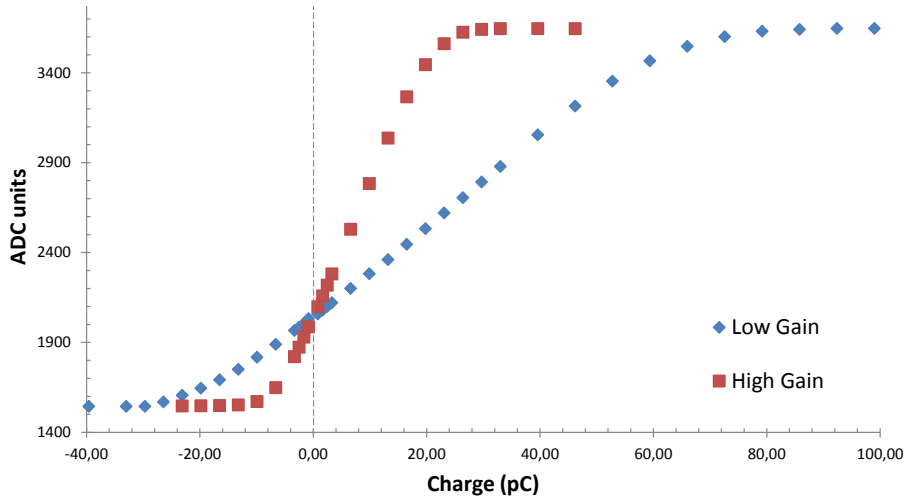

Figure 5.4: Input charge range for low gain and high gain in a single readout channel.

5.3 ASIC characterization

In order to assess the performance of the VATA64HDR16 ASIC, several tests on different characteristics were performed.

5.3.1 Input charge range

As a first step, the dynamic range of the ASIC for positive and negative charges in low gain and high gain configuration was tested. A voltage pulse through a 33 pF capacitor was used to inject charge to one channel of the ASIC. The ADC value of the channel was recorded in order to establish a correlation between injected charge and ADC units.

Figure 5.4 shows the ASIC response to the input charge for both polarities and for both gain configurations. The input charge range for low gain configuration was approximately from -20 pC up to 55 pC before saturation started, whereas for the high gain configuration it went from -6 pC until 10 pC, approximately. The ADC range for positive input charges was of 1900 ADC units, but it was reduced to 500 ADC units with negative input charges. These results demonstrated that the performance of this ASIC for negative input charges was limited and it was optimized for positive charges, as stated in the ASIC specifications.

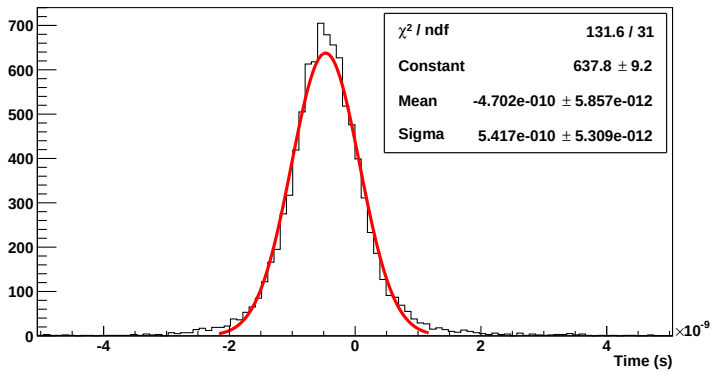

Figure 5.5: Intrinsic coincidence timing resolution of 1.3 ns FWHM.

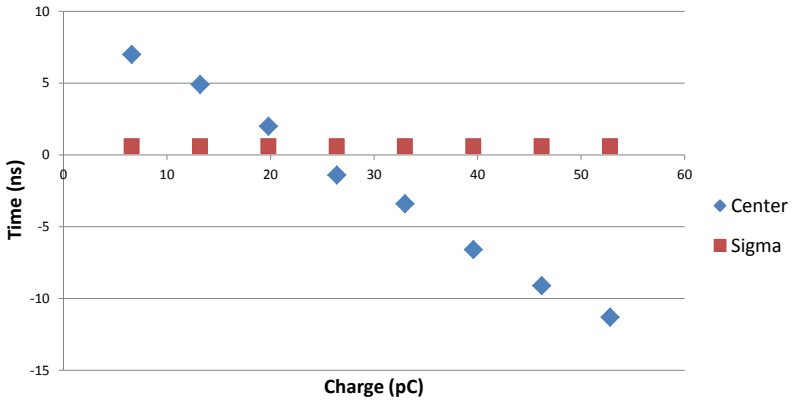

Figure 5.6: Position of the center of the intrinsic coincidence timing resolution distribution as a function of the input charge.

5.3.2 Intrinsic coincidence timing resolution

In order to measure the intrinsic timing resolution, two different ASICs were employed. To make conditions similar, a pulse was generated and split so that the same pulse was sent to the same channel number in both ASICs. The threshold was adjusted to the same level in both ASICs to reject noise. Trigger signals coming from the ASICs were connected to an oscilloscope LeCroy WavePro 950 and the time difference between them was measured through a histogram. A Gaussian function was employed to fit the distribution and obtain the FWHM.

First, a noise of 0.3 ns due to fluctuations in the power line was measured. Then, an intrinsic coincidence timing resolution of 1.3 ns FWHM was obtained with the pulse generator. The timing distribution can be seen in figure 5.5.

The amplitude of the input pulse was varied and the position of the center of the

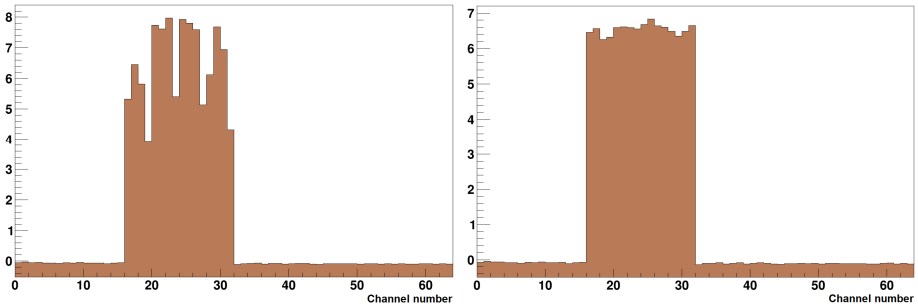

(a) (b)

Figure 5.7: Detector response before (a) and after (b) applying voltage corrections to individual channels.

timing distribution and its sigma were represented in figure 5.6. The input charge range tested corresponded to the linear part of the positive, low gain mode of the ASIC (from 0 to 55 pC). While the sigma of the distribution remained constant, it can be seen that the center of the timing distribution had a strong dependence on the input charge (timewalk). This will affect the measurements with real detectors, where the charge produced in each event is different (see section 5.3.6).

5.3.3 Input DACs equalization

In order to make the detector response uniform, input DACs were employed to adjust the bias voltage applied to each channel. Instead of using a pixelated crystal for this measurement, the continuous $LaBr_3$ crystal coupled to the MPPC array was employed. To provide similar signals to all channels, the detector was connected to the ASIC and a ^{22}Na source was placed 10 cm away, a distance far enough to ensure an homogeneous distribution of the emitted gamma interacting in the crystal.

Input DAC values were initially disabled and events were recorded in ADC units and normalized to 1. The channel with less hits recorded was taken as reference and no input DAC was applied to it. The input DAC values of the channels with larger values than the reference channel were increased in order to decrease the bias voltage applied until the difference in the number of hits recorded among channels is less than 1%. Figure 5.7 (a) shows a histogram of the number of hits recorded per channel when no input DACs were applied. Differences of up to 4% in the number of hits recorded among channels were obtained. Figure 5.7 (b) shows the effect of optimizing the

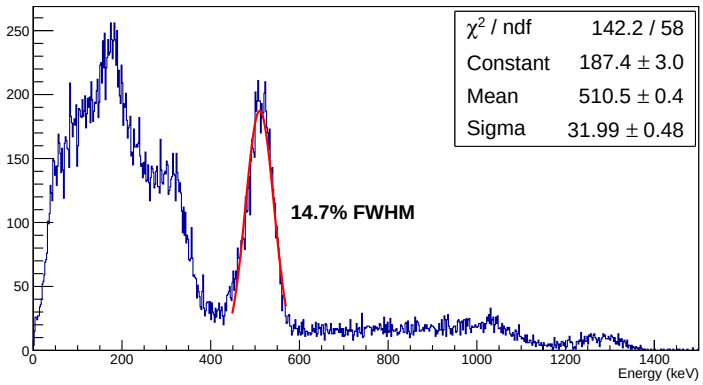

(a)

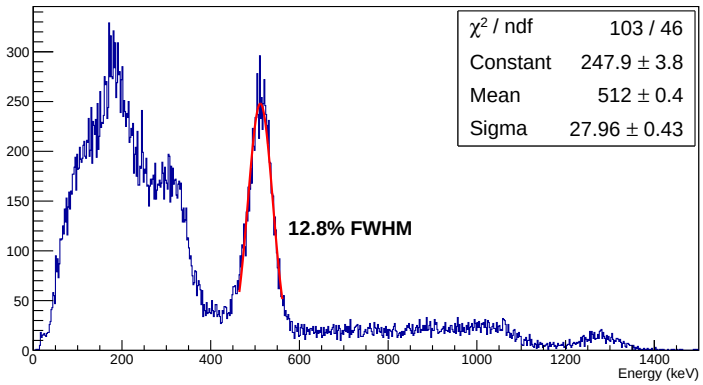

(b)

Figure 5.8: ^{22}Na spectra when no input DACs were applied (a) and when they are applied (b).

individual bias voltages, reducing the difference in the number of hits recorded per channel to less than 0.6%.

Once the detector response was equalized, data were taken to evaluate the effects of the input DACs on the energy resolution. The ^{22}Na source was placed close to the crystal in order to increase the rate and energy spectra were taken. In terms of energy resolution, an improvement of about 2% FWHM is obtained when the input DACs were applied, as it is shown in figure 5.8.

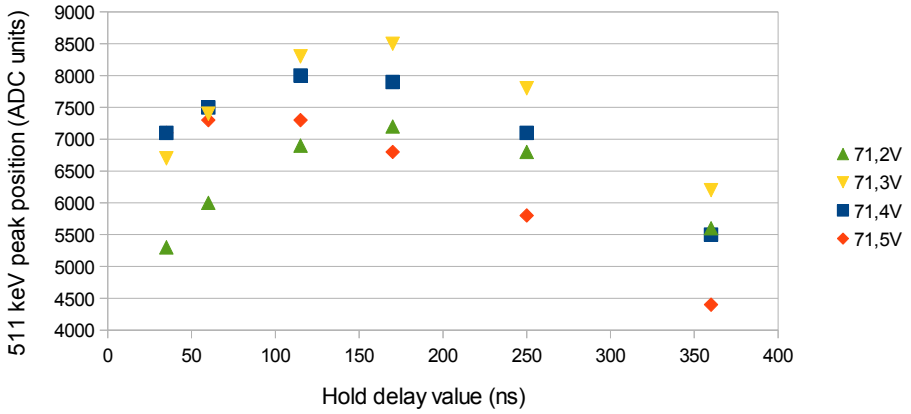

Figure 5.9: Position of the 511 keV photopeak as a function of the Hold Delay value for different bias voltages.

5.3.4 Hold delay selection

The hold delay parameter allows to choose the time elapsed from the moment in which an event surpasses the threshold until it is sampled. The aim is to sample the signal in its maximum, in order to get all the energy information. Different hold delay values were tested in order to identify the values that were better adjusted to the peak of the pulse and thus yielded the best results. ^{22}Na spectra were acquired with several bias voltages (from 71.2V to 71.5V in 0.1V steps) and different hold delay values (35, 60, 115, 170, 250, 360 ns) for each value of the bias voltage, employing the $LaBr_3$ scintillator crystal and low gain mode. For each acquisition, the 511 keV photopeak was fitted with a Gaussian function and its position in ADC units was recorded.

Figure 5.9 shows the position of the 511 keV photopeak as a function of the hold delay value for four different bias voltages. It can be observed that for each bias voltage, the 511 keV peak position increased until it reached a maximum, then it started to decrease. A hold delay value of 170 ns was selected for data taking in the remaining measurements, given that it corresponded to the peak of the distribution and it provided the largest amount of light recorded.

5.3.5 Energy resolution studies

Energy resolution measurements were carried out employing a ^{22}Na source and a MPPC array coupled to LYSO and $LaBr_3$ crystals of $16\times18\times5$ mm^3 size. The MPPC array was biased with positive and negative voltages, in order to assess the

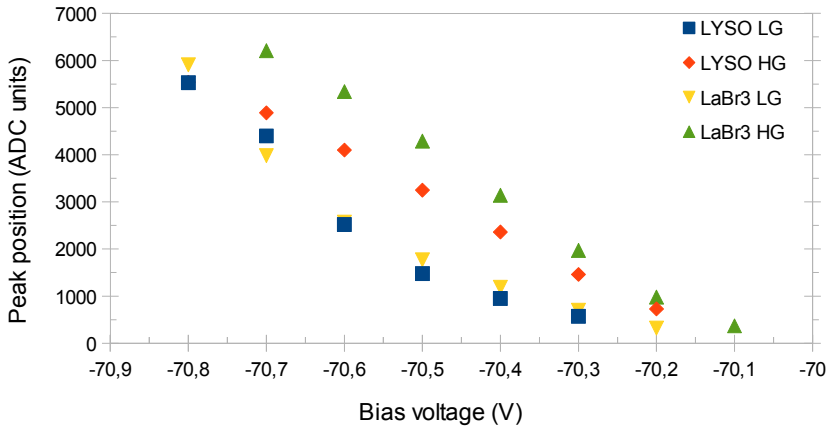

(a)

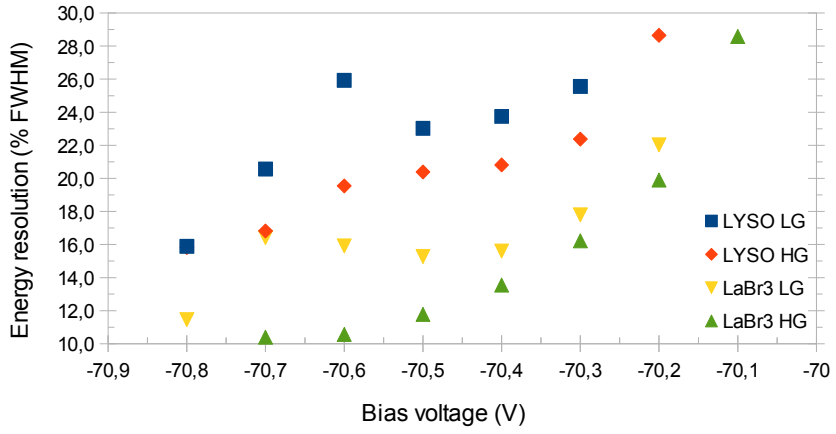

(b)

Figure 5.10: (a) 511 keV peak position for negative biases (b) energy resolution for negative biases.

performance of the ASIC to positive and negative inputs. For each case, low gain (LG) and high gain (HG) configurations were tested. The positive and negative bias voltages tested are the only values in which the detector generates a trigger, limiting the range of bias voltage that can be employed for detector operation.

Figure 5.10 and 5.11 show the results obtained with negative and positive biases, respectively. Figure 5.10 (a) shows the 511 keV peak position in ADC units as a function of the bias voltage for negative voltages, following an almost linear behavior. Figure 5.10 (b) shows the energy resolution obtained for each negative bias, being around 10% FWHM and 16% FWHM the best values obtained for $LaBr_3$ and LYSO, respectively. Figure 5.11 (a) shows the 511 keV peak position in ADC units as a

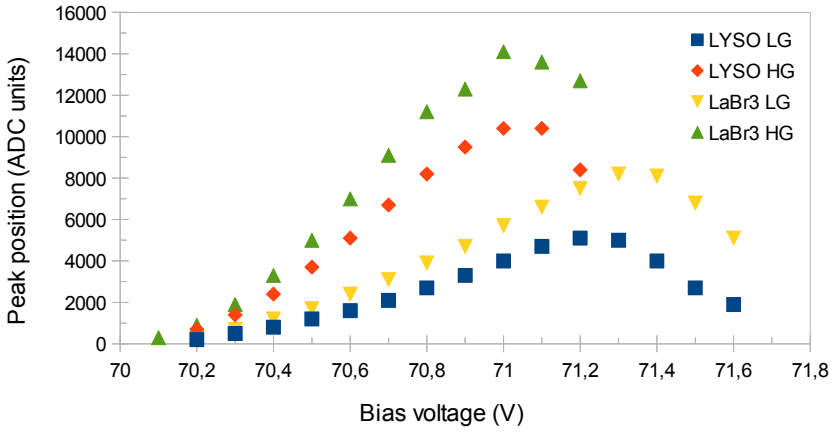

(a)

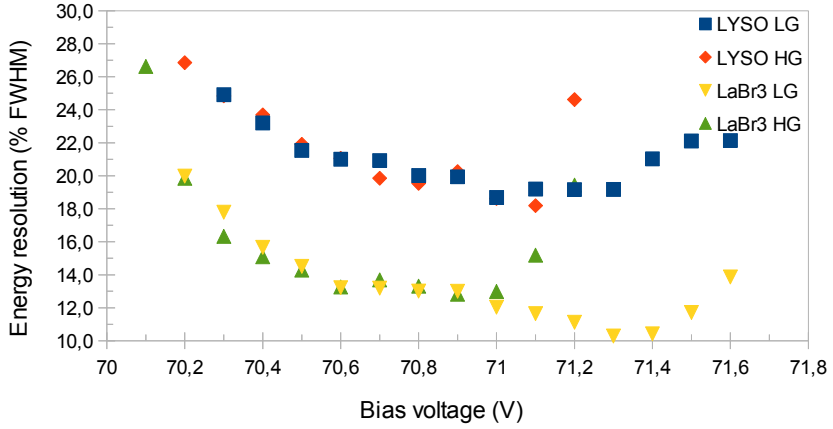

(b)

Figure 5.11: (a) 511 keV peak position for positive biases (b) energy resolution for positive biases.

function of the bias voltage for positive voltages. The peak position increased until it reached a peak and then it decreased. Figure 5.11 (b) shows the energy resolution obtained for each positive bias, being around 10% FWHM and 18% FWHM the best values obtained for $LaBr_3$ and LYSO, respectively.

The best energy resolution obtained with the $LaBr_3$ scintillator crystal was 10% FWHM at 511 keV, far from the 5.8% FWHM obtained with the same $LaBr_3$ crystal attached to a PMT and employing optical grease [84]. Results of energy resolution could be limited due to the fact that the MPPC model S11064 has a 50% of dead space because of the gaps between SiPM elements, meaning that half of the photons

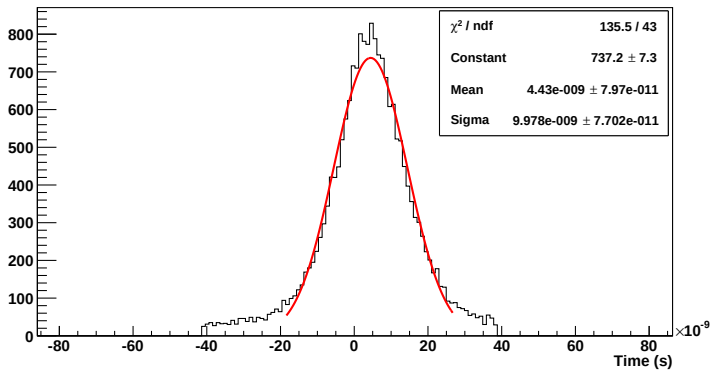

Figure 5.12: Coincidence timing resolution of 24 ns FWHM with two LYSO detectors.

reaching the photodetector were lost. An energy resolution of 7.1% FWHM would be expected if no photons were lost due to the dead area. Energy resolution improvement would also be expected if optical grease could be employed with this MPPC model.

5.3.6 Coincidence timing resolution

For this measurement, two detectors working in time coincidence and low gain mode were employed. In order to ensure a similar response in both detectors, two crystals of the same dimensions were selected. Each detector consisted of a $12\times12\times5$ mm^3 LYSO crystal coupled to a MPPC array biased with positive voltage and connected to the VATA64HDR16 ASIC. Detectors were separated by a distance of 60 mm and the ^{22}Na source was placed in the middle. Triggers coming from each detector were connected to an external custom made coincidence board which generated an output signal whenever the two input signals performed a logic AND. The output signal of the coincidence board was used as an external trigger to record the coincidence event in each detector.

A coincidence timing resolution of 24 ns FWHM was obtained, as it can be seen in figure 5.12. As mentioned in section 5.3.2, the timing distribution has a strong dependence on the input charge (timewalk). It can be seen in figure 5.6 that the difference in the center of the timing distribution was up to 20 ns for the whole input range of the positive, low gain mode of the ASIC. This could explain the poor results obtained with the real detector. In order to minimize timewalk and obtain a better timing resolution in the case of PET applications, the threshold should be set high enough to select only the events contained in the photoelectric peak. In this configuration,

this was not possible. The threshold value applied to both detectors was the highest possible, corresponding to an energy cut around 300 keV.

Moreover, the fact that the ASIC generated a trigger when any of the 64 channels surpasses the threshold level (OR trigger) was appropriate for pixelated crystals, in which a photon interacting in any position within the crystal would generate enough light to exceed the threshold level and trigger the readout of the event. In continuous crystals, even for a high energy deposition, the light detected by a single SiPM element can be very low, especially if the event has taken place far from the SiPM side of the crystal. In this situation, signals generated by single SiPM channels can have low amplitude not surpassing the threshold level, although they are associated to a non-negligible amount of light. In PET applications, an appropriate threshold to select events in the photoabsorption peak would be more suitable. Trigger signal should be generated when the sum of the energy deposited in the 64 channels surpasses the threshold value. In Compton imaging, since the energies of interest cover a wide range, a constant fraction discriminator strategy could be an effective approach.

5.4 Conclusions

In this chapter, several tests were carried out to test the performance of the VATA64HDR16 ASIC from Ideas for medical physics applications based on continuous crystals and SiPMs. The aim was to assess its suitability for our applications. Based on the results obtained, the performance of the VATA64HDR16 ASIC is not optimum, but it fulfils our needs.

The VATA64HDR16 ASIC has been successfully employed in the second version of the Compton telescope prototype described in chapter 3. Results of this second prototype can be found in [39] and in-beam tests with the system are described in [40].

The VATA64HDR16 ASIC has also been employed in the second version of the small animal PET prototype described in chapter 4. Results of this second prototype are presented in chapter 6.

Chapter 6

Second prototype of a small animal PET based on SiPMs and continuous LYSO crystals

6.1 Introduction

The first prototype of a small animal PET based on SiPMs and continuous LYSO crystals, described in chapter 4, was successfully operated. The results obtained were promising and demonstrated the feasibility of the technology, so efforts were focused on making it scalable to a full-ring geometry of 16 detector heads. With this aim, a second prototype of a small animal PET was developed and a first characterization was carried out. The need of operating the 16 detector heads in coincidence and handling a high number of readout channels forced us to use the custom made data acquisition system based on the VATA64HDR16 ASIC described in chapter 5. Besides, the SiPM matrices were changed to a new version that significantly improved several device characteristics.

The detector heads of the second prototype were assembled in Valencia and first characterization tests were carried out. Then, the system was sent to the Technical University of Munich (TUM) to carry out the tests involving 18F-fluorodeoxyglucose (FDG). These tests were an attempt to study the functioning of the prototype with FDG, check the limitations of the system and identify the problems to be solved. A proper characterization of the system was not intended.

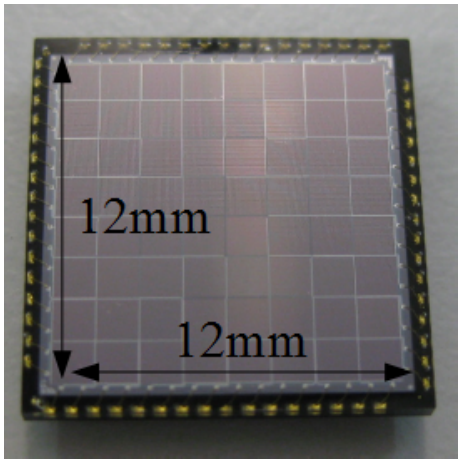

Figure 6.1: SiPM matrix from AdvanSiD model ASD-RGB1.5S-P-8x8A composed of 64 (8×8) pixels of size 1.45 mm × 1.45 mm.

6.2 Detector description

The detector heads employed in the second prototype of a small animal PET consisted of a continuous LYSO crystal coupled to a 64-pixel SiPM matrix.

6.2.1 SiPM matrices

The SiPM matrices employed in the second prototype of the small animal PET were the ASD-RGB1.5S-P-8x8A [85] from AdvanSiD [86]. The photodetector area was the same as the ones employed in the first version of the prototype, 12 mm × 12 mm. These SiPMs introduced a new manufacturing technology named RGB-SiPMs [87] that significantly improved several aspects of the SiPM matrices employed in the first prototype, such as dark count rate, photo detection efficiency, breakdown voltage uniformity and temperature stability. As the previous ones, they had 64 (8×8) pixels but the pixel size slightly changed to 1.45 mm × 1.45 mm, maintaining the 1.5 mm × 1.5 mm pitch. Each pixel had 841 microcells of 50 μm × 50 μm size. The connection to the PCB was done through a socket connector. A picture of the device can be seen in figure 6.1.

6.2.2 LYSO crystals

The scintillator crystals employed in the second prototype were the same of the first version, being LYSO crystals of 12 mm × 12 mm size with 5 mm and 10 mm

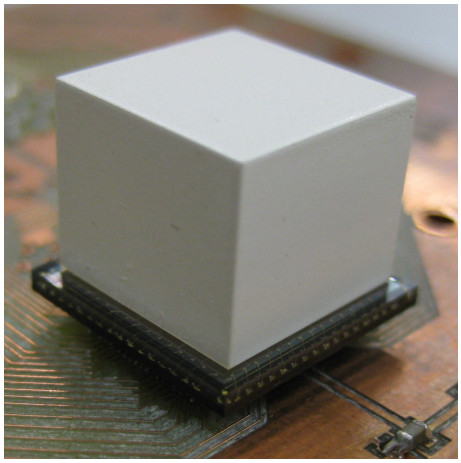

Figure 6.2: 12 $\times$ 12 $\times$ 10 mm^3 LYSO crystal placed on a RGB-SiPM matrix.

thickness painted white in five of their faces. A picture of a 10 mm thick crystal placed on a RGB-SiPM matrix can be seen in figure 6.2. Efforts were focused on using the 10 mm thick crystals because of their higher sensitivity compared to the 5 mm thick crystals due to the increase in the crystal thickness.

6.3 Readout electronics

The VATA64HDR16 ASIC from IDEAS was employed as readout electronics. A complete assessment of this ASIC can be found in chapter 5.

The charge output of the RGB-SiPMs was negative. The VATA64HDR16 ASIC was designed to work with both positive and negative input charges, but it was optimized for positive charges. In order to employ this ASIC with negative input polarity, some parameters needed to be adjusted and some features were not available. As it was shown in chapter 5, the performance of this ASIC with negative signals is limited. All measurements in this chapter were carried out with the low gain mode of the ASIC, in order to have a broader dynamic range in comparison with the high gain mode (see 5.3.1).

Each PCB containing the photodetector and the scintillator crystal was connected to another PCB hosting the VATA64HDR16 ASIC through a ribbon cable and to a data acquisition board. This approach was taken in order to allow the movement of the detector heads around the radioactive source while the electronics remained static.

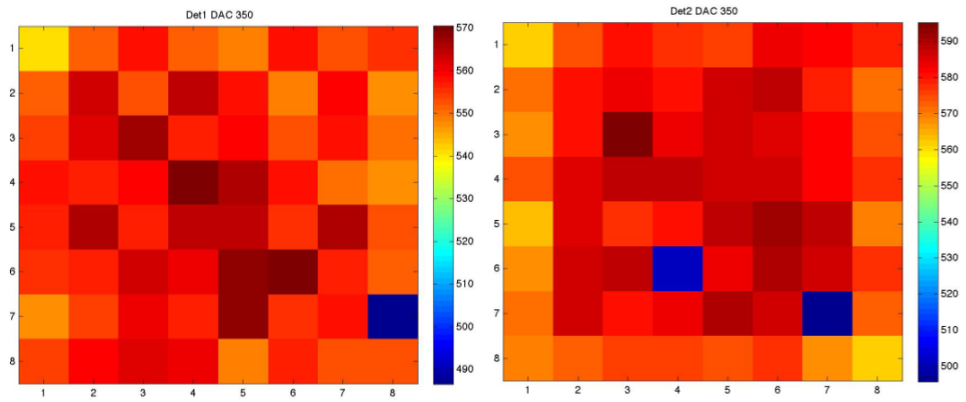

Figure 6.3: Flood map obtained for the two matrices employed in the second prototype. 6% response difference among channels.

6.4 Detector characterization

6.4.1 Uniformity

To test the uniformity of the two SiPM matrices employed in the second prototype of the small animal PET, a flood map was obtained. A piece of paper impregnated with FDG of the same size of the photodetectors (12 mm $\times$ 12 mm) was placed between them. Data were taken in both detectors in singles mode and normalized to the number of recorded events. The response difference among channels in both matrices was around 6%. The flood map obtained for both detectors can be seen in figure 6.3. The blue squares represent the channels not working in each detector.

6.4.2 Energy resolution

The energy resolution of the new RGB-SiPM matrices coupled to the 12 $\times$ 12 $\times$10 mm^3 LYSO crystals and read out by the VATA64HDR ASIC was evaluated employing a ^{22}Na source. The 511 keV photopeak was fitted with a Gaussian function and the energy resolution was calculated for each of the SiPM matrices. Almost identical results were obtained for both matrices. The ^{22}Na spectrum of one of the SiPM matrices can be seen in figure 6.4. The energy resolution obtained is 22.5% FWHM. These results were compatible with the results showed in section 5.3.5.

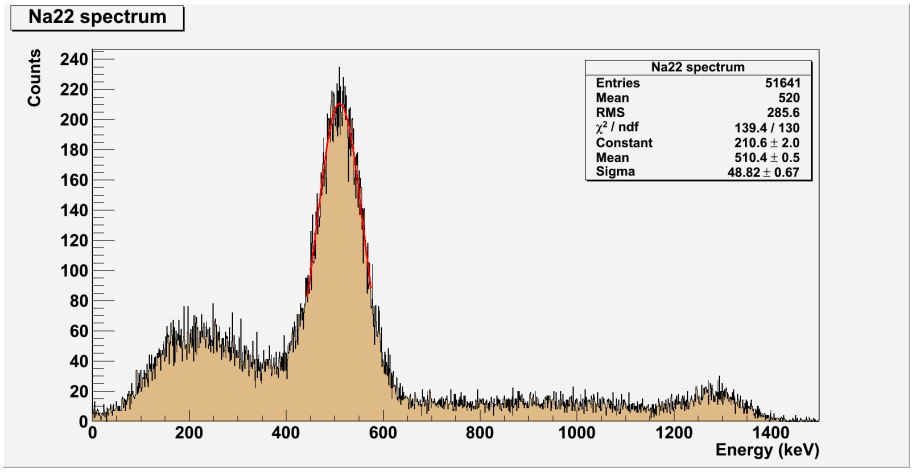

Figure 6.4: ^{22}Na spectrum obtained with a 12 $\times$ 12 $\times$ 10 mm^3 LYSO crystal coupled to a RGB-SiPM.

6.5 Coincidence tests

6.5.1 Experimental setup

The first prototype of the small animal PET was designed in order to allow the distribution of 12 detector heads, resulting in an inner diameter of 45.8 mm. This diameter was considered to be small, so the second prototype of the small animal PET was designed to host 16 detector heads, increasing its inner diameter up to 61.1 mm. This new diameter would allow to test the system with mice and rats.

The second prototype of the small animal PET consisted of two detector heads placed in front of each other and fixed to a methacrylate frame for mechanical support and alignment of the system. The frame was attached to a rotating stage MICOS DT-65N and the sources to be imaged were stationary at the center of the system in a field of view of 12 $\times$ 12 $\times$ 12 mm^3. The distance between detectors was 61.1 mm, making it possible to cover eight angular positions from 0° to 157.5° at 22.5° steps. The trigger signals generated by the two detectors were led to a custom made coincidence board. The coincidence board generated an output signal whenever the two input signals performed a logic AND. The output signal of the coincidence board was used as an external trigger and sent to the data acquisition board to record the coincidence event in each detector. A dedicated DAQ program developed in C++ controlled the rotation stage and the data acquisition of the two detectors simultaneously, and stored the digitized data from all channels of the two detectors for each coincidence event for

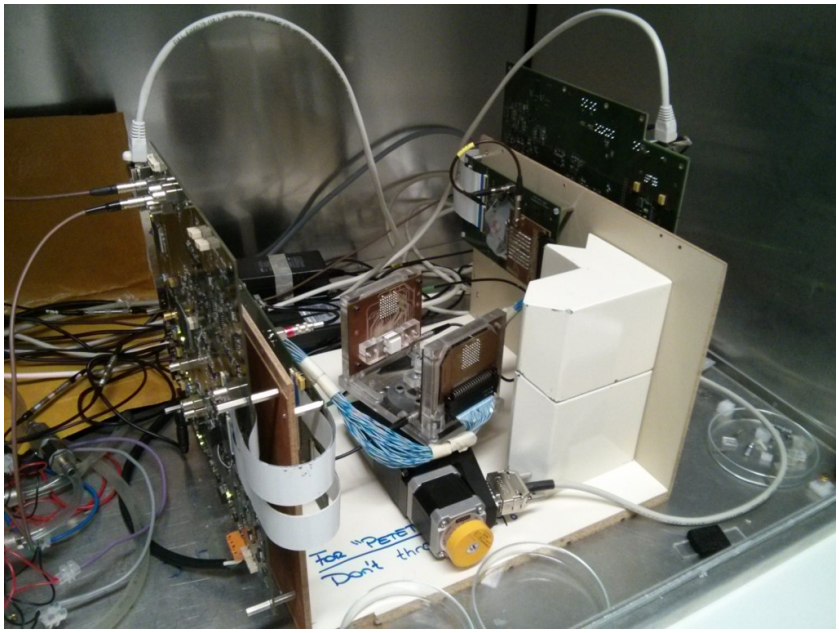

Figure 6.5: Picture of the experimental rotating system employed in the second prototype to take tomographic data at different angles.

further processing. A picture of the experimental rotating system can be seen in figure 6.5.

The algorithm employed for the image reconstruction was the MLEM explained in section 4.5.2, with the system matrix elements calculated with a Siddon-like method (SOPL). A Gaussian filter was applied to the image volumes to reduce the noise. The FOV of the reconstructed image volumes was 12 $\times$ 12 $\times$ 12 mm^3 and the image voxel was 0.1 mm^3.

6.5.2 Tests with point-like sources

Images with ^{22}Na point-like sources were obtained to test the performance of the prototype. Two point-like sources with different activities were employed for these measurements. They consisted of a plastic brick of 3 mm $\times$ 3 mm $\times$ 8 mm. The radioisotope was deposited in the center of the brick, being a cylinder of 1 mm diameter and 0.5 mm thick. The so-called ”low activity” source had 1.3 MBq and the so-called ”high activity” source had 3.4 MBq. The measurements were carried out with the 10 mm thick crystals.

To place the sources inside the field of view, a plastic holder was employed. It consisted of a column with rectangular holes of the same size as the source, with a

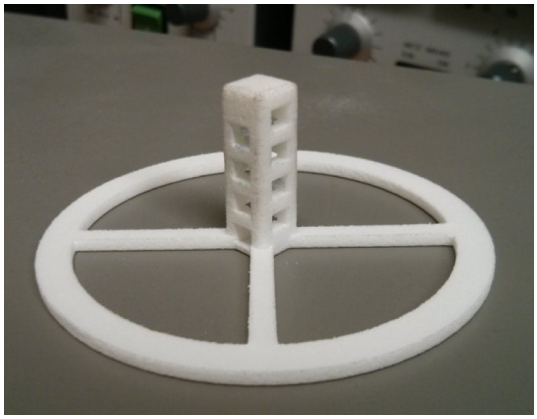

Figure 6.6: Picture of the column holder employed to place the point-like sources.

separation of 6 mm between centers of the holes. The column had holes in the two possible orientations, but they were interleaved, being 3 mm the minimum separation between active parts of the sources. A picture of the column holder can be seen in figure 6.6.

The first qualitative tests consisted in imaging both the low activity and the high activity sources. The threshold in this test was set as low as possible, just above the electronic noise. With the high activity source it was not possible to obtain good images. The best reconstructed image can be seen in figure 6.7 (top). Data were also taken with the low activity source, and the resulting image is shown in figure 6.7 (bottom). Although both sources had the same active volume, it can be qualitatively seen that the FWHM of the low activity source was better defined than the FWHM of the high activity source. We suspect that this effect was produced when the number of events to be processed exceeded a number the electronics was not capable of processing. The firmware employed in the electronics had a maximum effective readout rate of around 3500 events per second in each detector. If the number of events reaching the detectors was higher than 3500 per second, the events that the electronics was not able to process interfered with the readout and introduced noise into the measurement. Therefore, the higher the activity, the higher the number of events to be processed and consequently the distortion in the data obtained. To try to overcome this problem, a firmware programmed to support a higher readout rate was loaded into the FPGA and tested, but it resulted in making the electronics unstable. A too large amount of events to be read out was a critical limitation of the system at the time these tests were performed.

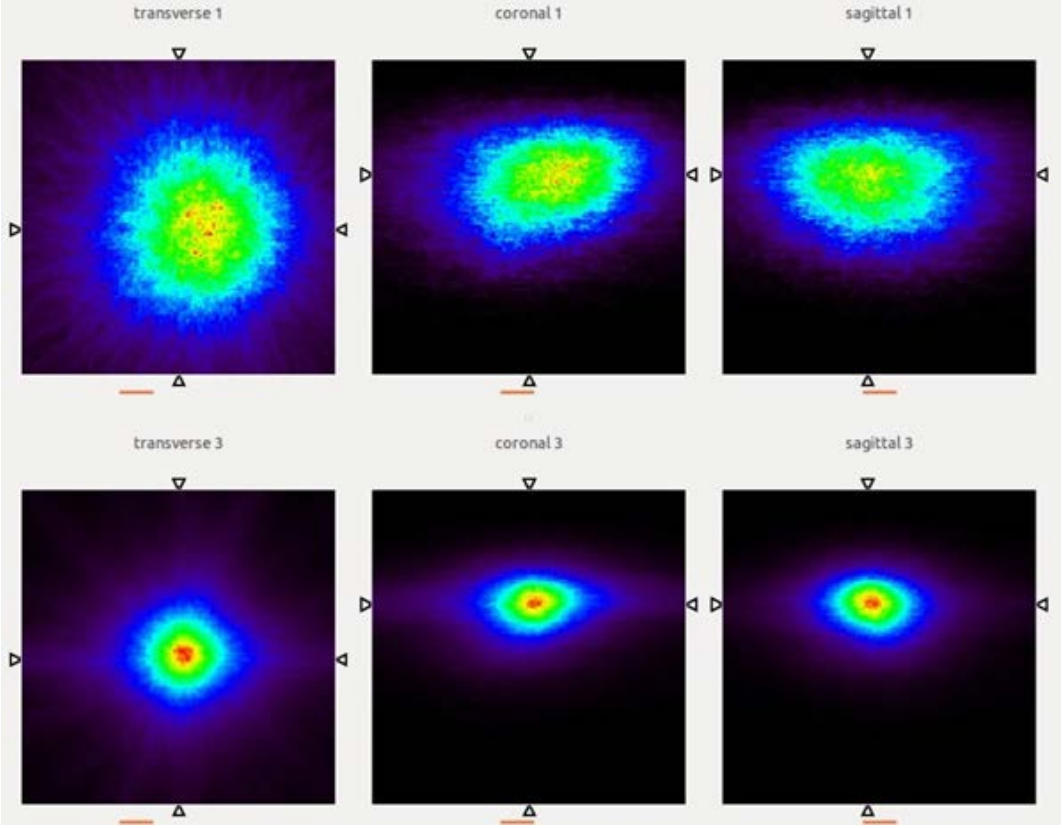

Figure 6.7: (Top) Reconstructed image of the high activity source. (Bottom) Reconstructed image of the low activity source.

Thus, in order to study the effect of varying the number of events to be read out, the influence of varying the energy threshold applied to the detectors was tested. To do so, both sources were placed in the column holder separated by a distance of 6 mm and approximately in the center of the field of view. Figure 6.8 (top) shows the reconstructed image when the same low threshold as in the previous tests was applied. As it can be seen in the figure, the two sources are indistinguishable. Then, a high threshold was set, meaning that events with energies below approximately 300 keV were electronically rejected and they were not processed. As it can be seen in figure 6.8 (bottom), the two sources were then clearly distinguishable. In PET imaging, the desirable events for the image reconstruction are the 511 keV ones to avoid detecting events scattered in the patient. Therefore, increasing the threshold up to around 300 keV is a usual practice in PET and it also contributes to reduce the number of events to be read out and therefore avoid the saturation of the electronics.

Taking into account the issues learned from the two previous tests, the low activity

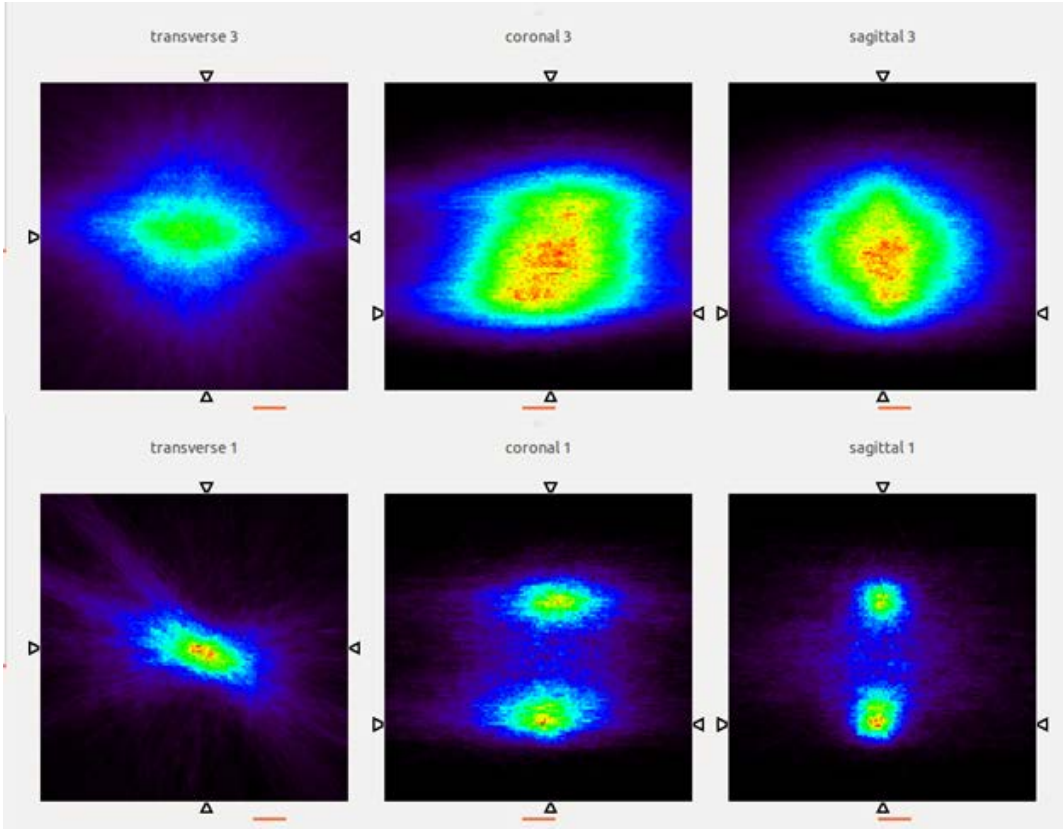

Figure 6.8: (Top) Reconstructed image of two point-like sources separated by 6 mm and employing a low threshold. (Bottom) Reconstructed image of two point-like sources separated by 6 mm and employing a high threshold.

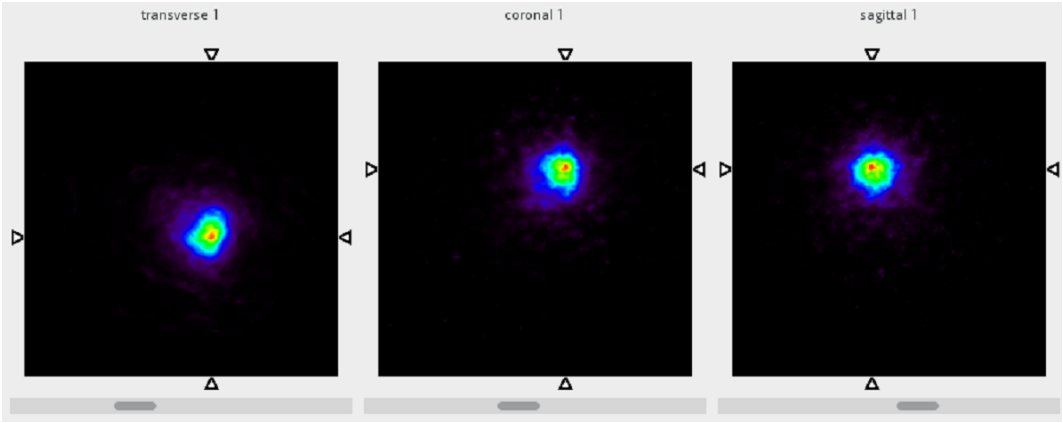

Figure 6.9: Low activity point-like source reconstructed with the MLEM algorithm, employing the 10 mm thick crystals. The FWHM obtained is 1 mm.

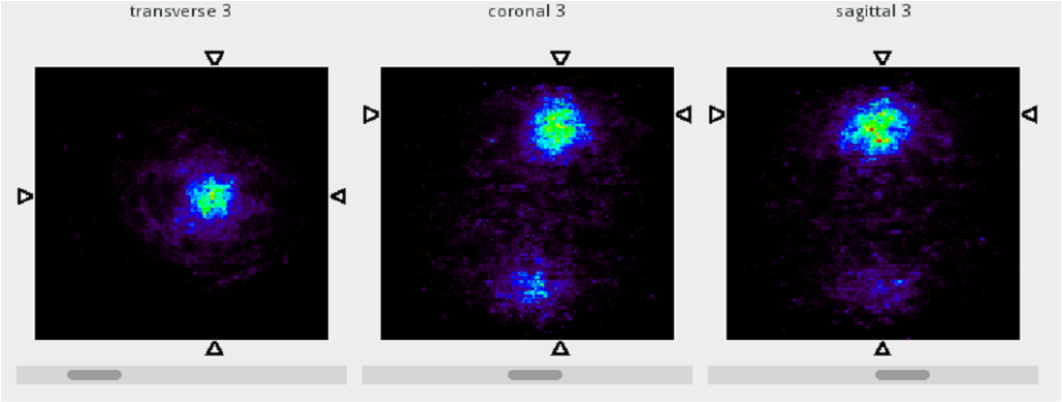

Figure 6.10: Reconstructed image of two point-like sources separated 7.5 mm. The distance between reconstructed sources was 7.3 mm and the FWHM obtained was 1.5 mm.

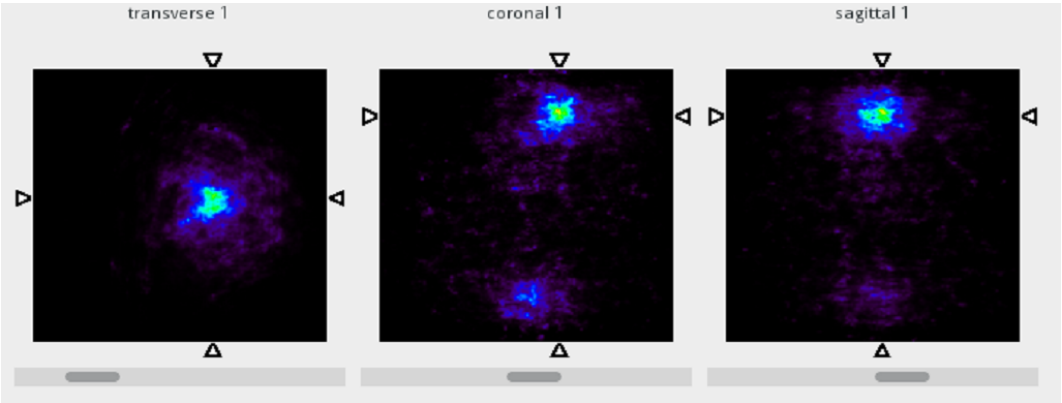

Figure 6.11: Reconstructed image of two point-like sources separated 9 mm. The distance between reconstructed sources was 8.7 mm and the FWHM obtained was 1.2 mm.

source was placed in the center of the field of view and the threshold was set high to have the lowest possible event readout rate. Figure 6.9 shows the reconstructed ^{22}Na point-like source obtained. The FWHM of the reconstructed image is 1 mm. Employing a high threshold produced a proper image, mostly probably because the electronics was not saturating.

Employing the column holder mentioned before, images with two point-like sources inside the field of view were also obtained separated at two different distances and the threshold set high. Figure 6.10 shows the reconstructed image obtained with the active part of the sources separated 7.5 mm. The distance in the image between reconstructed sources was 7.3 mm and the FWHM obtained for both sources was 1.5

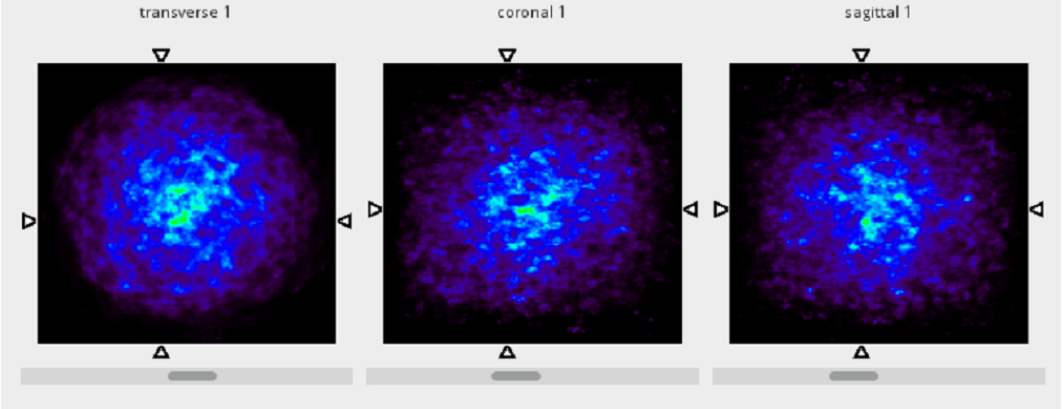

Figure 6.12: Reconstructed image of a hollow plastic cylinder of 12 mm inner diameter filled with FDG up to 12 mm.

mm. Figure 6.11 shows the reconstructed image obtained with the active part of the sources separated 9 mm. In this case, the distance between reconstructed sources was 8.7 mm and the FWHM obtained was 1.2 mm.

6.5.3 Tests with FDG

Tests employing FDG were also carried out. A hollow plastic cylinder of 12 mm inner diameter was filled with 10 MBq of FDG up to 12 mm, in order to cover the whole field of view and avoid having radioactivity outside it. The reconstructed image should be a cylinder with the radioactivity homogeneously distributed in the whole volume. The image obtained did not show cylindrical shape as it can be seen in figure 6.12. This was probably due to the high activity contained in the cylinder and therefore the saturation of the electronics, as it was explained before. Inter-pixel sensitivity correction and sensitivity matrix correction were applied, but no improvement in the images was obtained.

Measurements with a custom made phantom were also carried out. The phantom consisted of a solid plastic cylinder of 12 mm diameter with 9 holes placed in a 3 $\times$ 3 matrix. The diameter of the holes was 1.2 mm and the distance between centres was 2.4 mm in both directions. All holes were covered with tape except two in opposite corners. A first attempt to get an image with the 10 mm thick crystals was carried out since all the previous tests were performed with those crystals, but no clear image was obtained. As a test, crystals were changed to the 5 mm thick crystals and the measurement was repeated. Figure 6.13 shows the reconstructed image obtained with

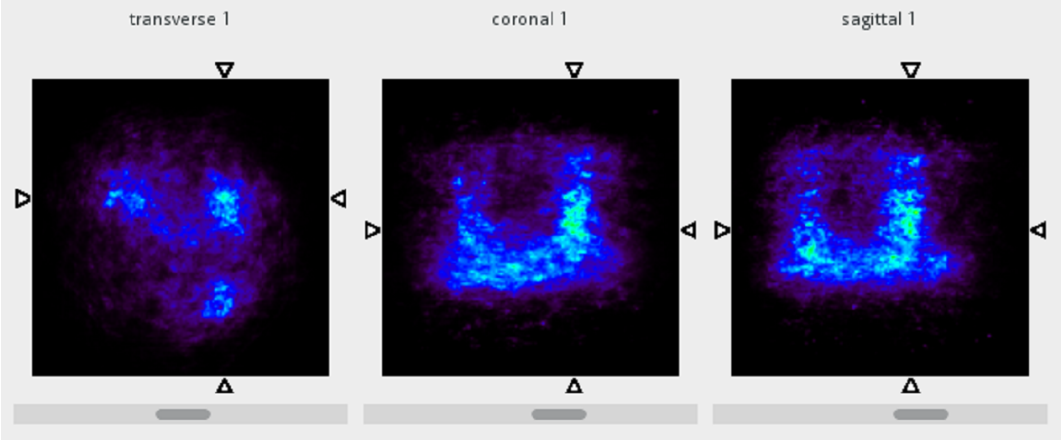

Figure 6.13: Reconstructed image of a custom made phantom filled with FDG. Three different column structures were clearly distinguishable.

the phantom and the 5 mm thick crystals. As it can be seen in the figure, the structure of the holes was distinguishable. The figure also shows three column structures instead of two, revealing that a third hole was accidentally filled with FDG.

A possible reason for this is that the position estimation determination in continuous crystals was more accurate in the case of 5 mm thick crystals due to their more favourable aspect ratio [22] and this affected the reconstruction of distributed sources more than point-like sources.

6.6 Conclusions

The second prototype of a small animal PET based on SiPMs and continuous LYSO crystals was assembled and the first images with point-like sources and FDG were obtained. The results presented in this chapter are constrained to the limited time spent at the TUM and the availability of FDG. Some tests should be carried out again with a revised version of the prototype. Nevertheless, these tests allowed to understand some of the limitations of the system in several aspects, some of which were improved, and to obtain images with FDG.

Still, further optimization of the system is needed. Although the VATA64HDR16 ASIC is capable of working with positive and negative signals, the use of SiPMs with negative polarity limits the ASIC performance, as it was shown in section 5.3.1. The use of matrices with positive polarity is foreseen in a future version of the system.

Summary and conclusions

The progress in the development of SiPMs in recent years has made them suitable candidates to replace traditional PMTs in medical physics applications. Coupled to continuous crystals, it is possible to improve spatial resolution and sensitivity at the same time, as well as to reduce the cost of the block detector.

The work presented in this thesis was initiated when the use of SiPMs was starting and it describes the first developments carried out in the IRIS group related to the use of continuous crystals and SiPMs for two medical physics applications: a Compton telescope for hadron therapy monitoring and a small animal PET.

The detector developed for the hadron therapy application was the necessary first step to test the detector concept towards the development of a Compton telescope, since SiPMs are essential in its design. It allowed us to evaluate the technology based on continuous $LaBr_3$ crystals and SiPMs and its application in a functioning Compton camera. At the time the tests carried out began, SiPMs were a new technology and the manufacturing process was not mature enough. The main problems were the lack of homogeneity among elements in a SiPM matrix and the high dark count rate. Besides, $LaBr_3$ was a relatively new scintillator crystal with characteristics that made it appropriate for the application. The detector was fully characterized and coincidence tests were carried out. Images were successfully reconstructed with the device. These results demonstrated the feasibility of operating the system and led to the development of a three-layer telescope with detectors four times bigger, which is still ongoing.

The other application, which was the main part of the work developed, was the first prototype of a small animal PET. The detectors were fully characterized and coincidence tests between two detector heads were carried out. Tomographic images of point-like sources were obtained with a FWHM close to 1 mm. Simulations of novel geometries, mainly tapered crystal, were performed in order to assess the possibility of employing such geometries in future versions of the prototype.

In both Compton telescope and small animal PET applications, improved readout electronics were needed due to the foreseen increase in the number of readout channels of the new prototypes. A simple and cost effective approach was to develop a versatile DAQ system employing the same ASIC for both applications. This approach allowed us to unify both research lines and to carry out the developments within our research group. The VATA64HDR16 ASIC was chosen for several reasons: it had a large enough number of channels, it was capable of working with both positive and negative input signals and it allowed to adjust the bias for each channel independently. Besides, the research group had previous experience with other chips of the same family for other applications and a DAQ board previously developed by the group could be adapted to operate this ASIC. Tests were carried out to assess the suitability of the VATA64HDR16 ASIC for our applications. Based on the results obtained, the performance of the ASIC was not optimum, but it fulfilled our needs.

The VATA64HDR16 ASIC was employed in a second version of the prototype of a small animal PET. The main differences with the first prototype were the use of this ASIC as readout electronics and the change of the SiPM matrices to a new version that significantly improved several device characteristics. Images of point-like sources and preliminary images of a custom made phantom filled with FDG were obtained. Those tests allowed us to understand the limitations of the system in several aspects. The prototype was a successful proof-of-concept of the proposed technology and the development of a full-ring PET based on it is underway with the aim of comparing its performance with commercial preclinical scanners.

The results obtained within this thesis assess the possibility of employing the proposed technology in the detector concepts tested from a technical point of view and have led to significant advances in the field. The use of continuous crystals coupled to SiPMs, with some additional efforts to achieve the stability and reproducibility requirements for commercialization, can constitute an effective way of enhancing spatial resolution and efficiency while reducing detector cost.

The tests carried out also show that the development of ASICs that appropriately address the specific requirements of continuous crystals is mandatory to achieve an optimal performance.

From the point of view of the applications, the requirements of PET are less stringent and it is better suited for the use of this technology. Its application to Compton cameras for nuclear imaging, homeland security or astroparticle physics can also be

advantageous. In the case of hadron therapy monitoring, other requisites such as large dynamic range or detector occupancy must also be carefully evaluated.

In conclusion, the development of this work has been essential to evaluate technologies and detector concepts that were being tested by a restricted number of groups at that point and that now have increased interest in the field with the contribution of the work carried out in this thesis. The results obtained in this work have given a strong experimental support to the research lines followed by the group and will lead to further developments and improvements along these line in the future.

Resumen en castellano

El trabajo presentado en esta tesis introduce y evalúa dos aspectos novedosos en los detectores de rayos gamma para imagen médica: el uso de fotomultiplicadores de silicio (SiPMs, en inglés) acoplados a cristales centelleadores continuos.

Tradicionalmente, los tubos fotomultiplicadores (PMTs, en inglés) acoplados a cristales centelleadores han jugado un papel dominante en la detección de rayos gamma. En los últimos años ha aparecido un nuevo tipo de fotodetector de estado sólido, el SiPM, como opción para sustituir a los PMTs en ciertas aplicaciones. Los SiPMs tienen una ganancia y una eficiencia cuántica altas, un voltaje de operación bajo y unas propiedades temporales excelentes. Además, son dispositivos muy compactos e insensibles a los campos magnéticos. Estas propiedades hacen de los SiPMs un excelente candidato para usarlos en aplicaciones de física médica.

Normalmente, la detección de los rayos gamma se lleva a cabo utilizando detectores basados en cristales centelleadores pixelados acoplados a un fotodetector segmentado porque ofrecen una manera sencilla de identificar el lugar donde ha tenido lugar la interacción. Sin embargo, en esta configuración la mejora de la resolución espacial implica la reducción de la sensibilidad, y al revés. El uso de cristales centelleadores continuos acoplados a fotodetectores segmentados podría aumentar la resolución espacial y la sensibilidad al mismo tiempo, además de reducir el coste del bloque detector.

Este trabajo aquí presentado se desarrolló en el grupo IRIS (*Image Reconstruction, Instrumentation and Simulations for medical applications*) del IFIC-Valencia. Se inició cuando el uso de los SiPMs estaba empezando y llevó a desarrollos importantes. En esta tesis, se han probado diferentes tipos de cristales centelleadores continuos acoplados a SiPMs de varios fabricantes para demostrar la viabilidad de esta tecnología en el desarrollo de nuevos conceptos de detector y aplicaciones en física médica. La mayor parte de la tesis trata el desarrollo de un prototipo PET para animales pequeños

basado en cristales centelleadores continuos de LYSO y SiPMs. Además, también se presentan las primeras pruebas de un telescopio Compton basado en SiPMs y cristales centelleadores continuos de $LaBr_3$ para la monitorización del tratamiento en terapia hadrónica.

Imagen médica

La imagen médica es el conjunto de técnicas que de forma no invasiva son capaces de producir imágenes de las estructuras internas de un cuerpo. Sus principales modalidades incluyen la imagen por rayos X, imagen por tomografía computarizada (CT), imagen por resonancia magnética (MRI), imagen por ultrasonidos e imagen por medicina nuclear.

La medicina nuclear es la rama de la medicina que hace uso de radiotrazadores para el diagnóstico y el tratamiento de enfermedades. En medicina nuclear se utilizan principalmente dos clases de radiotrazadores: los emisores de un sólo fotón y los emisores de positrones. Los emisores de un sólo fotón emiten principalmente un rayo gamma o una secuencia de rayos gamma que no están correlacionados direccionalmente. Los emisores de positrones emiten un positrón que viaja una corta distancia antes de aniquilarse con un electrón, su antipartícula, generando dos fotones de 511 keV que viajan en direcciones casi opuestas.

En esta tesis, se describe el desarrollo de nuevos detectores para medicina nuclear, en concreto para una aplicación de imagen Compton (una variedad de SPECT) y otra para PET.

El SPECT hace uso de emisores de un solo fotón y para su detección emplea colimadores mecánicos, lo que provoca que la resolución espacial y la eficiencia de detección estén inversamente relacionadas. La imagen Compton supera esta limitación sustituyendo los colimadores mecánicos por una serie de planos de detección trabajando en coincidencia temporal, lo que se conoce como colimación electrónica. El rayo gamma interacciona en un primer detector por efecto Compton, cediendo parte de su energía y cambiando su dirección de propagación e interacciona de nuevo en un segundo detector. Haciendo uso de la cinemática Compton, es posible determinar el origen de los rayos gamma.

Por su parte, el PET emplea emisores de positrones y se basa en la detección simultánea de los dos fotones de 511 keV generados tras la aniquilación del positrón con un electrón. Para ello, se suele utilizar un anillo de detectores trabajando en

coincidencia temporal que se dispone alrededor del lugar del cual se quiere obtener la distribución del radiotrazador.

Detectores para imagen médica

Tanto para la aplicacion de imagen Compton como para la de PET, se han usado detectores basados en cristales centelleadores continuos y SiPMs.

Los dos cristales centelleadores que se emplean en esta tesis son el *LaBr*$_3$ (Bromuro de Lantano (III)) y el *LYSO* (Lutecio Ytrio Ortosilicato, $Lu_{1.8}Y_{0.2}SiO_5$). El $LaBr_3$ es un cristal centelleador relativamente nuevo. Tiene una producción de luz muy alta, un tiempo de decaimiento muy bajo y una resolución energética excelente. Comparado con otros cristales centelleadores y debido a su bajo número atómico efectivo (Z_{eff}), el $LaBr_3$ presenta una probabilidad de fotoabsorción más baja y una probabilidad Compton más alta. La principal desventaja del $LaBr_3$ es su higroscopicidad, lo que hace que requiera de un alojamiento hermético y manipularlo con cuidado. Por su parte, el LYSO se emplea en escáneres PET. Tiene una eficiencia de detección alta, una producción de luz alta y un tiempo de decaimiento bajo. No es higroscópico y muestra buenas propiedas mecánicas. Su principal desventaja es la presencia del isótopo ^{176}Lu en su composición, con una vida media de 4×10^{10} años.

Los SiPMs son unos detectores que transforman la luz de centelleo que llega a su superficie proveniente del cristal centelleador en una señal eléctrica. Están formados por una matriz de microceldillas sensibles a la luz conectadas en paralelo. Cada microceldilla es un diodo de avalancha (APD) funcionando en modo Geiger que detecta fotones de manera idéntica e independiente. De esta manera, la amplitud de la señal de salida de un SiPM corresponde con la suma de la señal de todas las microceldillas activadas y es proporcional a la cantidad de fotones que interaccionan en su superficie.

Detector basado en SiPMs y cristales continuos de $LaBr_3$ para un telescopio Compton

La terapia hadrónica es una técnica para el tratamiento del cáncer basada en la irradiación de los tumores con iones ligeros, normalmente protones o iones de carbono. Durante el tratamiento, las partículas del haz excitan los núcleos de los tejidos del paciente y se emiten partículas secundarias. En el proceso de desexcitación nuclear

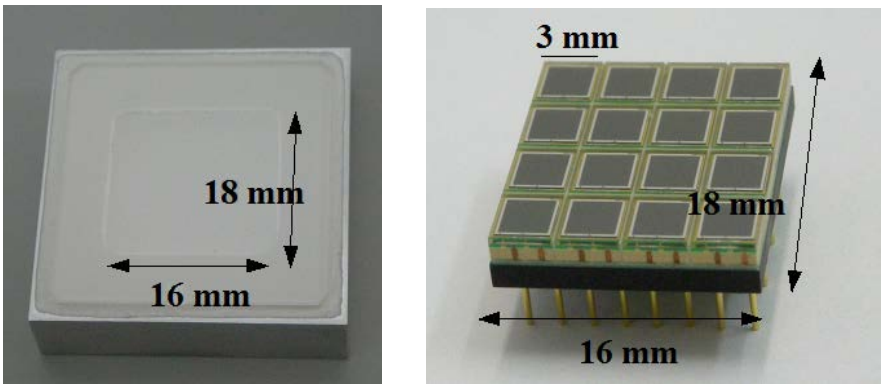

(a) (b)

Figure 1: (a) Imagen del cristal de $LaBr_3$ de tamaño 16 mm $\times$ 18 mm $\times$ 5 mm. (b) Array de MPPCs fabricado por Hamamatsu modelo S11064-050P compuesto por 16 (4 $\times$ 4) píxeles de 3 $\times$ 3 mm^2.

se emiten fotones en un espectro característico, siendo más abundantes en las energías comprendidas entre 1 y 7 MeV [23]. La producción de estos fotones está correlacionada con la dosis absorbida y además tiene lugar a los pocos nanosegundos de la irradiación [24, 25], por lo que su detección se puede usar para monitorizar el tratamiento en tiempo real.

Un telescopio Compton se podría usar para localizar el origen de los fotones emitidos durante el tratamiento con terapia hadrónica. El grupo IRIS, dentro del proyecto europeo ENVISION, desarrolló un primer prototipo de un detector basado en cristales centelleadores continuos de $LaBr_3$ acoplados a SiPMs para su uso en un telescopio Compton.

El detector estaba compuesto por un cristal continuo de $LaBr_3$ de tamaño 16 mm $\times$ 18 mm $\times$ 5 mm (figura 1 (a)) acoplado a una matriz de SiPMs, en este caso un array de MPPCs fabricado por Hamamatsu modelo S11064-050P de la misma superficie y compuesto por 16 (4 $\times$ 4) píxeles de 3 $\times$ 3 mm^2 (figura 1 (b)).

La electrónica de lectura empleada fue el ASIC SPIROC1 [35]. El detector mostraba un comportamiento lineal hasta los 1275 keV. La resolución energética obtenida fue del 7% FWHM a 511 keV y mejoraba hasta el 6.5% FWHM si se ecualizaba la respuesta de todos los píxeles del array del MPPC. La resolución temporal fue de 3.1 ns si se empleaba la señal suma de la salida del detector. La resolución espacial obtenida en toda la superficie del cristal fue de 0.7 mm FWHM.

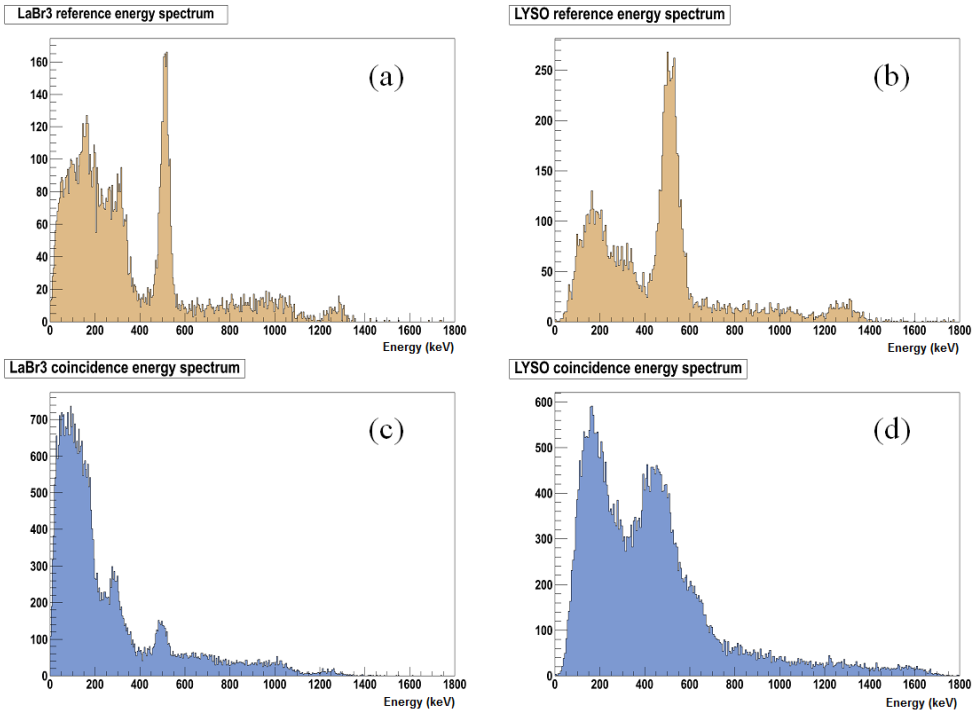

Figure 2: Espectros energéticos de referencia para los cristales de $LaBr_3$ (a) y de LYSO (b). Espectros energéticos en coincidencia temporal de $LaBr_3$ (c) y de LYSO (d).

Para evaluar el rendimiento del detector en modo telescopio, se llevaron a cabo pruebas añadiendo un segundo plano de detección detrás del que se acaba de describir, trabajando ambos en coincidencia temporal. El segundo plano estaba compuesto por un cristal de LYSO de 12 mm $\times$ 12 mm $\times$ 5 mm acoplado al mismo modelo de array de MPPCs, de manera que el cristal cubría 9 de los 16 píxeles.

Para estas pruebas, se usó una fuente de ^{22}Na colocada delante del primer detector, donde los fotones sufrían dispersión Compton y después, en el segundo detector, interaccionaban a través de otra dispersión Compton o por fotoabsorción.

La figura 2 corresponde a los espectros energéticos obtenidos sin coincidencia temporal con el $LaBr_3$ (a) y con el LYSO (b), los cuales se usaron como referencia y para realizar la calibración energética. La figura también muestra los espectros energéticos obtenidos trabajando en coincidencia temporal con el $LaBr_3$ (c) y con el LYSO (d). La figura 3 muestra la suma de las energías recogidas en los dos detectors, recuperando el espectro de ^{22}Na.

Con este prototipo también se obtuvieron imágenes de fuentes puntuales y fueron publicadas en [38]. Los resultados obtenidos demostraron la viabilidad de operar

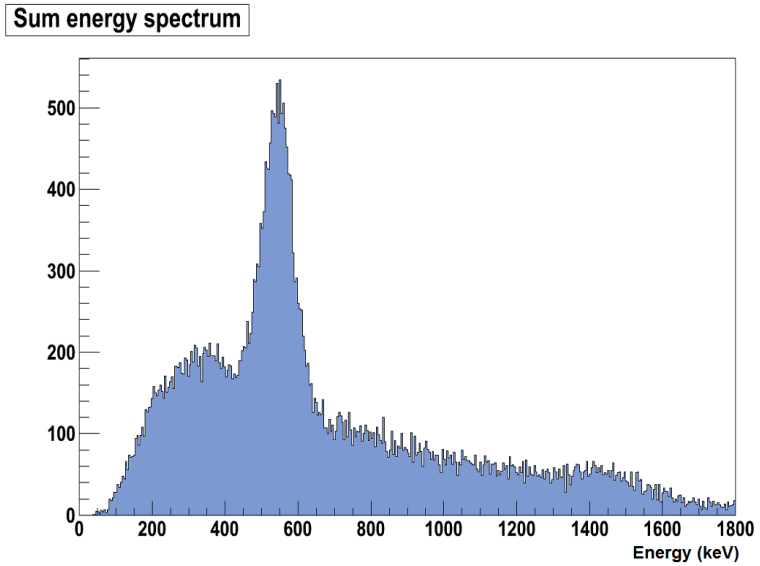

Figure 3: Espectro suma obtenido con ambos detectores en coincidencia temporal.

el sistema y condujeron a una segunda versión del prototipo que consistía en un telescopio de tres capas con detectores cuatro veces más grandes [39]. El aumento en el número de canales a procesar hizo necesario cambiar la electrónica de lectura al ASIC VATA64HDR16. El rendimiento de este segundo prototipo se probó en haz y los resultados se publicaron en [40].

El autor de esta tesis se encuentra actualmente trabajando en la tercera versión del telescopio Compton. Los arrays de MPPCs se van a actualizar al último modelo disponible de Hamamatsu (S13361-3050AE-08), los cuales mejoran varias especificaciones. Además, se está investigando la idoneidad del $CeBr_3$ para esta aplicación.

Primer prototipo de un PET para animales pequeños basado en SiPMs y cristales continuos de LYSO

En un escáner PET, los dos principales parámetros que hay que maximizar son la sensibilidad y la resolución espacial. El uso de cristales centelleadores continuos acoplados a SiPMs puede mejorar al mismo tiempo ambas magnitudes.

Para probar esta tecnología, se desarrolló un detector basado en un cristal centelleador continuo de LYSO de tamaño 12 mm $\times$ 12 mm $\times$ 5 mm acoplado a una matriz monolítica de SiPMs de la misma superficie desarrollada en el FBK-irst y compuesta por 64 elementos distribuidos en 8 $\times$ 8 píxeles. Cada píxel tenía un tamaño de 1.5 $\times$

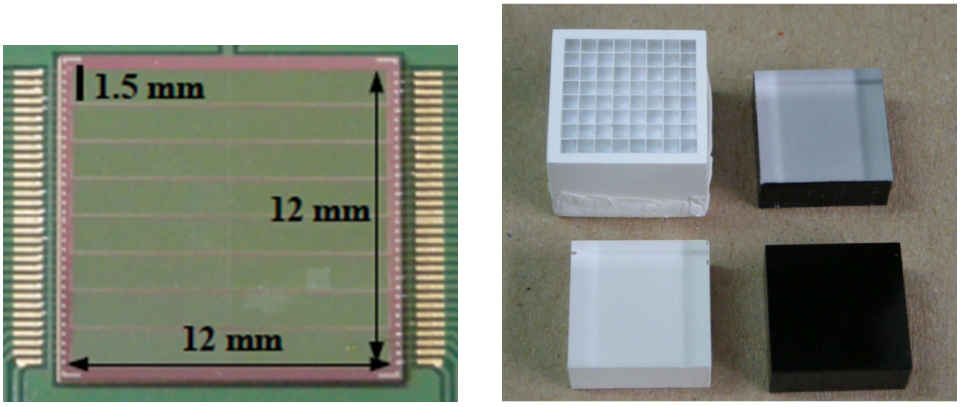

(a) (b)

Figure 4: (a) Matriz monolítica de SiPMs desarrollada en el FBK-irst compuesta por 64 elementos (8 $\times$ 8) de 1.5 $\times$ 1.4 mm^2. (b) Cristales empleados en las pruebas. Superior izquierda: array de cristales. Superior derecha: cristal blanquinegro. Inferior izquierda: cristal blanco. Inferior derecha: cristal negro.

1.4 mm^2 con un pitch de 1.5 mm en las dos direcciones (figura 4 (a)).

La electrónica de lectura empleada fue el ASIC MAROC2 [61]. Se hicieron pruebas con cristales centelleadores pintados de distintos modos para evaluar su rendimiento: blanco, negro y blanquinegro (figura 4 (b)). El cristal blanco fue el que mejores resultados ofreció, con un comportamiento lineal hasta los 1275 keV, una resolución energética del 15% FWHM a 511 keV, una resolución temporal de 6 ns FWHM y una resolución espacial de 0.7 mm FWHM. El algoritmo de determinación de la posición empleado demostró que era capaz de reconstruir la posición de interacción con una resolución espacial mejor que un milímetro, incluso cerca de los bordes del cristal y sin necesidad de calibración previa.

Para obtener imágenes tomográficas, se montaron dos detectores con los cristales blancos enfrentados a una distancia de 45.8 mm, unidos entre sí a través de un soporte de metacrilato, el cual giraba solidariamente junto con una mesa de rotación, de manera que cubrían seis posiciones angulares desde 0° a 150° en pasos de 30°.

La figura 5 muestra la imagen reconstruida de una fuente de ^{22}Na obtenida con los cristales continuos blancos de 5 mm de grosor. La FWHM promedio de las dos dimensiones fue de 0.9 mm. Algunas medidas se repitieron con cristales continuos blancos de 10 mm de grosor.

También se llevaron a cabo simulaciones con GEANT4 que incluían la generación

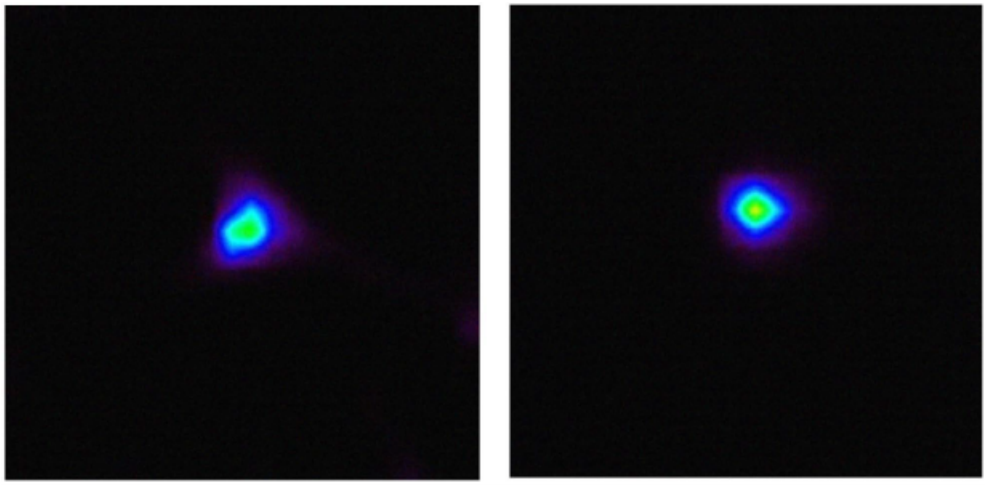

Figure 5: Vista transaxial (izquierda) y sagital (derecha) de una fuente puntual reconstruida con los cristales centelleadores blancos. La FWHM obtenida fue 0.9 mm de media.

y el transporte de fotones ópticos. Una vez se tuvo una simulación válida para cristales cuboides, se simularon cristales trapezoidales para reducir con ellos el espacio entre detectores y de esa manera aumentar la sensibilidad en un anillo completo [67]. Además, también se consideró colocar el fotodetector en la superficie de entrada del cristal, lo que se espera que mejore el rendimiento [72].

La figura 6 muestra las geometrías trapezoidales que se simularon para cristales de 5 y 10 mm de espesor. Los resultados de las simulaciones se compararon con datos reales, principalmente en términos de distribución de la luz y de determinación de la posición en el cristal. Los resultados obtenidos con las simulaciones de cristales trapezoidales mostraron una distribución de la luz distinta para cada geometría, como era de esperar, reproduciendo los datos experimentales. Esto demostró que la simulación se podía usar con cristales trapezoidales. Sin embargo, el algoritmo de determinación de la posición que se empleó era el mismo que se había desarrollado para cristales cuboides y no estaba adaptado para las particularidades geométricas de los cristales trapezoidales.

Los resultados obtenidos con este primer prototipo de PET para animales pequeños fueron prometedores, lo que motivó el desarrollo de una segunda versión del prototipo. La idea de crear un anillo completo de detectores hizo necesario considerar nuevas electrónicas de lectura, siendo el ASIC VATA64HDR16 la opción escogida.

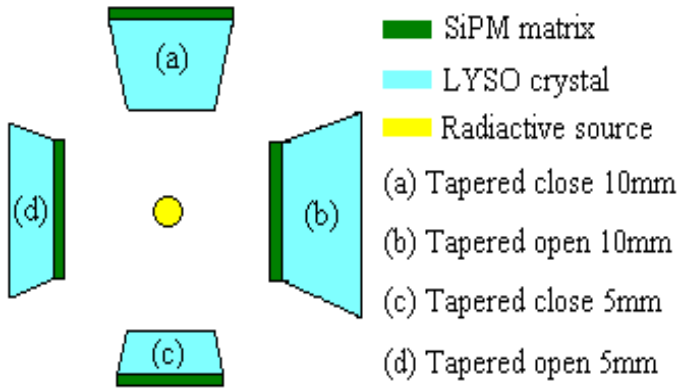

Figure 6: Geometrías de cristales trapezoidales que fueron simuladas.

Rendimiento del ASIC VATA64HDR16 para aplicaciones de física médica basadas en cristales continuos y SiPMs

Tanto la aplicación de terapia hadrónica como la de PET alcanzaron un punto en el que la electrónica de lectura que se empleaba en los detectors necesitó aumentar el número de canales. En esta situación, la solución fue desarrollar un sistema de adquisición de datos (DAQ) que usase el mismo ASIC para las dos aplicaciones. Esto permitía unificar las dos líneas de investigación y continuar con los desarrollos dentro del grupo de investigación. El principal problema era que la aplicación para terapia hadrónica hacía uso de arrays de MPPCs con una polaridad de salida positiva, mientras que la aplicación para PET empleaba matrices de SiPMs con una polaridad de salida negativa.

El ASIC VATA64HDR16 se escogió por varias razones: tenía un número de canales lo suficientemente amplio, era capaz de trabajar con señales de entrada positivas y negativas y permitía ajustar el voltaje de operación de cada canal de forma independiente. Además, el grupo IRIS tenía experiencia con otros chips de la misma familia para otras aplicaciones y previamente había desarrollado una tarjeta de adquisición que se podía adaptar para controlar este ASIC.

Para las pruebas se usó un array de MPPCs de Hamamatsu modelo S11064-050P compuesto por 16 (4×4) píxeles de 3×3 mm^2 acoplado a cristales de LYSO y de $LaBr_3$ de 16 mm $\times$ 18 mm $\times$ 5 mm. La particularidad de este modelo de MPPC es que el ánodo y el cátodo son independientes, por lo que dependiendo del esquema

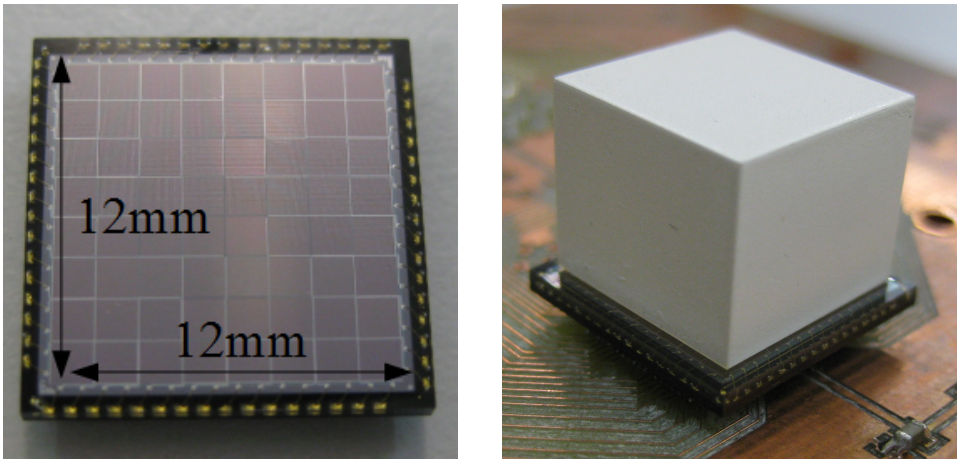

(a) (b)

Figure 7: (a) Matriz de SiPMs AdvanSiD ASD-RGB1.5S-P-8x8A compuesta de 64 píxeles (8 $\times$ 8) de tamaño 1.45 mm $\times$ 1.45 mm. (b) Cristal de LYSO pintado de blanco de 12 mm $\times$ 12 mm $\times$ 10 mm colocado sobre una matriz de SiPMs.

de alimentación, se pueden conseguir señales de salida positivas o negativas y así evaluar el rendimiento del ASIC para cada una de ellas.

Se llevaron a cabo pruebas de rango dinámico, de resolución temporal, de ecualización de la respuesta del detector, de selección del tiempo de retardo a la retención y estudios de resolución energética [79]. Las pruebas llevadas a cabo permitieron comprobar que el rendimiento de este ASIC para señales negativas era limitado y que estaba optimizado para señales positivas. Además, su respuesta temporal mostraba una fuerte dependencia de la amplitud de la señal de entrada (*timewalk*). Aunque el rendimiento del ASIC VATA64HDR16 no era óptimo, cumplía con los requisitos para nuestras aplicaciones.

Segundo prototipo de un PET para animales pequeños basado en SiPMs y cristales continuos de LYSO

Basado en los resultados obtenidos con el primer prototipo, se desarrolló un segundo prototipo de PET para animales pequeños con el objetivo de hacerlo escalable a una geometría de anillo completo. Las principales diferencias fueron el uso del ASIC VATA64HDR16 como electrónica de lectura y la sustitución de las matrices de SiPMs por una nueva versión que mejoraba significatimente varios parámetros del fotodetector.

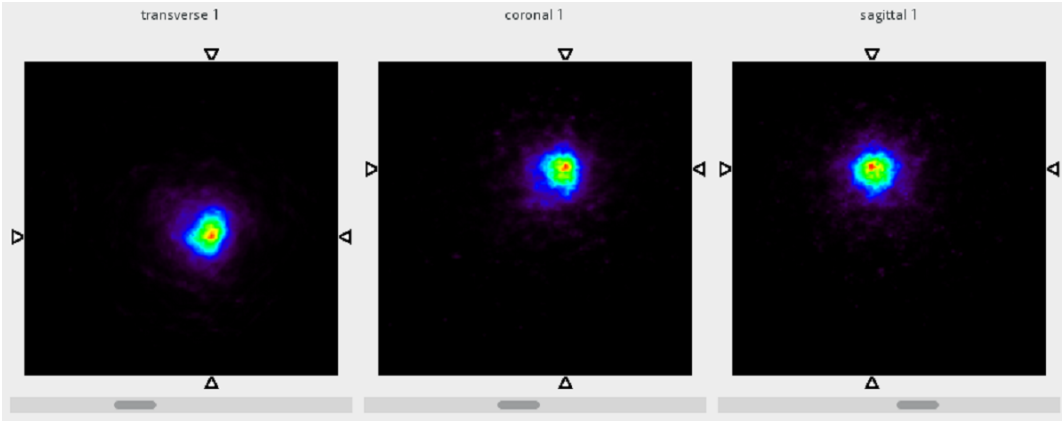

Figure 8: Fuente puntual de baja actividad reconstruida con los cristales de LYSO de 10 mm de espesor. La FWHM obtenida fue de 1 mm.

Las matrices de SiPMs se cambiaron por las AdvanSiD ASD-RGB1.5S-P-8x8A que estaban compuestas de 64 píxeles (8 $\times$ 8) de tamaño 1.45 $\times$ 1.45 mm^2 (figura 7 (a)). Los cristales centelleadores continuos empleados eran de LYSO pintados de blanco y tenían unas dimensiones de 12 mm $\times$ 12 mm $\times$ 10 mm (figura 7 (b)).

Los detectores se ensamblaron en el IFIC-Valencia y se realizaron las primeras pruebas de caracterización. Después, el sistema se envió a la Universidad Técnica de Múnich (TUM) para probarlo con fuentes puntuales y FDG.

Para obtener imágenes tomográficas, se montaron dos detectores con los cristales blancos enfrentados. Se aumentó la distancia a 61.1 mm, de manera que cubrían ocho posiciones angulares desde 0° a 157.5° en pasos de 22.5°.

Las pruebas realizadas permitieron unas condiciones aceptables para la obtención de imágenes. La figura 8 muestra la imagen reconstruida de una fuente puntual de ^{22}Na obtenida con los cristales continuos blancos de 10 mm de grosor. La FWHM obtenida fue de 1 mm.

Una vez se obtuvieron imágenes con fuentes puntuales, se pasó a pruebas con FDG y un fantoma que consistía en un cilindro de metacrilato de 12 mm de diámetro con 9 agujeros dispuestos en una matriz de 3 $\times$ 3. El diámetro de los agujeros era de 1.2 mm y la distancia entre centros de 2.4 mm en ambas direcciones. Se taparon todos los agujeros menos dos, situados en esquinas opuestas, que se llenaron con FDG. No se consiguió obtener ninguna imagen del fantoma con los cristales de 10 mm de grosor. Se cambiaron los cristales por los de 5 mm de grosor y se repitió la prueba. La figura 9 muestra el resultado obtenido, donde se distingue la estructura de

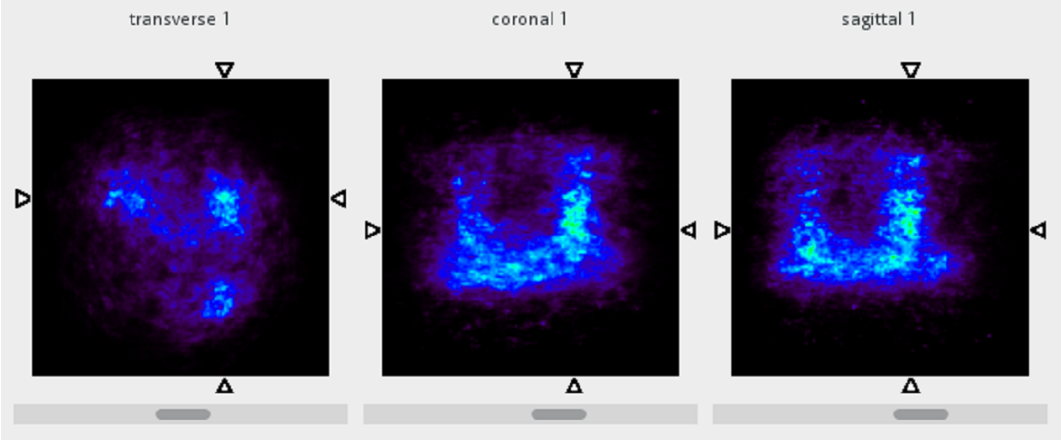

Figure 9: Imagen reconstruida de un fantoma relleno de FDG. Tres columnas se distinguen claramente.

los agujeros llenos con FDG. La figura también muestra que una tercera columna se había llenado de FDG de forma no intencionada.

Los resultados aquí mostrados están limitados por el tiempo que se pasó en la TUM y la disponibilidad de FDG. Las pruebas con FDG fueron un intento de estudiar el funcionamiento del prototipo con fuentes líquidas, comprobar las limitaciones del sistema e identificar los problemas a resolver. El uso de matrices con señales de salida negativas limitaba mucho el rendimiento del ASIC VATA64HDR16. Por ello, se prevé utilizar matrices con señales de salida positivas en una futura versión del sistema. Ademas, se ha mejorado el algoritmo de estimación de la posición para cristales de 10 mm de grosor [22].

Conclusiones

El detector basado en cristales continuos de $LaBr_3$ y SiPMs fue el primer paso necesario para el desarrolo de un telescopio Compton. Permitió evaluar la tecnología basada en cristales continuos de $LaBr_3$ y SiPMs y su aplicación en una cámara Compton funcional. El $LaBr_3$ era un cristal centelleador relativamente nuevo con unas características que lo hacían indicado para la aplicación. El uso conjunto de ambos componentes permitió comprobar que la tecnología propuesta era adecuada para un telescopio Compton. Los buenos resultados obtenidos condujeron a continuar con el desarrollo del prototipo, que todavía sigue su curso.

Por su parte, los dos prototipos de PET para animales pequeños fueron una

exitosa prueba de concepto de la tecnología basada en cristales continuos de LYSO y SiPMs. Las imágenes obtenidas mostraron resultados con una FWHM cercana a 1 mm. Las pruebas realizadas sirvieron para entender las limitaciones del sistema en muchos aspectos y la intención es desarrollar un anillo completo que permita comparar su rendimiento con el de escáneres preclínicos comerciales.

References

[1] W. R. Leo. *Techniques for Nuclear and Particle Physics Experiments: A How to Approach*. 1987. 5

[2] M. Singh. AN ELECTRONICALLY COLLIMATED GAMMA CAMERA FOR SINGLE PHOTON EMISSION COMPUTED TOMOGRAPHY. PART 1. *Journal of Computer Assisted Tomography*, 7(6):1135, dec 1983. 7

[3] J.W. LeBlanc, N.H. Clinthorne, C.-H. Hua, E. Nygard, W.L. Rogers, D.K. Wehe, P. Weilhammer, and S.J. Wilderman. C-SPRINT: a prototype compton camera system for low energy gamma ray imaging. *IEEE Trans. Nucl. Sci.*, 45(3):943–949, jun 1998. 7

[4] Gabriela Llosa, JosÉ Bernabeu, Don Burdette, Enrico Chesi, Neal H. Clinthorne, Klaus Honscheid, Harris Kagan, Carlos Lacasta, Marko Mikuz, Pablo Modesto, W. Leslie Rogers, Andrej Studen, and Peter Weilhammer. Last results of a first compton probe demonstrator. *IEEE Trans. Nucl. Sci.*, 55(3):936–941, jun 2008. 7

[5] Sudhakar Chelikani, John Gore, and George Zubal. Optimizing compton camera geometries. *Physics in Medicine and Biology*, 49(8):1387, 2004. 8

[6] F. Roellinghoff, M.-H. Richard, M. Chevallier, J. Constanzo, D. Dauvergne, N. Freud, P. Henriquet, F. Le Foulher, J.M. Létang, G. Montarou, C. Ray, E. Testa, M. Testa, and A.H. Walenta. Design of a compton camera for 3d prompt- imaging during ion beam therapy. *Nuclear Instruments and Methods in Physics Research Section A: Accelerators, Spectrometers, Detectors and Associated Equipment*, 648, Supplement 1:S20 – S23, 2011. NIMA 4th International Conference on Imaging techniques in Subatomic Physics, Astrophysics, Medicine, Biology and Industry. 8, 33, 34

[7] William Erkonen. *Radiology 101 : the basics and fundamentals of imaging*. Lippincott-Raven, Philadelphia, 1998. 9

[8] Arman Rahmim and Habib Zaidi. Pet versus spect: strengths, limitations and challenges. *Nuclear Medicine Communications*, 29(3), 2008. 10

[9] Craig S Levin and Edward J Hoffman. Calculation of positron range and its effect on the fundamental limit of positron emission tomography system spatial resolution. *Physics in Medicine and Biology*, 44(3):781, 1999. 11

[10] *Clinical PET and PET/CT*. Springer Nature, 2005. 11

[11] S. DeBenedetti, C. E. Cowan, W. R. Konneker, and H. Primakoff. On the angular distribution of two-photon annihilation radiation. *Physical Review*, 77(2):205–212, jan 1950. 12

[12] Michael E. Phelps, editor. *PET*. Springer Nature, 2006. 12, 13, 141

[13] Simon R. Cherry, James A. Sorenson, and Michael E. Phelps. *Physics in Nuclear Medicine*. Elsevier/Saunders, 2012. 13, 14, 141

[14] Glenn F Knoll. *Radiation detection and measurement; 4th ed.* John Wiley and Sons, Inc., 2010. 15, 16, 17, 18, 141

[15] Saint gobain prelude 420 datasheet, 2014. 18

[16] Saint gobain brillance 380 datasheet, 2014. 18

[17] E. V. D. van Loef, P. Dorenbos, C. W. E. van Eijk, K. Krämer, and H. U. Güdel. High-energy-resolution scintillator: Ce3+ activated labr3. *Applied Physics Letters*, 79(10), 2001. 19

[18] https://upload.wikimedia.org/wikipedia/commons/5/5f/photomultipliertubeandscintillator.jpg. 20, 141

[19] Photomultipliers tubes. basics and applications. third edition. 21, 141

[20] https://upload.wikimedia.org/wikipedia/commons/d/d6/pn-junction-equilibrium.png. 22, 141

[21] Advansid application note ”introduction to sipms”. 26, 27, 28, 29, 30, 142

[22] Ane Etxebeste, John Barrio, Enrique Muñoz, Josep F Oliver, Carles Solaz, and Gabriela Llosá. 3d position determination in monolithic crystals coupled to sipms for pet. *Physics in Medicine and Biology*, 61(10):3914, 2016. 31, 64, 81, 110, 126

[23] Joost M Verburg, Kent Riley, Thomas Bortfeld, and Joao Seco. Energy- and time-resolved detection of prompt gamma-rays for proton range verification. *Physics in Medicine and Biology*, 58(20):L37–L49, sep 2013. 33, 118

[24] Chul-Hee Min, Chan Hyeong Kim, Min-Young Youn, and Jong-Won Kim. Prompt gamma measurements for locating the dose falloff region in the proton therapy. *Applied Physics Letters*, 89(18):183517, oct 2006. 33, 118

[25] E. Testa, M. Bajard, M. Chevallier, D. Dauvergne, F. Le Foulher, N. Freud, J.M. Létang, J.C. Poizat, C. Ray, and M. Testa. Dose profile monitoring with carbon ions by means of prompt-gamma measurements. *Nuclear Instruments and Methods in Physics Research Section B: Beam Interactions with Materials and Atoms*, 267(6):993–996, mar 2009. 33, 118

[26] Julien Smeets, Frauke Roellinghoff, Guillaume Janssens, Irene Perali, Andrea Celani, Carlo Fiorini, Nicolas Freud, Etienne Testa, and Damien Prieels. Experimental comparison of knife-edge and multi-parallel slit collimators for prompt gamma imaging of proton pencil beams. *Frontiers in Oncology*, 6, jun 2016. 33

[27] M. Frandes, A. Zoglauer, V. Maxim, and R. Prost. A tracking compton-scattering imaging system for hadron therapy monitoring. *IEEE Transactions on Nuclear Science*, 57(1):144–150, Feb 2010. 33

[28] S W Peterson, D Robertson, and J Polf. Optimizing a three-stage compton camera for measuring prompt gamma rays emitted during proton radiotherapy. *Physics in Medicine and Biology*, 55(22):6841, 2010. 33

[29] T. Kormoll, F. Fiedler, S. Schöne, J. Wüstemann, K. Zuber, and W. Enghardt. A compton imager for in-vivo dosimetry of proton beams—a design study. *Nuclear Instruments and Methods in Physics Research Section A: Accelerators, Spectrometers, Detectors and Associated Equipment*, 626–627:114 – 119, 2011. 33

[30] Shunsuke Kurosawa, Hidetoshi Kubo, Kazuki Ueno, Shigeto Kabuki, Satoru Iwaki, Michiaki Takahashi, Kojiro Taniue, Naoki Higashi, Kentaro Miuchi, Toru Tanimori, Dogyun Kim, and Jongwon Kim. Prompt gamma detection for range verification in proton therapy. *Current Applied Physics*, 12(2):364 – 368, 2012. 33

[31] G. Llosá, J. Barrio, J. Cabello, A. Crespo, C. Lacasta, M. Rafecas, S. Callier, C. de La Taille, and L. Raux. Detector characterization and first coincidence tests of a compton telescope based on LaBr3 crystals and SiPMs. *Nuclear Instruments and Methods in Physics Research Section A: Accelerators, Spectrometers, Detectors and Associated Equipment*, 695:105–108, dec 2012. 33, 39

[32] Thirolf, P.G., Aldawood, S., Böhmer, M., Bortfeldt, J., Castelhano, I., Dedes, G., Fiedler, F., Gernhäuser, R., Golnik, C., Helmbrecht, S., Hueso-González, F., Kolff, H. v.d., Kormoll, T., Lang, C., Liprandi, S., Lutter, R., Marinšek, T., Maier, L., Pausch, G., Petzoldt, J., Römer, K., Schaart, D., and Parodi, K. A compton camera prototype for prompt gamma medical imaging. *EPJ Web of Conferences*, 117:05005, 2016. 33

[33] http://envision.web.cern.ch/envision/. 33

[34] Sebastian Schoene, Wolfgang Enghardt, Fine Fiedler, Christian Golnik, Guntram Pausch, Heide Rohling, and Thomas Kormoll. An image reconstruction framework and camera prototype aimed for compton imaging for in-vivo dosimetry of therapeutic ion beams. *IEEE Transactions on Radiation and Plasma Medical Sciences*, 1(1):96–107, jan 2017. 34

[35] M Bouchel, S Callier, F Dulucq, J Fleury, J J Jaeger, C de La Taille, G Martin-Chassard, and L Raux. Spiroc (sipm integrated read-out chip): dedicated very front-end electronics for an ilc prototype hadronic calorimeter with sipm read-out. *Journal of Instrumentation*, 6(01):C01098, 2011. 36, 83, 118

[36] G. Llosá, J. Barrio, C. Lacasta, S. Callier, L. Raux, and C. de La Taille. First tests in the application of silicon photomultiplier arrays to dose monitoring in hadron therapy. *Nuclear Instruments and Methods in Physics Research Section A: Accelerators, Spectrometers, Detectors and Associated Equipment*, 648, Supplement 1:S96 – S99, 2011. NIMA 4th International Conference on Imaging techniques in Subatomic Physics, Astrophysics, Medicine, Biology and Industry. 39, 43

[37] J. Cabello, J. Barrio, C. Lacasta, M. Rafecas, and G. Llosá. Position reconstruction in detectors based on continuous crystals coupled to silicon photomultiplier arrays. In *2011 IEEE Nuclear Science Symposium Conference Record*, pages 3911–3916, Oct 2011. 44

[38] G. Llosá, J. Cabello, S. Callier, J.E. Gillam, C. Lacasta, M. Rafecas, L. Raux, C. Solaz, V. Stankova, C. de La Taille, M. Trovato, and J. Barrio. First compton telescope prototype based on continuous LaBr3-SiPM detectors. *Nuclear Instruments and Methods in Physics Research Section A: Accelerators, Spectrometers, Detectors and Associated Equipment*, 718:130–133, aug 2013. 50, 119

[39] Gabriela Llosá, Marco Trovato, John Barrio, Ane Etxebeste, Enrique Muñoz, Carlos Lacasta, Josep F. Oliver, Magdalena Rafecas, Carles Solaz, and Paola Solevi. First images of a three-layer compton telescope prototype for treatment monitoring in hadron therapy. *Frontiers in Oncology*, 6:14, 2016. 50, 97, 120

[40] Paola Solevi, Enrique Muñoz, Carles Solaz, Marco Trovato, Peter Dendooven, John E Gillam, Carlos Lacasta, Josep F Oliver, Magdalena Rafecas, Irene Torres-Espallardo, and Gabriela Llosá. Performance of macaco compton telescope for ion-beam therapy monitoring: first test with proton beams. *Physics in Medicine and Biology*, 61(14):5149, 2016. 50, 97, 120

[41] Jinhun Joung, Robert Miyaoka, and Thomas Lewellen. cMiCE: a high resolution animal PET using continuous LSO with a statistics based positioning scheme. *Nucl. Instrum. in Phys. Res. A*, 489(1):584–98, 2002. 51

[42] Steven Staelens, Yves D'Asseler, Stefaan Vandenberghe, Michel Koole, Ignace Lemahieu, and Rik Van de Walle. A three-dimensional theoretical model incorporating spatial detection uncertainty in continuous detector PET. *Phys. Med. Biol.*, 49(11):2337, 2004. 51

[43] Christoph Werner Lerche, JM Benlloch, F Sanchez, N Pavon, B Escat, EN Gimenez, M Fernandez, I Torres, M Gimenez, J Martínez, et al. Depth of γ-ray interaction within continuous crystals from the width of its scintillation light-distribution. *IEEE Trans. Nucl. Sci.*, 52(3):560–72, 2005. 51

[44] Sascha Moehrs, Alberto Del Guerra, Deborah J Herbert, and Mark A Mandelkern. A detector head design for small-animal PET with silicon photomultipliers (SiPM). *Phys. Med. Biol.*, 51(5):1113, 2006. 51

[45] Peter Bruyndonckx, Cedric Lemaître, Dennis Schaart, Marnix Maas, Magalie Krieguer, Olivier Devroede, Stefaan Tavernier, et al. Towards a continuous crystal APD-based PET detector design. *Nucl. Instrum. in Phys. Res. A*, 571(1):182–6, 2007. 51

[46] T Ling, TH Burnett, TK Lewellen, and RS Miyaoka. Parametric positioning of a continuous crystal PET detector with depth of interaction decoding. *Phys. Med. Biol.*, 53(7):1843, 2008. 51

[47] Harrison H Barrett, William CJ Hunter, Brian William Miller, Stephen K Moore, Yichun Chen, and Lars R Furenlid. Maximum-likelihood methods for processing signals from γ-ray detectors. *IEEE Trans. Nucl. Sci.*, 56(3):725–35, 2009. 51

[48] G Llosá, J Barrio, C Lacasta, M G Bisogni, A Del Guerra, S Marcatili, P Barrillon, S Bondil-Blin, C de la Taille, and C Piemonte. Characterization of a pet detector head based on continuous lyso crystals and monolithic, 64-pixel silicon photomultiplier matrices. *Physics in Medicine and Biology*, 55(23):7299, 2010. 51, 58, 63

[49] Zhi Li, M Wedrowski, P Bruyndonckx, and G Vandersteen. Nonlinear least-squares modeling of 3D interaction position in a monolithic scintillator block. *Phys. Med. Biol.*, 55(21):6515, 2010. 51

[50] Pedro Rato Mendes, Icíar Sarasola Martín, Mario Cañadas, Paz García de Acilu, Robin Cuypers, José Manuel Pérez, and Carlos Willmott. Characterization and performance of monolithic detector blocks with a dedicated ASIC front-end readout for PET imaging of the human brain. *Nucl. Instrum. in Phys. Res. A*, 633:S33–5, 2011. 51

[51] Herman T Van Dam, Stefan Seifert, Ruud Vinke, Peter Dendooven, Herbert Löhner, Freek J Beekman, and Dennis R Schaart. A practical method for depth of interaction determination in monolithic scintillator PET detectors. *Phys. Med. Biol.*, 56(13):4135, 2011. 51

[52] P Aguiar, A Iglesias, B Couce, and C Lois. A feasibility study on the use of arrays of discrete SiPMs for MR compatible LYSO readout using Monte Carlo simulation. *J. Instrum.*, 7(06):P06002, 2012. 51

[53] David McElroy, Valeri Saveliev, Alla Reznik, and John Rowlands. Evaluation of silicon photomultipliers: a promising new detector for MR compatible PET. *Nucl. Instrum. Methods Phys. Res. A*, 571(1):106–9, 2007. 52

[54] Gabriela Llosá, Roberto Battiston, Nicola Belcari, Maurizio Boscardin, Gianmaria Collazuol, Francesco Corsi, Gian-Franco Dalla Betta, Alberto Del Guerra, Nicoleta Dinu, Giuseppe Levi, et al. Novel silicon photomultipliers for PET applications. *IEEE Trans. Nucl. Sci.*, 55(3):877–81, 2008. 52

[55] Dennis R Schaart, Herman T van Dam, Stefan Seifert, Ruud Vinke, Peter Dendooven, Herbert Löhner, and Freek J Beekman. A novel, SiPM-array-based, monolithic scintillator detector for PET. *Phys. Med. Biol.*, 54(11):3501, 2009. 52

[56] Armin Kolb, Eckart Lorenz, Martin S Judenhofer, Dieter Renker, Konrad Lankes, and Bernd J Pichler. Evaluation of Geiger-mode APDs for PET block detector designs. *Phys. Med. Biol.*, 55(7):1815, 2010. 52

[57] Samuel España, LM Fraile, JL Herraiz, José Manuel Udías, Manuel Desco, and Juan José Vaquero. Performance evaluation of SiPM photodetectors for PET imaging in the presence of magnetic fields. *Nucl. Instrum. in Phys. Res. A*, 613(2):308–16, 2010. 52

[58] Emilie Roncali and Simon R Cherry. Application of silicon photomultipliers to positron emission tomography. *Annals of Biomedical Engineering*, 39(4):1358–77, 2011. 52

[59] Alberto Del Guerra, Nicola Belcari, Maria Giuseppina Bisogni, Francesco Corsi, Maurizio Foresta, Pedro Guerra, Sara Marcatili, Andres Santos, and Giancarlo Sportelli. Silicon Photomultipliers (SiPM) as novel photodetectors for PET. *Nuclear Instruments and Methods in Physics Research Section A: Accelerators, Spectrometers, Detectors and Associated Equipment*, 648:S232–5, 2011. 52

[60] Taiga Yamaya, Takayuki Mitsuhashi, Takahiro Matsumoto, Naoko Inadama, Fumihiko Nishikido, Eiji Yoshida, Hideo Murayama, Hideyuki Kawai, Mikio Suga, and

Mitsuo Watanabe. A SiPM-based isotropic-3D PET detector X'tal cube with a three-dimensional array of 1 mm3 crystals. *Phys. Med. Biol.*, 56(21):6793, 2011. 52

[61] S. Blin, P. Barrillon, and C. de La Taille. Maroc, a generic photomultiplier readout chip. *IEEE Nucl. Sci. Symp. Med. Imag. Conf.*, page 1690, 2010. 55, 83, 121

[62] J. Cabello, P. Barrillon, J. Barrio, M.G. Bisogni, A. Del Guerra, C. Lacasta, M. Rafecas, H. Saikouk, C. Solaz, P. Solevi, C. de La Taille, and G. Llosá. High resolution detectors based on continuous crystals and sipms for small animal {PET}. *Nuclear Instruments and Methods in Physics Research Section A: Accelerators, Spectrometers, Detectors and Associated Equipment*, 718:148 – 150, 2013. Proceedings of the 12th Pisa Meeting on Advanced DetectorsLa Biodola, Isola d'Elba, Italy, May 20 – 26, 2012. 64

[63] G. Llosá, J. Barrio, J. Cabello, C. Lacasta, J. F. Oliver, M. Rafecas, C. Solaz, P. Barrillon, C. de La Taille, M. G. Bisogni, A. Del Guerra, and C. Piemonte. Development of a pet prototype with continuous lyso crystals and monolithic sipm matrices. In *Nuclear Science Symposium and Medical Imaging Conference (NSS/MIC), 2011 IEEE*, pages 3631–3634, Oct 2011. 68

[64] Dan J Kadrmas. Lor-osem: statistical pet reconstruction from raw line-of-response histograms. *Physics in Medicine and Biology*, 49(20):4731, 2004. 68

[65] G. Llosá, P. Barrillon, J. Barrio, M.G. Bisogni, J. Cabello, A. Del Guerra, A. Etxebeste, J.E. Gillam, C. Lacasta, J.F. Oliver, M. Rafecas, C. Solaz, V. Stankova, and C. de La Taille. High performance detector head for {PET} and pet/mr with continuous crystals and sipms. *Nuclear Instruments and Methods in Physics Research Section A: Accelerators, Spectrometers, Detectors and Associated Equipment*, 702:3 – 5, 2013. PET/MR and SPECT/MR: New Paradigms for Combined Modalities in Molecular Imaging. 70

[66] J E Gillam, P Solevi, J F Oliver, and M Rafecas. Simulated one-pass list-mode: an approach to on-the-fly system matrix calculation. *Physics in Medicine and Biology*, 58(7):2377, 2013. 70

[67] Sara St James, Yongfeng Yang, Spencer L Bowen, Jinyi Qi, and Simon R Cherry. Simulation study of spatial resolution and sensitivity for the tapered depth of

interaction pet detectors for small animal imaging. *Physics in Medicine and Biology*, 55(2):N63, 2010. 72, 122

[68] S. Agostinelli, J. Allison, K. Amako, J. Apostolakis, H. Araujo, P. Arce, M. Asai, D. Axen, S. Banerjee, G. Barrand, F. Behner, L. Bellagamba, J. Boudreau, L. Broglia, A. Brunengo, H. Burkhardt, S. Chauvie, J. Chuma, R. Chytracek, G. Cooperman, G. Cosmo, P. Degtyarenko, A. Dell'Acqua, G. Depaola, D. Dietrich, R. Enami, A. Feliciello, C. Ferguson, H. Fesefeldt, G. Folger, F. Foppiano, A. Forti, S. Garelli, S. Giani, R. Giannitrapani, D. Gibin, J.J. Gómez Cadenas, I. González, G. Gracia Abril, G. Greeniaus, W. Greiner, V. Grichine, A. Grossheim, S. Guatelli, P. Gumplinger, R. Hamatsu, K. Hashimoto, H. Hasui, A. Heikkinen, A. Howard, V. Ivanchenko, A. Johnson, F.W. Jones, J. Kallenbach, N. Kanaya, M. Kawabata, Y. Kawabata, M. Kawaguti, S. Kelner, P. Kent, A. Kimura, T. Kodama, R. Kokoulin, M. Kossov, H. Kurashige, E. Lamanna, T. Lampén, V. Lara, V. Lefebure, F. Lei, M. Liendl, W. Lockman, F. Longo, S. Magni, M. Maire, E. Medernach, K. Minamimoto, P. Mora de Freitas, Y. Morita, K. Murakami, M. Nagamatu, R. Nartallo, P. Nieminen, T. Nishimura, K. Ohtsubo, M. Okamura, S. O'Neale, Y. Oohata, K. Paech, J. Perl, A. Pfeiffer, M.G. Pia, F. Ranjard, A. Rybin, S. Sadilov, E. Di Salvo, G. Santin, T. Sasaki, N. Savvas, Y. Sawada, S. Scherer, S. Sei, V. Sirotenko, D. Smith, N. Starkov, H. Stoecker, J. Sulkimo, M. Takahata, S. Tanaka, E. Tcherniaev, E. Safai Tehrani, M. Tropeano, P. Truscott, H. Uno, L. Urban, P. Urban, M. Verderi, A. Walkden, W. Wander, H. Weber, J.P. Wellisch, T. Wenaus, D.C. Williams, D. Wright, T. Yamada, H. Yoshida, and D. Zschiesche. Geant4—a simulation toolkit. *Nuclear Instruments and Methods in Physics Research Section A: Accelerators, Spectrometers, Detectors and Associated Equipment*, 506(3):250 – 303, 2003. 72

[69] J. Allison, K. Amako, J. Apostolakis, H. Araujo, P. Arce Dubois, M. Asai, G. Barrand, R. Capra, S. Chauvie, R. Chytracek, G. A. P. Cirrone, G. Cooperman, G. Cosmo, G. Cuttone, G. G. Daquino, M. Donszelmann, M. Dressel, G. Folger, F. Foppiano, J. Generowicz, V. Grichine, S. Guatelli, P. Gumplinger, A. Heikkinen, I. Hrivnacova, A. Howard, S. Incerti, V. Ivanchenko, T. Johnson, F. Jones, T. Koi, R. Kokoulin, M. Kossov, H. Kurashige, V. Lara, S. Larsson, F. Lei, O. Link, F. Longo, M. Maire, A. Mantero, B. Mascialino, I. McLaren, P. Mendez Lorenzo, K. Minamimoto, K. Murakami, P. Nieminen, L. Pandola, S. Parlati, L. Peralta, J. Perl, A. Pfeiffer, M. G.

Pia, A. Ribon, P. Rodrigues, G. Russo, S. Sadilov, G. Santin, T. Sasaki, D. Smith, N. Starkov, S. Tanaka, E. Tcherniaev, B. Tome, A. Trindade, P. Truscott, L. Urban, M. Verderi, A. Walkden, J. P. Wellisch, D. C. Williams, D. Wright, and H. Yoshida. Geant4 developments and applications. *IEEE Transactions on Nuclear Science*, 53(1):270–278, Feb 2006. 72

[70] J. Barrio, J. Cabello, A. Etxebeste, C. Lacasta, J. F. Oliver, M. Rafecas, C. Solaz, V. Stankova, and G. Llosá. Electronics upgrade and crystal geometry optimization for a sub-millimeter small animal pet based on continuous crystals and sipms. In *2013 IEEE Nuclear Science Symposium and Medical Imaging Conference (2013 NSS/MIC)*, pages 1–4, Oct 2013. 72

[71] C. M. Pepin, P. Berard, A. L. Perrot, C. Pepin, D. Houde, R. Lecomte, C. L. Melcher, and H. Dautet. Properties of lyso and recent lso scintillators for phoswich pet detectors. *IEEE Transactions on Nuclear Science*, 51(3):789–795, June 2004. 74

[72] R. S. Miyaoka, X. Li, C. Lockhart, and T. K. Lewellen. Comparison of detector intrinsic spatial resolution characteristics for sensor on the entrance surface and conventional readout designs. *IEEE Transactions on Nuclear Science*, 57(3):990–997, June 2010. 75, 122

[73] F. Powolny, E. Auffray, S.E. Brunner, E. Garutti, M. Goettlich, H. Hillemanns, P. Jarron, P. Lecoq, T. Meyer, H.C. Schultz-Coulon, W. Shen, and M.C.S. Williams. Time-based readout of a silicon photomultiplier (sipm) for time of flight positron emission tomography (tof-pet). *Nuclear Science, IEEE Transactions on*, 58(3):597–604, June 2011. 83

[74] I Sacco, P Fischer, M Ritzert, and I Peric. A low power front-end architecture for sipm readout with integrated adc and multiplexed readout. *Journal of Instrumentation*, 8(01):C01023, 2013. 83

[75] A. Argentieri, F. Corsi, M. Foresta, C. Marzocca, and A. Del Guerra. Design and characterization of {CMOS} multichannel front-end electronics for silicon photomultipliers. *Nuclear Instruments and Methods in Physics Research Section A: Accelerators, Spectrometers, Detectors and Associated Equipment*, 652(1):516 – 519, 2011. Symposium on Radiation Measurements and Applications (SORMA) {XII} 2010. 83

[76] J. Talebi S. Azman G. Maehlum D. Meier, S. Mikkelsen and B. E. Patt. An asic for sipm/mppc readout. *IEEE Nucl. Sci. Symp. Med. Imag. Conf.*, page 1653, 2010. 84, 85

[77] M D Rolo, R Bugalho, F Gonçalves, G Mazza, A Rivetti, J C Silva, R Silva, and J Varela. Tofpet asic for pet applications. *Journal of Instrumentation*, 8(02):C02050, 2013. 84

[78] http://ideas.no/. 84

[79] J. Barrio, A. Etxebeste, C. Lacasta, E. Muñoz, J.F. Oliver, C. Solaz, and G. Llosá. Performance of vata64hdr16 asic for medical physics applications based on continuous crystals and sipms. *Journal of Instrumentation*, 10(12):P12001, 2015. 84, 124

[80] Vata64hdr16 datasheet specification v2r1. 85

[81] M.G. Bagliesi, C. Avanzini, G. Bigongiari, R. Cecchi, M.Y. Kim, P. Maestro, P.S. Marrocchesi, and F. Morsani. A custom front-end {ASIC} for the readout and timing of 64 sipm photosensors. *Nuclear Physics B - Proceedings Supplements*, 215(1):344 – 348, 2011. Proceedings of the 12th Topical Seminar on Innovative Particle and Radiation Detectors (IPRD10). 85

[82] https://www.dymax.com/index.php/en/adhesives/products/9001-e-v35. 87

[83] C. Solaz, J. Barrio, G. Llosá, V. Stankova, M. Trovato, and C. Lacasta. Data acquisition system for the readout of sipm arrays. In *2013 IEEE Nuclear Science Symposium and Medical Imaging Conference (2013 NSS/MIC)*, pages 1–4, Oct 2013. 87

[84] G. Llosá, J. Barrio, J. Cabello, A. Crespo, C. Lacasta, M. Rafecas, S. Callier, C. de La Taille, and L. Raux. Detector characterization and first coincidence tests of a compton telescope based on labr3 crystals and sipms. *Nuclear Instruments and Methods in Physics Research Section A: Accelerators, Spectrometers, Detectors and Associated Equipment*, 695:105 – 108, 2012. New Developments in Photodetection {NDIP11}. 95

[85] http://advansid.com/products/product-detail/asd-rgb-nuv-1-5s-p-8x8a. 100

[86] http://advansid.com/. 100

[87] N Serra, A Ferri, A Gola, T Pro, A Tarolli, N Zorzi, and C Piemonte. Characterization of new fbk sipm technology for visible light detection. *Journal of Instrumentation*, 8(03):P03019, 2013. 100

List of Figures

List of Tables